Dissertation

submitted to the

Combined Faculty of Mathematics, Engineering and Natural Sciences

of **Heidelberg University, Germany**

for the degree of

Doctor of Natural Sciences

Put forward by
Jonathan Morgner
born in Langenhagen
Oral examination: November 26, 2024

Stringent Test of Bound-State Quantum Electrodynamics with Highly Charged Tin

Referees:

Prof. Dr. Klaus Blaum

Jun.-Prof. Dr. Skyler Degenkolb

Zusammenfassung

Die Quantenelektrodynamik ist die am besten getestete fundamentale Theorie. Sie ist allgegenwärtig und an fast allen grundlegenden Prozessen beteiligt, angefangen bei der Wechselwirkung zwischen Licht und Materie. Noch ist das Standardmodell der Teilchenphysik unvollständig und bedarf weiterer Forschung. Daher ist es wichtig, das Verständnis der am besten zugänglichen Prozesse zu vertiefen. Die Quantenelektrodynamik muss daher in all ihren Facetten getestet und ihre Gültigkeit in Extremsituationen überprüft werden, um Rückschlüsse auf unser Universum ziehen zu können. Zu diesem Zweck werden hier drei Messungen an verschiedenen Ladungszuständen von hochgeladenem Zinn vorgestellt. Wasserstoffähnliches Zinn, ein Zinnkern mit einem einzelnen gebundenen Elektron, wurde in das Penning-Fallen-Experiment ALPHATRAP geladen und der g-Faktor des gebundenen Elektrons mit einer relativen Genauigkeit von 5×10^{-10} bestimmt. Bisher waren alle hochpräzisen Messungen des g-Faktors auf Kerne mit einer Ordnungszahl $Z \leq 20$ beschränkt. Mit $Z = 50$ erlaubt die Messung an Zinn die Überprüfung der Theorie in einem bisher unerreichten Regime. Dies erlaubt Rückschlüsse auf die Gültigkeit der Quantenelektrodynamik in den hohen elektrischen Feldern, denen das Elektron in der Nähe des Atomkerns ausgesetzt ist. Auch der g-Faktor von lithium- und borartigem Zinn wurde mit ähnlicher Genauigkeit bestimmt. Dies ermöglicht die Untersuchung der Wechselwirkung zwischen den Elektronen. Gleichzeitig werden verschiedene Entwicklungen zur Verbesserung dieser Tests vorgestellt.

Abstract

Quantum electrodynamics is the best-tested fundamental theory. It is ubiquitous and contributes to almost all fundamental processes, starting with the interaction between light and matter. The Standard Model of particle physics is still incomplete and requires further research. It is therefore important to deepen the understanding of the most accessible processes. Quantum electrodynamics must therefore be tested in all its facets and its validity verified in extreme situations in order to be able to draw conclusions about our universe. To this end, three measurements on different charge states of highly charged tin are presented here. Hydrogen-like tin, a tin nucleus with a single bound electron, was injected into the Penning-trap experiment ALPHATRAP and the g factor of the bound electron was determined with a relative precision of 5×10^{-10}. Until now, all high-precision measurements of the g factor of highly charged ions were performed on elements with an atomic number $Z \leq 20$. With $Z = 50$, the measurement on tin enables the theory to be tested in an unprecedented regime. From this conclusions can be drawn about the validity of quantum electrodynamics in the high electric fields to which the electron is exposed in the vicinity of the atomic nucleus. The g factor of lithium-like and boron-like tin has also been determined with similar accuracy. This makes it possible to study the interaction between the electrons. At the same time, various developments to improve these tests are presented.

Contents

Chapter 1

Introduction

At the beginning of the 20th century, Max Planck was the first to describe the theory explaining the absorption spectrum of a perfect black body, which had been introduced earlier by the pioneering work of Gustav Kirchhoff [1]. Planck explained that a system of individually oscillating resonators could quantitatively describe the observed spectra [2]. This was one of the first hints towards quantum mechanics, which was soon extended by Albert Einstein to explain the photoelectric effect [3]. In 1914, Nils Bohr introduced his model of the atom, which implemented quantum mechanics in terms of discrete energy levels and was the first to successfully reproduce the energy spectrum of the hydrogen atom [4]. This was followed in the 1920s by Erwin Schrödinger's idea of wave mechanics, which introduced the wave function of particles described by the Schrödinger equation [5]. This was further refined for Lorentz invariance by Paul Dirac [6].

By now these discoveries are close to 100 years ago and in the year 2025 the *International Year of Quantum Science and Technology* will be celebrated globally[1]. With the experimental observation of the Lamb shift by Lamb and Retherford [7], additional effects were discovered and had to be described, leading to the description of effects from virtual particles. Pioneering work was done by Hans Bethe, Richard Feynman and Julian Schwinger accurately describing the interaction of charged particles by mediation of photons, with new effects like Self Energy (SE) and Vacuum Polarization (VP) [8–11]. This can be considered the foundation of quantum electrodynamics (QED).

QED has become one of the fundamental pillars of the Standard Model of (particle) physics. It is ubiquitous in everything from particle collisions, atoms and ions, molecules and quantum chemistry to large-scale systems such as stars. As the most accessible fundamental interaction, rigorous tests can shed light on the incomplete parts of the Standard Model, such as baryogenesis, neutrino oscillations, and the presence of dark matter and dark energy. Therefore it must be tested in all its aspects with highest precision possible.

Presently, there is a lot of focus on simple systems, that can be described precisely from *ab initio* theory. A highlight measurement is the determination of $g-2$, the anomalous magnetic moment of the free electron [12]. This measurement is used to determine the fine-structure constant α, which quantifies the coupling strength between charged particles. α can also be determined by measuring the recoil experienced by an atom when it absorbs a photon [13, 14]. Therefore, using α as determined by the atomic recoil experiments, QED can be precisely tested in the $g-2$ value. Further tests of this theory can be made with atomic systems, i.e. systems consisting of several particles bound together by their electromagnetic interaction. Not only atomic/ electronic systems

[1] See www.dpg-physik.de/aktivitaeten-und-programme/quanten-2025 and www.quantum2025.org for further information.

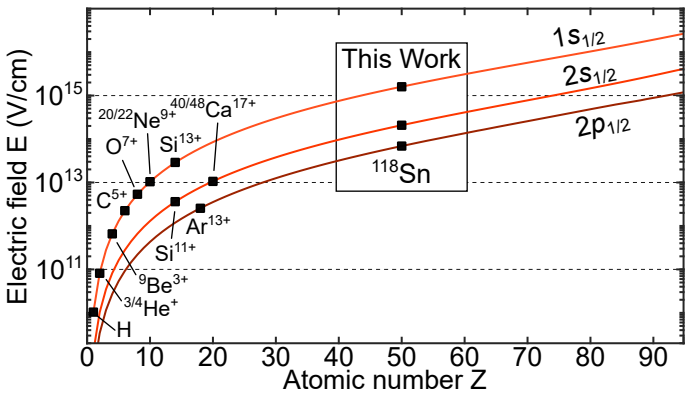

Fig. 1.1: Mean electric field at the valence electron in ground-state hydrogen-like, lithium-like and boron-like ions. The black squares mark the available high-precision measurements. In the box, the here presented measurements of the three different charge states of Sn-118 are highlighted. These are at much higher Z with significantly higher field strength than any prior high-precision g-factor measurement. Prior measurements are reported in Ref. [18–30].

are of interest, but also those with bound muons, pions, antiprotons and so on [15–17]. These multi-body systems have additional interactions between the bound particle(s) and the nucleus. Typically referred to as bound-state effects, they are of particular interest because any atomic system can be predicted by their rigorous treatment. In such systems there are certain properties that can be both measured and predicted very precisely, enabling the underlying theory to be tested. These are the Lamb shift, the hyperfine structure and the magnetic moment, which is related to the g factor.

Part of the problem with atomic systems is the electron-electron interaction. The higher the number of electrons, the more complex this becomes. This can be overcome with highly charged ions (HCIs), because with only a few bound electrons the interaction can be treated rigorously from *ab initio* theory. In the simplest case, only a single electron is bound to the nucleus, making it very similar to the hydrogen atom. For these *hydrogen-like* ions in the electronic ground state, the binding scales strongly with the atomic number Z. This brings the electron wave function closer to the nucleus and increases the interaction between the two charged particles. At high Z the remaining electron in the $1s$ configuration experiences an average electric field greater than $10^{16}\,\mathrm{V/cm}$, which is orders of magnitude stronger than any field that can be produced in a laboratory. Fig. 1.1 shows the mean electric field experienced by the hydrogen-like $1s$ electron and that for the valence electron in the lithium-like (three electrons, $1s^2 2s$) and boron-like (five electrons, $1s^2 2s^2 2p$) system. Precise measurements in these fields therefore enable the theory to be tested under extreme conditions. Furthermore, the bound electron becomes highly relativistic, which requires a rigorous treatment of the electron-nucleus interaction using the Dirac equation. The calculation of these effects is outlined in the next chapter, with particular focus on the bound-electron g factors.

By now, many high-precision measurements of HCI at high Z exist. Measurements of the Lamb shift of specific energy levels have already reached the highest Z with several measurements of uranium [31–34]. Similarly, the hyper-fine structure (HFS) has been studied in high-Z systems [35–38]. HFS measurements are of particular interest because at high Z the bound electron experiences magnetic fields with a mean value above 20 000 T [39]. While this enables unique tests of the coupling with the strong nuclear magnetic moment, the prediction of these is much more difficult due to the Bohr-Weisskopf (BW) effect resulting from the unknown nuclear magnetization distribution. In 2001 it was proposed to measure the HFS in the hydrogen-like and lithium-like charge states in order to calculate a specific difference where the BW effect is canceled [40]. This has now been done with bismuth at high Z [37] and also at low Z with beryllium [30], testing the HFS theory precisely in both regimes.

Other important tests of bound-state QED (BS-QED) have been made with muonic systems. In the 1980s, high-precision measurements of muonic transitions were made to test QED in the

extreme field experienced by the heavy muon close to the nucleus [15, 41]. By choosing transitions between states with a similar finite nuclear size (FNS) contribution, the effect of the nuclear charge radius is suppressed. Thus it is possible to precisely test the theory without the otherwise limiting uncertainty from the FNS contribution. Furthermore, due to the higher mass of the muon, the VP terms are much larger than for electrons, as they scale with mass. This enables them to be probed with unique sensitivity.

Of all the different observables that were tested in HCI, high-precision bound-electron g-factor measurements were so far exclusively performed at low Z. These are of particular interest, as the additional interaction with an external magnetic field includes additional terms that are not present in the Lamb shift for example. Hence there is motivation to perform high-precision g-factor measurements at high Z as well. Thus far the measurement of the hydrogen-like silicon ($Z = 14$) g factor is the highest Z studied so far[2]. Throughout the thesis the focus will be on systems without nuclear spin. There are some measurements available where the nuclear spin is non-zero, which further complicates both the measurement and the theoretical prediction due to the spin-spin coupling [28, 30]. Eventually, studying such systems at high Z may be of interest in the future.

Two approaches are used to produce HCI. In accelerator facilities, a particle beam passes through a stripper foil, which removes the electrons from the atom in the beam and turns them into HCI [43]. While this can produce large amounts of high Z nuclei in all charge states, the produced ions are very fast and must to be slowed down to (near) rest in order to trap them in an ion trap. This is the goal of HITRAP at the GSI Darmstadt, which will enable various experiments performed on large amounts of slow and trapped HCI [44].

The other approach is to use an electron beam ion trap (EBIT), where high charge states are produced by electron impact ionization [45]. An electron beam is accelerated in an electric field and compressed in a strong magnetic field to achieve a high current density. The fast electrons collide with the atoms and ions in the EBIT to (further) ionize them. This approach requires the kinetic energy of the electron beam to be greater than the binding energy of the bound electron, with a maximum in the cross section at about two to three times the binding energy [46].

Some experiments use in-trap EBITs where HCI are produced within the measurement apparatus [47–49]. These are limited to low binding energies as it is difficult to produce the high acceleration potentials required for their ionization. Therefore dedicated EBITs must be used to produce high-Z HCI. For example, the binding energy of the K-shell electrons in uranium is about 130 keV [50], so kinetic energies above 200 keV are required for efficient ionization. Successful production of hydrogen-like and bare uranium in an EBIT has been demonstrated in the past [51]. These high-energy EBITs are specialized and not suited for single-ion high-precision experiments. Thus in order to use the production capabilities of an EBIT, the ions have to be transferred to a separate measurement apparatus. There they are re-captured, and high-precision spectroscopy can be performed. One experiment with such a setup is the Penning-trap apparatus Alphatrap , in which the here presented measurements take place [52]. It was designed as a successor to the Mainz g-factor experiment, which performed a lot of g-factor measurements in the low-Z regime [20–25, 27]. The goal of Alphatrap is to extend these measurements into the high-Z regime. To achieve this it is connected to the Heidelberg-EBIT (HD-EBIT) which has shown to produce bare nuclei up to $Z \approx 55$ [53, 54].

Here presented are the g-factor measurements of hydrogen-like, lithium-like and boron-like tin-

[2]Note that there are g-factor measurements of hydrogen-like lead and hydrogen-like bismuth, but their relative precision is less than a 2×10^{-3} [39, 42]. Thus their precision is too low to resolve any contribution apart from the Breit correction.

118. At $Z = 50$ it therefore brings the QED tests with g factors into the medium-to-high-Z range, surpassing any previous bound-electron g-factor measurement as shown in Fig. 1.1. The hydrogen-like measurement tests QED in these extremely strong electric fields, where the BS-QED contributions are much stronger. At this high Z, the current theoretical approach using a $Z\alpha$ expansion reaches its limit, and a rigorous treatment of the effects is necessary for an improved comparison with the experiment.

The lithium-like and boron-like tin ions have multiple bound electrons, enabling the contributions from electron-electron interactions to be tested. The lithium-like charge state is of particular interest, as for some time there were large discrepancies between the measurements and the theoretical prediction of their bound-electron g factors [27, 55, 56]. It has been suggested that these are due to some inconsistencies in the calculation of the electron-electron interaction [57]. So the measurement of lithium-like tin tests this conjecture with a new element at much higher Z than any previous measurement.

In boron-like tin, with its $2P_{1/2}$ state, the spin-orbit coupling with $l = 1$ can be tested, making this also a unique test at high-Z. It is the second ground-state boron-like ion which g factor has been measured with high precision [26].

Structure

The thesis is structured in the following way: the first three chapter focus on the theoretical description of g factor, Penning traps and electron beam ion traps (Chapter 2,3,4). This is followed by a brief description of the experimental setup of the ALPHATRAP apparatus (Chapter 5). Following this is Chapter 6 presenting the results on the production of hydrogen-like tin using the Heidelberg-EBIT. This is followed by Chapter 7 which presents progress on the ALPHATRAP apparatus. Chapter 8 covers the measurement of the tin-118 mass performed to improve the g-factor measurements which are dependent on the mass of the ion. The g-factor measurements of the three charge states and the discussion of their error budget are presented in Chapter 9. This is followed by the outlook chapter, discussing upgrades that either were implemented, or could be implemented in the future. Finally, Chapter 11 summarizes the results and discusses the comparison between the theoretical predictions and experimental g factors.

Chapter 2

g-Factor Theory

HCI like hydrogen-like, lithium-like and boron-like ions can be considered simple systems. The g factor of these quantifies the ratio between their magnetic moment $\boldsymbol{\mu}_\mathrm{j}$ and its total angular momentum $\mathbf{J} = \mathbf{L} + \mathbf{S}$,

$$\boldsymbol{\mu}_\mathrm{j} = -\frac{g}{2}\frac{e}{m_\mathrm{e}}\mathbf{J}, \tag{2.1}$$

with e/m_e as the electron charge-to-mass ratio. For hydrogen-like and lithium-like charge states, the orbital angular momentum $\mathbf{L}$ of the valence electron is zero. These are therefore rather similar to the free-electron g factor. In boron-like systems, the orbital angular quantum number l is 1, causing a deviation to the free-electron case.

Generally, the g factor from Eq. (2.1) of these ions can be predicted from *ab initio* theory by calculating the various contributions that affect it. Separating these into reasonable categories gives it a form of:

$$\begin{aligned} g = 2 &+ (\Delta g_\mathrm{QED} + \Delta g_\mathrm{hadronic,weak} + ...)_\mathrm{free-electron} \\ &+ [\Delta g_\mathrm{Breit} + \Delta g_\mathrm{BS\text{-}QED} + \Delta g_\mathrm{FNS} + \Delta g_\mathrm{Recoil} \\ &+ (\Delta g_\mathrm{e\text{-}structure} + \Delta g_\mathrm{QED\text{-}screening} + ...)_\mathrm{e\text{-}e\text{-}interaction} + ...]_\mathrm{BS\text{-}effects} \end{aligned} \tag{2.2}$$

This is valid for S-state g factors[1]. A stylized overview of the contributions following the color-code in the equation is shown in Fig. 2.1. All these effects can be described by Feynman diagrams, with the first contribution as the tree-level contribution, which is simply the solution to the Dirac equation for the electron interacting with an external magnetic field via photon exchange. Its Feynman diagram is shown as the trunk of the tree in Fig. 2.1, labeled "Dirac". In this the horizontal line is the electron, which interacts with the magnetic field (triangle) by photon exchange (wiggly line). All additional effects can be split into two main categories: Free-electron effects, and those only present in bound-state systems. While the free-electron terms are dominated by radiative corrections, namely the self-energy (SE) and the vacuum polarization (VP), bound-state corrections include the additional photon exchange between the electron and the nucleus. In the following sections the contributions are discussed in order to provide the necessary background for understanding the implications of the measurements. However, the actual, very involved calculations are the active work subject of a multitude of people and were not part of this work [39, 57–63]. For this work, the theoretical predictions were calculated by the group of Zoltán Harman and by Vladimir Yerokhin and were published in articles that present their comparison with the experimental values [54, 64]. For more in-depth description of these effects and their calculations it is referred to Refs. [39, 59, 65, 66].

[1] For P-state g factors, e.g. in boron-like systems, the additional spin-orbit coupling must be considered, which changes the leading 2 to be $2/3$

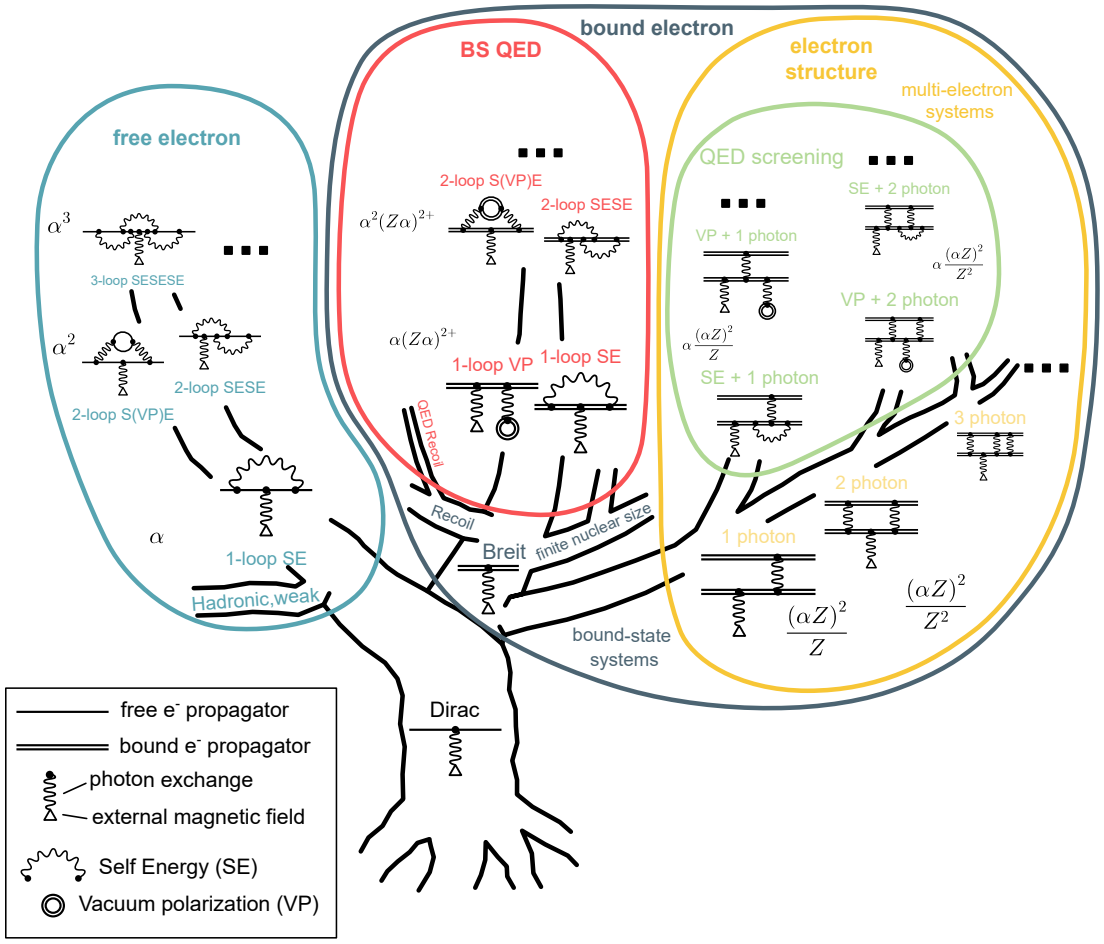

Fig. 2.1: Generalization of the various contributions to the g factor of an electron, with some exemplary Feynman diagrams for the different orders in the various "tree branches". At the left branch of the tree, the free-electron contributions are shown. These are dominated by QED effects scaling in ascending order of α. The middle are those with the additional terms for an electron bound to a nucleus with atomic number Z. The lowest contributing order of these effects is typically $(Z\alpha)^2$. Note that conventionally these diagrams include the free-electron terms as well, here they are shown separately to better distinguish between free-electron QED and BS-QED. Similar to the free-electron contributions, BS-QED effects additionally scale with the additional factor α^k for each k-loop QED. The recoil correction is described as an additional expansion in orders of m_e/M, the electron-to-ion mass ratio. These as well have higher loop-orders which are labeled QED-recoil including additional QED effects therefore getting the additional scaling with α. Furthermore, the finite nuclear size correction has to be included. Already on the Breit correction this has a significant impact. But also on the various QED-effects this causes a shift in g. On the right branch, the terms that result from the electron-electron interaction in multi-electron ions are shown. These can be separated into two groups, those purely with photon exchange, and those with an additional radiative QED loop. The dominating l-photon terms scale with order $(\alpha Z)^2/Z^l$. The QED screening terms then scale with $\alpha^k \frac{(\alpha Z)^2}{Z^l}$, with k as the loop order.

2.1 Free-Electron g Factor

The free-electron effects are dominated by corrections due to the radiative QED effects, the vacuum polarization (VP) and the self-energy (SE) corrections. These are called radiative terms due to the interaction of the charged particle via photons with itself (SE), and with the vacuum (VP). For the VP this is the interaction with the vacuum in the form of a virtual particle-antiparticle pair[2] exchanging a photon with the bound electron. The SE is describing the interaction of the electron with itself, the emittance and consecutive absorbance of a photon. The corresponding Feynman diagrams are shown on the left in the free-electron branch in Fig. 2.1. Note that in electronic systems like HCI due to the light mass of the electron, generally, the VP corrections are significantly smaller compared to the SE ones. This is not the case in muonic systems, where they contribute significantly more, showing that tests of VP can be performed most precisely in these [15, 41, 68]. These QED effects appear in ascending order, separated by on the amount of radiative loops in the Feynman diagram. Those with only a single SE or VP loop are the one-loop terms. Two-loop QED corrections therfore include all possible configurations with exactly two radiative loops (SESE, S(VP)E, etc.), three loop with three, etc.. These contribute to the free-electron g factor in the following form:

$$\Delta g_{\mathrm{QED}} = \sum_{l=1}^{\infty} C_{2l} \left(\frac{\alpha}{\pi}\right)^{l}, \tag{2.3}$$

with the C_{2n} as the n-loop correction, and α as the fine-structure constant quantifying the interaction strength between charged particles. These are labeled with $2n$, due to the SE and VP corrections always having an even number of vertices, where photons are emitted/absorbed. In this description, each n-loop order is thus scaling with α^n. With $\alpha^{-1} \approx 137$ they quickly decrease in size resulting in a converging series.

Naturally, with increasing loop order there are more possibilities to assemble the increasing number of radiative corrections. Thus the higher orders increase in complexity, making it challenging to evaluate all diagrams for a higher order. As of now the radiative corrections for the free-electron are evaluated analytically up to the four-loop terms, while the fifth loop is known only numerically [12, 69, 70]. On top of these QED radiative terms, some additional much smaller non-QED radiative corrections to the free-electron g factor exist, namely hadronic and electroweak effects $\Delta g_{\mathrm{hadronic,weak}}$ which are too small to be significant for the measurements of g factors in heavy HCI.

2.2 Bound-Electron g Factor

All the Feynman diagrams valid for the free-electron are also present in the bound state case. On top of this, further effects have to be considered. Fig. 2.2 shows the various contributions as a function of the atomic number Z. These additional terms describe the interaction of the particle with the Coulomb field of the nucleus. This bound-state is emphasized in the Feynman diagrams by denoting the electron with a double line. Therefore, the tree level diagram for the bound-state changes, and the Dirac value is perturbed in this bound state. This was first described by Breit in 1928 [71]. For the hydrogen-like ion, the Breit correction $\Delta g_{\mathrm{Breit}}$ for a point-like nucleus can be

[2] These are predominantly electron-positron pairs, but others are also possible, as in example muonic VP as well as pionic VP which are the dominant part of the hadronic contributions. These scale with the inverse square of the virtual particle mass, and therefore contribute only insignificantly in the context of the here presented measurements (< 3 ppb in the hydrogen-like tin g factor) [67].

analytically calculated as:

$$\Delta g_{\text{Breit}} = \frac{4}{3}\left(\sqrt{1-(Z\alpha)^2}-1\right). \tag{2.4}$$

For lithium-like and boron-like ions, it takes the form[39]:

$$\Delta g_{\text{Breit}} = \frac{2}{3}\left(\sqrt{2\left(1+\sqrt{1-(Z\alpha)^2}\right)}-2\right). \tag{2.5}$$

The above equations both exhibit in leading order a quadratic dependence on $Z\alpha$, showing the quadratic scaling of relativistic effects in HCI.

2.2.1 Bound-State QED

Additionally to the tree-level contribution, radiative terms are perturbed by the nuclear potential as well. $\Delta g_{\text{BS-QED}}$ can be, as for the free-electron case, described as an expansion along α, with the added term from the interaction with the nucleus, which can be described as a series expansion along $Z\alpha$, with the lowest order $(Z\alpha)^2$ [66]. This approach is commonly known as the $Z\alpha$ expansion, where the different coefficients for this series are evaluated individually. This is a perturbative approach, where the higher orders are evaluated as corrections to the free-electron case. From this follows, that the precision of the theoretical prediction is only as good as the size of the highest calculated term in the series. This is advantageous in the low-Z region, where $Z\alpha \ll 1$ and the series is converging quickly. For high Z where $Z\alpha$ is approaching 1, this places stringent limits on the accuracy that can be achieved. Thus, for the calculation of these effects at high-Z another theoretical approach is pursued. This is a rigorous *all-order* approach where one calculates the interaction with the nuclear Coulomb field non-perturbatively. This requires to evaluate all contributing Feynman diagrams and is furthermore computationally demanding. For the Lamb shift, all-order calculations exist both for the one-loop and the two-loop QED corrections. This is not the case for the bound-electron g factor, due to the added complexity from the interaction with the magnetic field, which is not present in the Lamb shift, rigorous calculation of these are not complete. While the one-loop QED corrections for hydrogen-like g factors can be calculated both with the expansion and with the all-order approach, some dominant two-loop QED corrections are only evaluated within the $Z\alpha$ expansion, and of these only the terms up to $(Z\alpha)^5$ are evaluated. Therefore, the precision of the prediction is limited by the remaining higher orders starting with $(Z\alpha)^6$.

This raises the question how to give a reasonable uncertainty on the remaining higher orders. Typically this is done by looking at the one-loop QED terms. These are known very precisely, and the scaling in these can be used for an estimate of the uncertainty of the unknown two-loop terms. From all the contributions to the bound-electron g factors in hydrogen-like ions with $Z \geq 4$, this has the largest uncertainty [30, 63]. Furthermore, due to the strong scaling with $Z\alpha$, the uncertainty increases rapidly with increasing Z.

Nonetheless, up till now, of all previously measured hydrogen-like g factors, only hydrogen-like silicon has a theoretical prediction that is less precise than the measurement [22]. With the here presented measurement of hydrogen-like tin, the $Z\alpha$ expansion is not competitive with the experimental precision anymore. With the $Z\alpha$ expansion, the theoretical prediction is limited to a relative accuracy of 0.15 ppm, which compared to the experimental precision of 0.5 ppb, is orders of magnitude less precise. This shows the demand for an all-order calculation of the two-loop contribution. Bastian Sikora, Max-Planck-Institut für Kernphysik, is currently working on

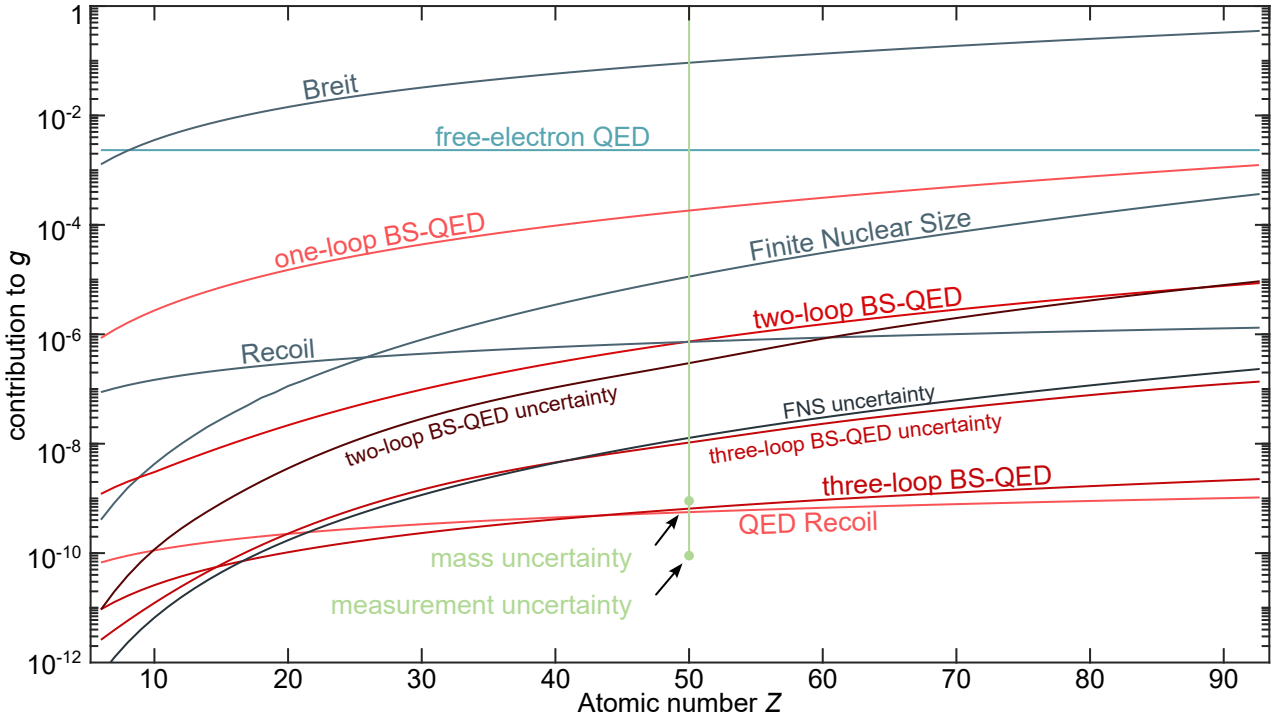

Fig. 2.2: Contributions to the g factor of a hydrogen-like ion. The data of this plot is kindly provided by Bastian Sikora, Max-Planck-Institut für Kernphysik, along with data from Ref. [72]. Details can be found in the text.

this [60, 73], and the calculation is approaching completion[3]. This has the chance to significantly improve the tests of QED in these high-Z systems, although eventually the precision will be limited by other uncertainties, like that of the finite nuclear size.

2.2.2 Finite Nuclear Size

The Breit correction assumes a point-like infinitely heavy nucleus, which therefore must be corrected for an accurate evaluation of the atomic system. The deviation from the nuclear charge radius is evaluated by calculating the Dirac equation for a nucleus with a certain radius r, taken from experimental measurements [74]. This is limited based on the actual charge distribution, of which typically only the leading order r^2 is known precisely. Therefore, the used model for the distribution can change Δg_{FNS}, and hence must be considered in error-estimation. Note that there is ongoing effort to better understand the charge density of the nucleus [75–77]. For example, in Ref. [61] nuclear structure calculations are performed to obtain realistic proton distributions for a more accurate prediction of the FNS contribution.

Overall the finite nuclear size (FNS) correction Δg_{FNS} has two sources of uncertainty: One from the experimental uncertainty of the charge radius, and one from the used model [76]. In the simplest case, the model uncertainty is estimated by comparing two different models and using the difference as an estimate for the uncertainty [28, 72].

Similar to the correction of the Breit term, FNS must be also corrected for the radiative QED terms by calculating the interaction including the finite nuclear size [76].

[3] From private communication with Bastian Sikora

2.2.3 Nuclear Recoil

Another correction is that of the nuclear recoil. Since the nucleus is not stationary, this changes the wave function, and therefore the g factor. This correction is calculated as an expansion along m_e/M. The first order $(m_e/M)^1$ is known to all orders in $Z\alpha$, while higher orders are only calculated partially [78]. Additionally one must consider the recoil correction to the radiative terms. These are typically called QED recoil. Overall, the recoil correction to the g factor $\Delta g_{\mathrm{Recoil}}$ can be described as a three-fold series expansion along m_e/M, $Z\alpha$ and α [39]. In the here presented tin measurement only the first order $(m_e/M)^1$ of the non-radiative correction contributes significantly (see Tab. 11.1).

This completes the description of the g factor of hydrogen-like ions[4]. For many-electron systems, the additional interaction between the bound-electrons must be considered as well.

2.3 Electron-Electron Interaction

For simplicity these can be separated into two terms: The electron-structure effects, and the QED screening effects, namely those including radiative corrections. Both of these are described as an additional expansion along $1/Z$. The corresponding Feynman diagrams include photon exchange between the bound electrons, with the amount of photons exchanged corresponding to the exponent of the denominator. Thus, in first order, the size of the electron-structure correction scales with $1/Z$. This is interesting, as this means that in light systems this contribution is limiting the precision of the prediction in lithium-like systems. In heavier systems such as tin, the strong $(Z\alpha)^6$ scaling of the uncertainty of two-loop QED effects is dominating instead, at least in lithium-like systems [64, 79]. In boron-like system though, the uncertainty is limited at all Z by the uncertainty of the electron structure [62].

Two ways are being pursued to calculate the contributions from the electron-electron interaction: One is rigorous in the QED corrections, meaning an all-order calculation of the $Z\alpha$ terms, but the $1/Z$ terms have to be addressed individually. The second so-called non-relativistic approach includes electron-electron interaction exactly, but has to be calculated perturbatively for the relativistic effects scaling to first order with $(Z\alpha)^2$. Typically to achieve highest precision in the prediction, a combination of both is used. As of now, the electron-structure effects can be calculated rigorously in zeroth, first and second order in $1/Z$, meaning they are calculated to all orders in $Z\alpha$, higher orders are only evaluated to the $(Z\alpha)^2$ term [57, 58, 80].

The simplest way to calculate these effects is to start with the Coulomb field of the nucleus, then calculating the perturbation by the other bound electrons individually. An alternative is to use so-called screening potentials. This quantitatively describes the screening from the closed inner shell(s) by combining the potential from their charge distribution with the binding potential of the nucleus. With this, the convergence in the $1/Z$ expansion changes. For example the core-Hartree potential is derived from the electron distribution of the closed $1s$ shell [81]. This is helpful, as already a large part of the electron-electron interaction is included in the screening potential, resulting in small coefficients for the higher orders in $1/Z$. This is not the case with the Coulomb potential. Nonetheless, with a rigorous treatment of the electron-electron interaction, any starting potential should converge towards the same result. Thus comparison of different screening potentials provide a consistency check enabling to estimate the uncertainty of the calculations.

In the current state-of-the-art calculations, QED screening effects are calculated rigorously for the zeroth and the first order in $1/Z$, the second order only to first order $(Z\alpha)^2$.

[4] At least for those with zero nuclear spin

Higher-Order Zeeman effects

Thus far only Feynman diagrams with a single interaction (photon-exchange) with the external magnetic field were considered, which is the first order Zeeman effect, that scales linearly with the magnetic field. Higher orders exist as well, which are described by Feynman diagrams with multiple photon-exchange with the external magnetic field. In electron transitions between $m_j = \pm 1/2$ all even order terms cancel because both states are shifted equally [82]. The higher odd orders are quite small[5] and can therefore be neglected in the here presented study, especially in the hydrogen- and lithium-like cases [83]. Note that in light boron-like systems these can be significant for low Z due to the mixing of the two nearby levels $2p_{1/2}$ and $2p_{3/2}$, [26]. Nonetheless, at high-Z, this contribution quickly reduces in size, becoming irrelevant for the here presented measurement of boron-like tin [84].

[5] This is the case for the 4-Tesla magnetic field in which the presented measurements are taking place.

Chapter 3

Penning-Trap Spectroscopy of Bound-Electron g Factors

After introducing the general concepts for the theoretical description of the bound electron g factor, this chapter discusses the methods applied to perform the high-precision g-factor measurements. It will focus on the techniques relevant for the study of g factors of electrons bound in highly charged ion (HCI), but can also be used to measure nuclear g factors or even electron g factors in hydrogen molecular ions, as shown by the work of my colleague Charlotte König. Furthermore, the discussion is limited to highly charged ions without nuclear spin, although there is a significant overlap of methods with these (and other) atomic systems.

3.1 g-Factor Measurement Concept

The general idea to determine the g factor of a HCI in a Penning trap makes use of the magnetic field, used to trap the charged particles on a circular orbit. The so-called cyclotron motion has an oscillation frequency of

$$2\pi\,\nu_\mathrm{c} = \frac{q}{M}B_0. \tag{3.1}$$

Here, q/M is the particles charge-to-mass ratio and B_0 the magnetic field assumed to be homogeneous in z direction $\boldsymbol{B} = B_0\boldsymbol{e}_z$. In the very same magnetic field, the electron spin interacts with the field. The energy of the two distinct orientations of the spin-$\frac{1}{2}$ particle is given by $\Delta E = h\,\nu_\mathrm{L}$, where the Larmor frequency ν_L is defined as:

$$2\pi\,\nu_\mathrm{L} = \frac{g}{2}\frac{e}{m_\mathrm{e}}B_0 \tag{3.2}$$

where e/m_e is the electron charge-to-mass ratio. Both the cyclotron frequency and the Larmor frequency are proportional to B_0. One can therefore describe the g factor magnetic field independently as follows:

$$g = 2\frac{\nu_\mathrm{L}}{\nu_\mathrm{c}}\frac{q}{e}\frac{m_\mathrm{e}}{M}. \tag{3.3}$$

This equation shows that a measurement of the ratio $\nu_\mathrm{L}/\nu_\mathrm{c}$, also called Γ_0, combined with the literature values for the charge-to-mass ratios of the electron and ion, gives the g factor of the system. This experimental result can then be compared to the prediction by QED, providing a stringent test of this fundamental theory. Alternatively, if the theory is assumed to be correct, one is able to extract another value from the equation. Recently, this has been used to improve the mass

of the Ne-22 isotope extracted from the g-factor measurement of hydrogenlike $^{22}Ne^{9+}$ [29]. More famously, the electron mass has been measured using hydrogen-like carbon [24]. By measuring Γ_0 of the hydrogen-like carbon ion, where the theoretical prediction of g is very accurate and the mass (in u) is well defined[1], one can extract the electron mass. At the time its precision surpassed any prior measurement, and only recently measurements on molecular hydrogen ions which are sensitive to the electron-to-nucleus mass ratio, achieve a higher precision when combined with the mass of a proton and a deuteron [85].

Following Eq. (3.3), to determine the g factor, ν_L and of ν_c must be measured simultaneously to avoid systematic effects from magnetic field instabilities like drifts. In the presented work the magnetic field is about 4 Tesla, which results – for an ion with a q/M of roughly $1/2$ (in units of e per u) – in a cyclotron frequency slightly lower than 30 MHz. The bound electron g factor, in systems where the valence electron is the single occupant of an s shell, the g factor is around 2, rather close to the free electron g factor, due to the electron orbit quantum number l being 0. This results in a Larmor frequency in the order of 110 GHz. Since this frequency is quite fast, in state-of-the-art experiments residual magnetic field fluctuations quickly make the spin precession incoherent. While measuring the cyclotron frequency ν_c, a microwave irradiation is applied to the ion. If the microwave frequency ν_MW is sufficiently close to the Larmor frequency, the transition is driven, and the spin can flip. By probing multiple ratios $\Gamma = \nu_\mathrm{MW}/\nu_\mathrm{c}$ the spin-flip probability curve is recorded. Proper data analysis provides then a value for the center of the resonance, corresponding to Γ_0. The following sections in this chapter will explain briefly how the Penning trap works, and how the particle can be controlled in order to determine the free-space cyclotron frequency, as well as probe the ratio Γ.

3.2 Penning-Trap Physics

Hans Dehmelt who was awarded the Nobel Prize in Physics in 1989 for his contributions towards the measurement of the free-electron g factor pioneered the Penning Trap for high-precision measurements. Its advantage lies in the extremely stable magnetic field, owing to the superconducting magnet within a very stable cryogenic environment. In this field, a charged particle is confined to the cyclotron orbit. To confine the particle in the axial direction as well, a static electric field is used. Hence, a field minimum in the z direction is required. The Laplace equation shows that to produce this we need a saddle potential, with a maximum in the radial direction[2]. To achieve an ideal harmonic oscillator in axial direction, the electric potential would therefore be a quadrupole potential with the form

$$\phi(\rho, z) = \frac{V_0 C_2}{2 d_\mathrm{char}^2} \left(z^2 - \frac{\rho^2}{2} \right). \tag{3.4}$$

Here, $\frac{V_0 C_2}{2 d_\mathrm{char}^2}$ is a prefactor describing the trap strength as a function of the applied voltage V_0, d_char is a geometrical factor called the characteristic length, C_2 is the normalized[3] second order field coefficient. To produce such a harmonic potential there are multiple ways, most commonly used are hyperbolic designs or a stack of cylindrical electrodes. At Alphatrap a cylindrical trap is used. This chapter will therefore focus on these, without going into details on the other possible geometries.

Cylindrical traps are rather simple, consisting only of a stack of electrodes separated by some

[1] The neutral carbon mass is the mass standard (in units of u), therefore the ion mass is only limited by the uncertainties for the binding energies and missing electrons.

[2] We assume cylinder symmetry.

[3] More specifically, here normalized means unitless, with the normalization factor coming from the characteristic length d_char^2.

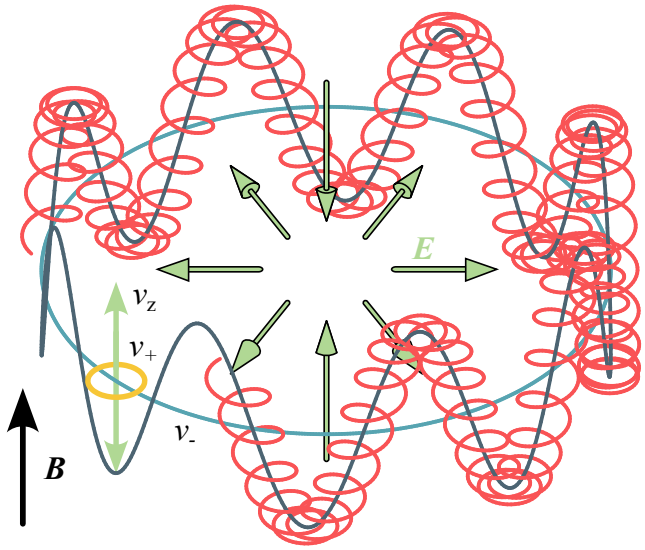

Fig. 3.1: Particle trajectory in a Penning trap. The motion can be described by three oscillations, modified cyclotron ν_+, axial ν_z and magnetron ν_-. The frequencies and amplitudes for the modes in the figure are chosen for visibility, and are far from what is typical for the trap. The electric field gradient is forming a saddle potential with the from shown in Eq. (3.4).

dielectric material. Each electrode has typically the same radius, which will be used as the characteristic constant d_{char} throughout the thesis[4].

3.2.1 Particle Motion

It follows from Eq. (3.4) and the resulting equation of motion that the axial mode has an oscillation frequency of

$$\nu_z \times 2\pi = \sqrt{\frac{qV_0C_2}{M\,d_{\mathrm{char}}^2}}. \tag{3.5}$$

Without going into too much detail, as the trap dynamics have been explained very detailed in many theses, see e.g. Refs. [86, 87], the combination from electric and magnetic field will result additionally in a perturbation of the cyclotron motion. Its frequency will decrease, and a second radial motion from the $\boldsymbol{E} \times \boldsymbol{B}$ term appears as a drift around the trap symmetry axis. The frequencies of the two radial modes, called modified cyclotron ν_+ and magnetron motion ν_-, can be calculated by

$$\nu_\pm = \frac{\nu_c}{2} \pm \frac{1}{2}\sqrt{\nu_c^2 - 2\nu_z^2}. \tag{3.6}$$

Further relations follow from the equation of motion, for details it is referred to previous work, e.g. [25]. The three frequencies ν_+, ν_z and ν_- typically follow the hierarchy

$$\nu_+ \gg \nu_z \gg \nu_-. \tag{3.7}$$

The frequency hierarchy is relevant for the presented high-precision measurement of the cyclotron motion, as the three motions, as shown by the invariance theorem [88], are connected to the free-space cyclotron frequency via

$$\nu_c^2 = \nu_+^2 + \nu_z^2 + \nu_-^2. \tag{3.8}$$

The theorem shows that this equation is true even when the electric and magnetic field axis are not aligned, and that further an elliptical deviation from the cylinder symmetry of the electric potential is compensated. Due to the hierarchy of the frequencies, ν_c is the most sensitive to ν_+ as the relative dependence on ν_z and ν_- is reduced by a factor ν_z/ν_c^2 and ν_-/ν_c^2 respectively.

[4] Inherited from hyperbolic traps, in cylindrical traps, the characteristic length is typically defined as $d_{\mathrm{char}}^2 = 1/2\left(z_0^2 + r_0^2/2\right)$, where r_0 is the trap radius, and z_0 some characteristic length of the geometry. d_{char} was typically close to the trap radius, and as this is just an arbitrary scaling factor, the convention here will be that $d_{\mathrm{char}} = r_0$.

The energy inherent to each mode, as derived in example in [89], are as follows:

$$\begin{aligned} E_+ &= \frac{1}{2}M\left(\omega_+^2\hat{r}_+^2 - \frac{1}{2}\omega_z\hat{r}_+^2\right) \approx \frac{1}{2}M\omega_+^2\hat{r}_+^2, \\ E_z &= \frac{1}{2}M\omega_z^2\hat{r}_z^2, \\ E_- &= \frac{1}{2}M\left(\omega_-^2\hat{r}_-^2 - \frac{1}{2}\omega_z^2\hat{r}_-^2\right) \approx -\frac{1}{4}M\omega_z^2\hat{r}_-^2. \end{aligned} \tag{3.9}$$

The different $\hat{r}$ are defined as the classical amplitudes of the three particle motions. Typical energies in the presented work are below 1 eV. This stems from the modes being thermalized to the cryogenic apparatus, which sits at a temperature of roughly 5 K, as explained in an upcoming section.

3.2.2 Systematic Effects

To achieve a high accuracy on the measurement of the g factor, not only a low statistical uncertainty must be reached, but also the systematic effects must be understood, and it must be estimated how large their impact can be in the worst-case scenario. In Chapter 9, a complete analysis of the systematic effects for the here presented g-factor measurements is presented. Table 9.3 summarizes the measurement specific results a complete table of all known systematic effects affecting. The following sections will give a brief overview on the most dominant systematic effects, caused by the imperfect trap.

Electric Field Anharmonicity

In reality, the electric potential can not be a perfect harmonic oscillator. Hence, higher-order terms have to be taken into account. The field will not follow a perfect parabola due to a variety of sources such as patch potentials, imperfect design and manufacturing errors. The potential (reduced to the field along the z axis) can be described in a more general form as follows:

$$\phi(z) = \frac{1}{2}V_0 \sum_{i=0,1\ldots}^{\infty} \frac{C_i z^i}{d_{\text{char}}^i} \tag{3.10}$$

Note that a more general solution $\phi(z,\rho)$ exists, but is omitted here since it has been described in detail in the past [86]. Due to these higher-order perturbations of the ideal field, the frequency becomes a function of the motional amplitudes. This can be calculated analytically for the cylinder-symmetric system. The dominating terms that produce the largest systematic uncertainty on the here presented measurements are [90]:

$$\begin{aligned} \frac{\Delta\nu_z}{\nu_z} &= \frac{C_4}{C_2}\frac{3}{4d_{\text{char}}^2}\left(\hat{z}^2 - 2\hat{r}_+^2 - 2\hat{r}_-^2\right), \\ \frac{\Delta\nu_\pm}{\nu_\pm} &= \mp\frac{C_4}{C_2}\frac{3}{2d_{\text{char}}^2}\frac{\nu_\mp}{\nu_+ - \nu_-}\left(2\hat{z}^2 - \hat{r}_\pm^2 - 2\hat{r}_\mp^2\right), \\ \frac{\Delta\nu_z}{\nu_z} &= \frac{C_6}{C_2}\frac{15}{16d_{\text{char}}^4}\left(\hat{z}^4 + 3\hat{r}_+^4 + 3\hat{r}_-^4 - 6\hat{r}_+^2\hat{z}^2 - 6\hat{r}_-^2\hat{z}^2 + 12\hat{r}_+^2\hat{r}_-^2\right), \\ \frac{\Delta\nu_\pm}{\nu_\pm} &= \mp\frac{C_6}{C_2}\frac{15}{8d_{\text{char}}^4}\frac{\nu_\mp}{\nu_+ - \nu_-}\left(3\hat{z}^4 + \hat{r}_\pm^4 + 3\hat{r}_\mp^4 - 6\hat{r}_\pm^2\hat{z}^2 - 12\hat{r}_\mp^2\hat{z}^2 + 6\hat{r}_+^2\hat{r}_-^2\right). \end{aligned} \tag{3.11}$$

For their derivation and further equations it is referred to the work of Jochen Ketter, who quantified the first-order shifts, as well as many second-order shifts [90].

These effects can cause a problem, since they result in a systematic shift of the free-space cyclotron frequency ν_c extracted from the three individually measured motions. To minimize the anharmonicity, a couple of measures are taken, starting with an optimized electrode geometry, such that the dominant coefficients are small to begin with. Furthermore, by implementing a set of correction electrodes, the harmonicity can be further tuned. In this process, the shift is characterized by measuring the frequency shifts as a function of the motional amplitudes, followed by compensation of these shifts via the correction electrodes.

Thus far neglected were odd-order coefficients, which only indirectly produce a frequency shift. In first order they only produce shift of the axial position as a function of the motional amplitude, which then in second order causes a shift frequency. Thus, frequency shifts due to odd-order anharmonicities scale only with coupled terms, i.e. C_3^2, $C_3 \times B_1$, $C_3 \times C_5$ and so on. Higher terms starting with C_5 are usually to small to affect the measurement, hence they can be neglected.

Magnetic Field Inhomogeneity

Similar to the electric field anharmonicity, imperfections in the real world result in a deviation of the magnetic field from the ideal case of a position independent $\boldsymbol{B} = B_0 \boldsymbol{e}_z$. They can be written[5] as a series expansion of the magnetic field with the higher-order coefficients B_i:

$$B(z) = \sum_{i=0}^{\infty} B_i z^i. \tag{3.12}$$

This deviation from the ideal case can result in certain systematic shifts, although since they act both on the Larmor and the modified cyclotron frequency, such effects drop out to first order when ν_c is measured simultaneously with the microwave injection. Additionally they cause a change in the lineshape of the Γ_0 resonance, shifting the center of the resonance [91]. In the here presented measurements of highly charged tin, this effect is negligible[6] because of the exceptionally small residual field inhomogeneity combined with the small thermal radii. Therefore, a detailed description here is avoided, and the interested reader is referred to previous work [86, 91, 92].

Image-Charge Shift

In electrostatics one commonly employed method is that of image charges. It enables to calculate the produced electric field of a charge near a conductive surface. Following this approach, the field experienced by the particle is perturbed due to the interaction with the surrounding electrodes. This has been studied extensively in the past [93] and the resulting shift on the axial frequency for a cylindrical trap can be calculated via[7]

$$\frac{\Delta\nu_c}{\nu_c} \approx \xi \frac{M}{4\pi\epsilon_0 B_0^2 r_0^3}, \tag{3.13}$$

with ξ a geometry factor extracted from numerical simulations for the specific geometry, in this case for the cylindrical trap with the slits between the electrodes. In the measurement trap of the ALPHATRAP setup ξ has a value of 0.9935 [94, 95]. Due to tolerances in the manufacturing and the unknown ellipticity, the correction will inhibit some error, which is typically chosen as 5 % of the overall shift, which is shown to be reasonable in Ref. [93]. Eq. (3.13) shows directly the M/r_0^3 scaling. So for large masses, and small traps, this shift can be quite large. ALPHATRAP was built

[5] Again simplified for the solution along the z-axis.

[6] For the here presented results, the effects are less than 0.001 ppt.

[7] For sign clarity, the image charge shift reduces the measured frequency, meaning that the unperturbed free-space frequency is higher than measured.

with high-precision heavy ion measurements in mind. Hence, the Precision Trap, as introduced later, has an inner radius $r_0 = 9\,\mathrm{mm}$. Nonetheless, in the heaviest systems like hydrogen-like lead, this shift still results in a relative contribution of 2.6×10^{-10}.

Relativistic Correction

Another effect of relevance is the relativistic correction. This effect does not drop out in the ratio Γ, as it is reduced on the Larmor frequency by about a factor of $\nu_\mathrm{L}/\nu_\mathrm{c}$ [86, 92], due to the Lorentz boost into the rest frame of the atom. Thus, the shift to the cyclotron frequency must be taken into account. The calculation of it can be treated classically using a perturbative approach as done in Ref. [96], where the relativistic equations of motions are solved to first order. This shows that the simple treatment via relativistic mass increase is factually incorrect, especially for the mass increase due to the axial amplitude. Nonetheless, typically a large error is assumed on the motional amplitudes, and therefore on the speed of the particle. This makes the simple estimate via relativistic mass increase accurate enough, and no further treatment is needed here. Hence, the relativistic corrections is done by shifting the measured cyclotron frequency higher according to the formula

$$\frac{\Delta\nu_\mathrm{c}}{\nu_\mathrm{c}} \approx 1 - \frac{1}{\gamma}, \tag{3.14}$$

with $\gamma = \left(1 - \hat{v}^2/c^2\right)^{-1/2}$ being the Lorentz factor. $\hat{v}$ is the velocity of the particle, which in the measurements presented here is in good approximation $\omega_+ r_+$, due to the hierarchy of the motional frequencies and their typical amplitudes.

3.3 Particle Detection

All the shifts and uncertainties discussed so far are often in the milli-Hertz range. Thus far neglected were the methods enabling to measure the particle motion with the precision where such tiny deviations have to be taken into account. This section will address the various methods used to determine motional frequencies of the particle in the trap. This has been addressed in many previous works, thus here the goal will be to give a more general description to introduce the basics needed for the following work. The curious reader is referred to previous work. For example pioneering work can be found in Ref. [97]. More recent descriptions closer to the current state-of-the-art can be found in Ref. [86, 87, 92].

Axial Frequency

In the presented work, particle detection in the trap was done exclusively by detecting the image currents that the moving charge induces in the neighboring electrodes. This is given by the ions charge q, the *effective electrode distance* d_eff and the velocity of the ion $\dot{z}(t)$

$$I(t) = \frac{q}{d_\mathrm{eff}}\dot{z}(t). \tag{3.15}$$

Here, the d_eff is the inverse of the normalized[8] gradient of the potential generated by the electrode of interest at the position of the ion. This means, with a larger gradient at the ion position, the induced currents increase. It follows that to detect a certain motion, symmetry breaking of the electrode geometries is required, in order to have a potential gradient at the ion position. Thus, to

[8] The normalization is done by dividing the electric field generated by the electrode at 1 V by 1 V

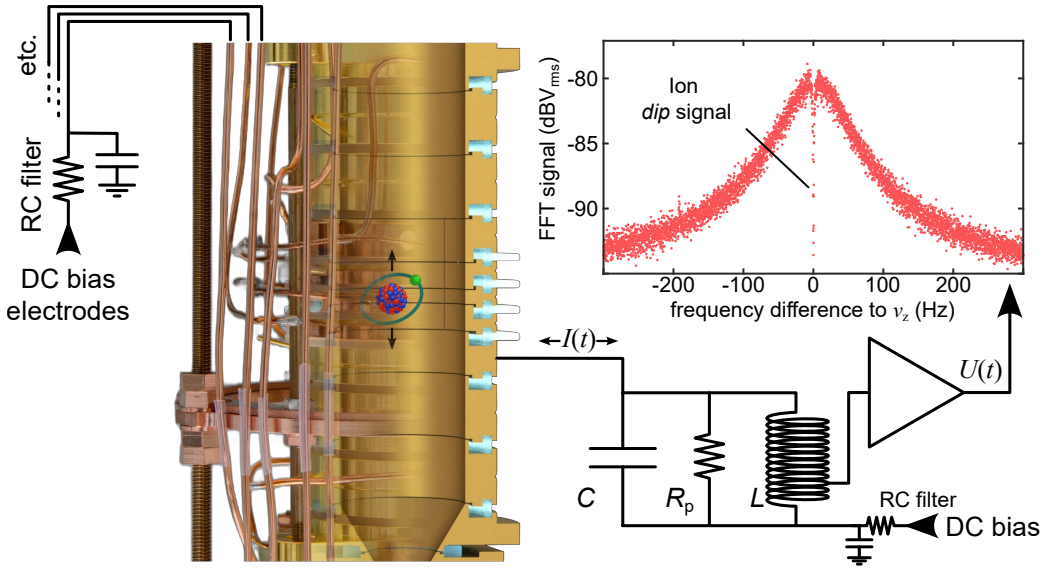

Fig. 3.2: Simplified schematic showing the connection of the LC tank circuit to the trap and the cryogenic amplifier. The ion induces a current in the electrode, which is connected to the resonator, resulting in a coupling between both if in resonance. The trans-impedance amplified signal is then fed to an FFT analyzer, where the resonator spectrum is visible along with the ion signal, a dip in the spectrum at the frequency of the particles axial oscillation frequency. The photo on the left was kindly provided by Ralf Lackner.

detect axial motion, an electrode[9] above or below the trap center is chosen for pickup. For radial modes, one similarly needs an electrode which is split along the x-z plane to achieve symmetry breaking in y direction. As a side note, this is closely related to the requirements for the excitation (or coupling) of particle motions via radio-frequency fields on a trap electrode, as similarly these need a gradient in the potential at the ion position.

Returning to the induced currents and their detection, it can seen from Eq. (3.15) that the typical currents generated are of the order of a few femto amperes. To detect this oscillating current, one employs a resonant LC circuit which with its (effective) parallel resistance[10] produces a voltage drop that can be further amplified and Fourier analyzed to detect the particles oscillation frequency. Fig. 3.2 shows the electrical connection used in the presented work in the Precision Trap (see Chapter 5 for further details). The LC circuit is a hand-made superconducting coil in a superconducting housing. As an example, in one of the traps, the circuit has an inductance of 2.1 mH and a capacity of roughly 28.4 pF. From this, its resonance frequency is at 652 kHz[11]. The overall impedance Z is given by

$$Z(\omega) = \frac{R_\mathrm{p}}{1 + iQ(\frac{\omega}{\omega_\mathrm{res}} - \frac{\omega_\mathrm{res}}{\omega})}. \tag{3.16}$$

Using a superconductor for the coil and the housing reduces the losses in the circuit, increasing the effective parallel resistance R_p and thus the $Q = {}^{R_\mathrm{p}}/_{\omega_\mathrm{res} L}$ value, which describes the width of the resonance.

If now the axial frequency of an ion in the trap is in resonance with the circuit, the induced current from the ion produces a voltage drop over the real part of the impedance. The ion dissipates

[9] Sometimes also multiple electrodes, connected by capacitors, are used.
[10] This is analog to a series LC circuit with the losses being described as a series resistance. So the parallel resistance is a different way to represent the losses in the circuit.
[11] $\omega_\mathrm{res} = {}^1/\sqrt{LC}$

energy into the resonator until it is in thermal equilibrium with the Johnson noise of the resistance. The resonator is attached to a cryogenic amplifier, located close to the resonator and the trap for minimized losses in the wires. Around the oscillation frequency ω_{res}, output exhibits the johnson noise density rising above the amplifier noise floor. For the here used cryogenic amplifiers this is typically in the order of $0.5\,{}^{\mathrm{nV}}/\sqrt{\mathrm{Hz}}$ to $1.5\,{}^{\mathrm{nV}}/\sqrt{\mathrm{Hz}}$. With the particle thermalized and in resonance, the ion, which can be described by an LC resonance circuit itself, *shortens* the resonator, and the signal at the ion frequency drops, showing a distinctive *dip* feature. The width of this dip is related to the time constant of the resonator ion coupling

$$\gamma = \frac{q^2 \mathrm{Re}(Z)}{2 m d_{\mathrm{eff}}^2}, \tag{3.17}$$

with the already introduced charge q, mass M, d_{eff} and Z the impedance of the tank circuit. From this it follows that the signal strength is a function of charge-squared to mass ratio, as well as the dissipative (real) part of the impedance, and the effective electrode distance. With the well-understood behavior, the line shape is known, and fitting of the noise spectrum is used to determine the oscillation frequency of the ion. The overall lineshape is then given by:

$$u_n^2 = A\left(1 + \left(Q\left(\frac{\omega}{\omega_{\mathrm{res}}} - \frac{\omega_{\mathrm{res}}}{\omega}\right) - \frac{\omega}{\tau(\omega^2 - \omega_{\mathrm{z}}^2)}\right)^2\right)^{-1} + (u_n^{\mathrm{amp}})^2\,. \tag{3.18}$$

Here, A is the amplitude, which results from the (effective) temperature and the wiring of the resonator. To acquire the ions oscillation frequency, Eq. (3.18) is typically fitted in units of $\mathrm{dBV}_{\mathrm{rms}}$. On top of that, a frequency dependence of the transfer function of the amplifier is taken into account by adding a frequency dependence to the noise in the form of a polynomial around ω_{res}. As later discussed in the systematic effects sections, the degree of the polynomial is varied, to test the accuracy of the fitted resonator frequency.

Such electric circuitry can be built for the axial and for the modified cyclotron motion. For the magnetron motion, the negative temperature (see Eq. (3.9)) disallows such detection methods. For the here described measurements only axial resonators were used. With some simple tricks detection and measurement of radial modes is possible with one single axial detector.

Radial Frequencies

For this, coupling of the radial modes to the axial mode is done with an appropriate (quadrupole) radio frequency (RF) field at one of the sidebands ($\nu_z \pm \nu_\pm$). In the simplest case the *red* sideband ($\nu_+ - \nu_{\mathrm{z}}$ and $\nu_{\mathrm{z}} + \nu_-$), this leads to a continuous Rabi-type transfer of the action between the two modes where the quantum number of one mode is transferred into the other and vice-versa. Combined with the axial detector, thermalization of the radial modes with the axial mode can be achieved. As the energy transfer is effectively an exchange of motional quanta, the energy after thermalization is scaled by the radial-to-axial frequency ratio. Hence the temperature $T_\pm = {}^{E_\pm}/_{k_{\mathrm{B}}}$, after such so called *sideband* cooling, is $T_\pm = {}^{\nu_\pm}/_{\nu_{\mathrm{z}}} T_{\mathrm{z}}$. In this case, the axial dip in the noise spectrum splits into two dips, which can be exactly described as an avoided crossing. Knowledge of the axial frequency ν_{z}, the two dip frequencies during sideband cooling (ν_{l}, ν_{r}) and the frequency of the quadrupolar field ν_{rf}, the two radial frequencies can be extracted as:

$$\nu_\pm = \nu_{\mathrm{rf}} \mp \nu_{\mathrm{z}} \pm \nu_{\mathrm{l}} \pm \nu_{\mathrm{r}}. \tag{3.19}$$

This method, also called *double-dip* method, is used for the magnetron motion, as with the invariance theorem and the strong scaling between the modes, its accuracy is much less crucial for the determination of ν_c. For the modified cyclotron mode on the other hand, utmost precision and accuracy is needed. To achieve this better approaches are available, these are overall slower since they typically require a lot of overhead work, but their shot-to-shot precision is far above the noise-averaging approach.

The *blue* sidebands ($\nu_+ + \nu_z$ and $\nu_z - \nu_-$) on the other hand result in coupling on the motion combined with a exponential heating of both modes still obeying the temperature scaling $T_\pm = {}^{\nu_\pm}/_{\nu_z} T_z$.

3.3.1 Pulse 'n Amplify

As mentioned earlier, other methods rather than the *double-dip* approach exist. Also known as PnA, this technique is a phase sensitive approach to directly measure the cyclotron oscillations of the radial modes in the trap [98]. Briefly summarized, the particles modified cyclotron motion[12] is excited to some radius significantly above the thermal radius, imprinting a starting phase onto the motion. Afterwards, the particle evolves in phase-space rotating around the z axis. After some evolution time t_{evol}, the particle accumulated a certain phase shift

$$ {}^{\phi}/_{2\pi} = t_{evol}\nu_+. \tag{3.20} $$

In order to read this out, as described above, the available axial detector is used. The phase information is transferred using the above described coupling pulses. In the predecessor Pulse 'n Probe (PnP), the *red* cooling sideband is used. With a π pulse, the complete phase (and space/radius) information is transferred from one mode to the other, resulting in a cold cyclotron mode, but a hot axial mode, swapping the conditions during the free evolution time. This has the disadvantage, that the final signal strength, which scales with the axial radius, is dependent on the initial modified cyclotron radius, which might cause larger effects from special relativity, due to the higher velocity at higher amplitude. PnA is meant to overcome this issue by not *swapping* the information between both modes, but by coupling and amplifying them. This can be done simply using the *blue* sideband. For the modified cyclotron mode this is then $\nu_+ + \nu_z$. If the signal strength of the modified cyclotron mode is large enough[13], the phase information in the axial phase is after coupling dominated by the phase of the cyclotron mode, independent of the final amplitude. To then measure the phase of the axially hot particle, the axial detector is used. It interacts with the electronic circuit, and the energy is dissipated in the detector via the parallel resistance R_p. This produces a strong detectable signal in the FFT spectrum of the detector from which one can extract the phase of the signal, which is directly given by the particle axial phase as imprinted from the modified cyclotron phase in the coupling pulse. The noise floor of the detector adds a certain amount of jitter, making a large signal-to-noise ratio (SNR) advantageous, as described in detail in Ref. [86]. In resonance the SNR, so the peak prominence[14] of this signal is:

$$ \mathrm{SNR} \approx \frac{q\omega_z\sqrt{R_p t}}{d_{eff}\sqrt{4k_B T}} z_{rms}, \tag{3.21} $$

[12] This also works with the magnetron motion, but since this was not used for the presented work, the text will refer predominantly to the modified cyclotron motion.

[13] This requires the amplitude $\hat{r}_+$ to be significantly larger than the $\hat{r}_z\sqrt{\nu_z/\nu_+}$, with $\hat{r}_z$ as the thermal radius

[14] From geological descriptions of mountains this describes the height difference of the peak to the valley. Here it refers to the peak signal above the noise floor of the circuit

with t as the signal readout time, and the other terms as defined prior. This shows that various options exist to improve the signal. Trivially, a higher amplitude z_{rms} causes a better signal, and hence better readout. Nonetheless, this cannot be scaled arbitrarily as trap anharmonicities become more prominent at higher radius which could cause a systematic shift along with an increased jitter of the signal. In the presented measurement of tin this is a small effect, as with the high q of the three measured charge states, the signal increases, and large SNR can be achieved already at small radii. This becomes more critical when working with lighter ions. For measurements with these one could naively assume to simply increase $\sqrt{t}$ accordingly. This gets difficult with the square-root scaling. Additionally, as effectively the axial frequency is detected during t, its frequency stability plays a role and might cause additional instability of the readout phase. Typical readout times used at ALPHATRAP are between 50 ms and 0.5s, depending on the ion and the required SNR. For the used tin measurements, a readout time of 128 ms was used. Typical SNR values for tin were between 20 dB and 25 dB, which results in very little additional phase noise from the amplifier.

For a complete frequency determination, a single phase measurement is not enough. In its outcome, a single phase ϕ, there is no complete information on the cyclotron frequency. Nonetheless, it can be used for relative measurements, in example to study the shot-to-shot stability. One could repeat multiple measurements with the same parameters, and compare the change over time. To extract the absolute frequency, additional steps have to be taken. For once, there is no perfect information on the starting phase after the initial excitation of the modified cyclotron mode. Thus, a reference phase[15] is measured to extract the phase difference between the short time[16] and the long evolution time. For this, the measurement time for this reference phase should be short enough so that the phase becomes essentially independent of magnetic field fluctuations. The long time on the other hand is chosen such that it is dominated by it. Then it is a near perfect measurement of the magnetic field during the phase accumulation of the long evolution time. Since the phase is measured modulo 2π, but the ion performs many oscillations within the long evolution time, one needs to determine the integer number of completed cycles additionally. To track this many cycles, one needs a good initial guess of the frequency to know the amount of rotations the ion performs during the free evolution time. This is often called n-determination, in the sense that one determines the amount of revolutions n that the ion performs in the long evolution time for correct unwrapping of the final phase difference:

$$\nu_+ = \frac{\phi_{\mathrm{ref}} - n \times 2\pi - \phi_{\mathrm{long}}}{2\pi(t_{\mathrm{long}} - t_{\mathrm{ref}})}. \tag{3.22}$$

The phases $\phi_{\mathrm{ref/long}}$ are here the measured axial phase after imprinting the modified cyclotron phase onto these. As a sidenote, one would naively think that this is just the slope between the two phases versus the evolution time, and not as in this equation the negative slope. This is due to the coupling between axial and modified cyclotron. So unintuitively, the measured axial phase gets smaller for an increasing modified cyclotron phase. The n is then taken from the guessed frequency, the reference phase, and the evolution times

$$n = \mathrm{round}\left(\nu_+^{\mathrm{guess}}\,(t_{\mathrm{long}} - t_{\mathrm{ref}})\right). \tag{3.23}$$

As the very first guess of the frequency, the *double-dip* method is used. As an example, if this has a precision of 100 mHz, correct unwrapping is only possible for times shorter than a few seconds, as the n uncertainty $\Delta n = 0.1\,\mathrm{Hz} \times 3\,\mathrm{s} = 0.3$ is not far from incorrect unwrapping. Thus, in order

[15] Typically multiple reference phases with the same evolution time are measured to average down their inherent readout jitter, which would increase the precision of the ν_+ measurement.

[16] In this work it is in nearly all cases 0.2 s.

to measure for longer times than given by the *double-dip* limit, additional phases are measured for intermediate evolution times, enabling to get a better prediction of n for long evolution times. As later discussed, these intermediate phases give also great information on potential systematic effects. One thing that also has to be considered, which limits the possible range of usable evolution times is the magnetic field stability. If the measured shot-to-shot phase jitter is too high, correct unwrapping is not possible. So for optimal settings one would choose a long evolution time, where the magnetic field jitter dominates, and readout jitter plays a minor role, while still being far below a 90° phase shot-to-shot stability. From here on, jitter is defined as the standard deviation of consecutive phase/frequency measurements. In the presented measurements, typical numbers here are 6° readout jitter, and 12° jitter at 5.2 s as the longest evolution time. With the later introduced self-shielding cylinder, the magnetic field stability improved, and with $^{12}C^{5+}$ a stability of 24° was observed at 40 s evolution times.

3.4 Spin-State Detection

To complete the required set of methods for a g-factor measurement, the detection of the Larmor frequency is presented here. In the 4-Tesla magnetic field of ALPHATRAP this is typically around 110 GHz for HCI with a single electron in an s valence shell, and around 36 GHz for boron-like systems due to the factor three smaller g factor from the non-zero orbital angular momentum. Irradiating a microwave at the Larmor frequency excites the transition and possibly flips the spin of the particle when in resonance. Probing multiple microwave frequencies will result in a spin-flip probability distribution, with the center being at the Larmor frequency of the transition. To do this in practice, one needs an appropriate microwave source, and a way to subsequently determine whether a change of the spin-state occurred.

Continuous Stern-Gerlach Effect

To do this non-destructively, one can make use of the Stern-Gerlach effect. In a magnetic field gradient, the particle with non-zero spin will experience a force. This will depend on the orientation of the spin along the magnetic field axis. This two-level system, from now on addressed as spin up and spin down, thus has a low-field seeking state, and a high-field seeking state. A magnetic bottle, a magnetic field minimum in z direction, therefore results in an inwards or outwards facing force dependent on the spin state. This means the particle oscillates at a different axial frequency for the two spin states. Thus one can test the state by measuring the frequency of the particle. Similar to the electrons magnetic moment, the radial modes inherently have a magnetic moment, they cause an additional axial frequency shift, as in detail explained in Ref. [99]. Thus the overall frequency shift due to the magnetic moment in the bottle is given as:

$$\Delta\nu_z = \frac{B_2\hbar q}{4\pi^2 m^2 \nu_z}\left(\Gamma_0\Delta m_s + \hat{n}_+ + \hat{n}_-\frac{\nu_-}{\nu_+}\right), \tag{3.24}$$

with B_2 the second-order B-field coefficient, $\hbar$ the reduced Planck constant, q, m, ν_z, ν_+ and ν_- as introduced before. Δm_s is the change in the spin quantum number[17], and $\hat{n}_\pm$ are the radial quantum numbers. In most measurements, the cyclotron mode is thermalized as described above. Afterwards it has a random amplitude following a Boltzmann distribution. To determine therefore a spin change $\Delta m_s = \pm 1$ in the bottle, the axial frequency is measured, followed by inducing a spin change via microwave irradiation and a repeated frequency measurement. When the frequency

[17] For boron-like systems it would rather be m_j, as the descriptive s denotes the electronic state.

changed, a spin flip occurred and the direction of change provides information on the current (and prior) spin state. The B_2 used at ALPHATRAP is around $43\,\mathrm{kT/m^2}$. In example for hydrogen-like tin, the frequency jump from a spin change is roughly 300 mHz. Errors from heating rates $\dot{\hat{n}}_+$ are small as the scaling factor Γ_0 (several thousand for electron g factors of HCI) for the frequency change makes the spin state the dominating effect. Additionally, heating rates in Penning traps are typically extremely low. In example, at BASE a heating rate of around 6 quanta per hour was observed, which uses a setup similar to the one used here [100]. A quantitative measurement has not been done for the presented work, but from the observed frequency stability this does not seem to impose any limit for the determination of bound electron spin flips.

As introduced in the magnetic field inhomogeneity section, the magnetic bottle causes large systematic effects. For highest precision a measurement can therefore not be performed in such a trap.

3.5 Double-Trap Measurement

To overcome this, the by now well-established double-trap technique is used for such Penning-Trap spectroscopy measurements [20]. By using two separate trap sections, one for spin-flip detection and one for a high-precision measurement of Γ_0, limits from the inhomogeneity are overcome. During the measurement, the spin state is determined in the from now on called Analysis Trap (AT) with its magnetic bottle. In the Precision Trap (PT), precise measurement of ν_c is performed. At the same time, a microwave with frequency ν_MW is injected. If the frequency ratio $\Gamma = \nu_\mathrm{MW}/\nu_\mathrm{c}$ is in resonance with the transition, the spin can flip. This can only be detected after moving back into the AT, in order to compare the spin state before and after probing the ratio Γ in the PT. Measuring at different Γ results in a dataset of boolean information, with either successful or unsuccessful PT spin-flip attempts. Maximum-likelihood analysis is performed to determine the center of the resonance.

Chapter 4

Electron Beam Ion Trap

Electron beam ion traps (EBIT) were first developed in the eighties as a successor for the electron beam ion sources. They are a way to produce highly charged ions by electron impact ionisation. An electron beam, compressed by a strong magnetic field, ionises atoms through kinetic impact. The biggest difference between an EBIT and EBIS at the time was the compactness, and instead of using long homogeneous magnetic fields, the EBITs interaction region became smaller [45, 101]. The main advantage lies in the possibility to use a pulsed ejection with a significantly smaller spatial distribution. Nowadays, the two different names are used more interchangeably and refer typically more to the respective use of the device. EBITs refer more towards devices that make use of their trapping capabilities, in example by in-trap spectroscopy. An EBIS on the other hand is used more as a source to produce a desired charge state which would then be ejected and transported through a beamline to a desired place for further experiments. In the presented thesis, the shown devices were solely used as a source, nonetheless the specific devices will be referred to with their original name. Furthermore, as over the decades, many publications and theses covered the topic of EBITs, this section will be kept brief. The interested reader is therefore referred to the various publications and dissertations dealing with EBITs in much greater detail [45, 102–104].

4.1 Concept

To describe the processes happening within an EBIT in a bit more detailed the schematic in Fig. 4.1 will be used as a guide. Typical devices can be separated into three sections: The electron gun, the magnet/trap region and the collector section. From a cathode within the gun section, the electrons are emitted into the vacuum, and accelerated by the electric field along the z direction. Once they leave the gun, the magnetic field is steadily increasing, and they perform cyclotron oscillations around the central axis, the radius of which is decreasing with the rising field, resulting in a compression of the beam. This results in a large current density within the central drift tubes, increasing the likelihood of an electron hitting a bound electron for impact ionization. The beam then leaves the trap, and by the help of the collector coil, the magnetic field is canceled in the collector, causing the electrons to spread outwards, being captured by the collector, closing the circuit between cathode and collector. The electrons are emitted from the cathode with only a few keV[1]. Most beam acceleration is achieved by the biasing between magnet and gun/collector. Therefore the electrons are extremely fast within the trap, but slow down before being collected

[1]The reason being that they will collide with the collector heating it up by their kinetic energy, the dissipated power is then the cathode voltage times the beam current. Therefore, the higher the voltage, the more heat has to be removed by some cooling mechanism, giving limits on the maximum *cathode voltage* $\times$ *beam current*.

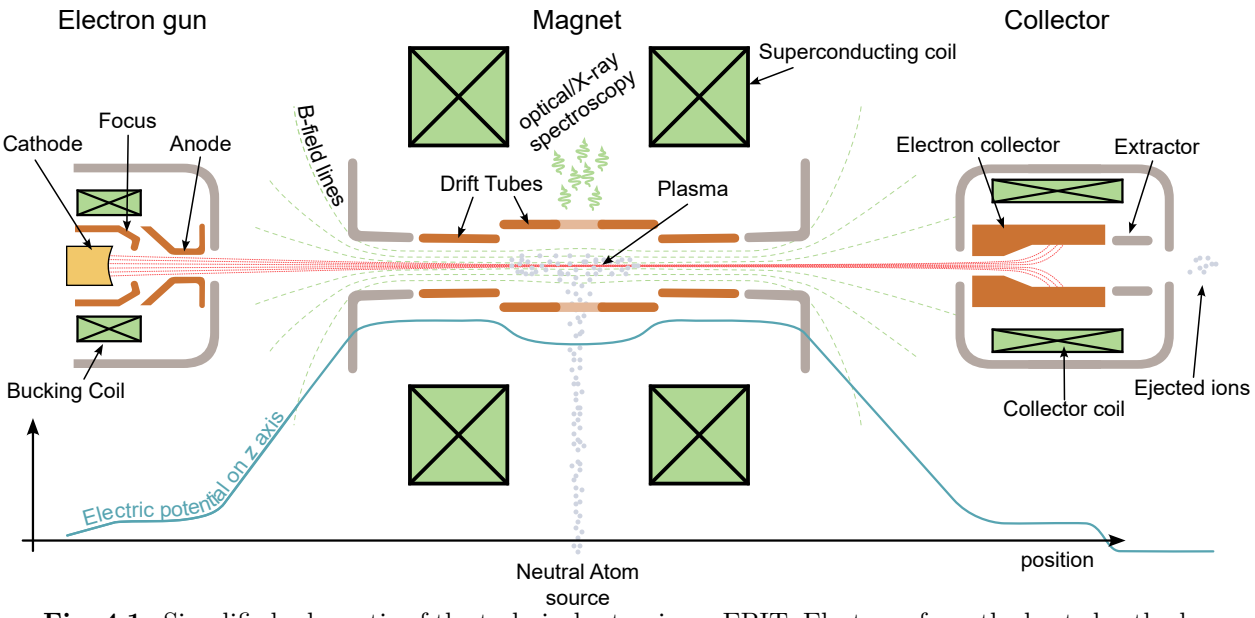

Fig. 4.1: Simplified schematic of the technical setup in an EBIT. Electrons from the heated cathode are accelerated towards the superconducting magnet where they follow the magnetic field lines, resulting in a compressed high density electron beam. This collides with the neutral atoms from a nearby source, ionizing them in the process, producing higher and higher charge states. The electrons then leave the magnetic field entering the collector where they hit the surface, closing the circuit of the electron gun. The collector is open to both directions, enabling to extract ions from the drift tubes. Electrons are hindered to leave through the backside of the collector by setting the extractor voltage higher than the cathode voltage.

in the collector. To be specific, both the collector and the electron gun are biased to the same voltage, such that the kinetic impact of the electrons on the collector is solely given by the voltage applied to the cathode[2].

Perpendicular to the beam around the central drift tube it is possible to inject neutral atoms from various sources. The central drift tube is therefore typically slotted for access to the trap. Additionally these slots enable the observation of the radiation produced by the ion-electron and the ion-ion interaction in the trap which can be used for spectroscopy. In the past, different spectrometers have been used for probing electron transitions of highly charged ions within EBITs [105, 106]. In this thesis, the focus will be on germanium detectors which were used to detect X-rays emitted from electron recombination events to test the production of certain charge states, as well as giving an estimate of their abundance in the trap.

4.1.1 Electron Beam

As the name suggests, the electron beam in the EBIT is an integral part of such devices. With the high current density due to the high compression by the magnetic field it results in a strong interaction between the plasma and the electron beam. The compression results from the conservation of the angular momentum, which means that for the increasing magnetic field, the cyclotron frequency increases which causes the rotation radius to decrease. Thus, the radius is compressed in the strong field until the interaction between the electrons due to coulomb repulsion and the thermal interaction is equal to the Lorentz force. With the assumption non-thermal particles starting in zero magnetic field, the limit of the radius is given by the space charge and is then called

[2]Neglecting inter-beam scattering and thermal electron energy.

Parameter	Value
Cathode voltage	some kV
Beam current	5 mA to 250 mA
Beam radius	around 30 µm
Current density	$<100\,\mathrm{A/mm^2}$
Magnetic field	0.5 T to 8 T
Cathode Temperature	1100 °C
Thermal energy $k_\mathrm{B}T$ at cathode	0.1 eV

Tab. 4.1: Typical EBIT parameters frequently present in the devices used throughout this work.

Brillouin radius, which is defined by:

$$r_\mathrm{B} = \sqrt{\frac{m_\mathrm{e} I_\mathrm{e}}{\pi \epsilon_0 \dot{z} e B^2}}. \tag{4.1}$$

I_e is the electron current, B is the magnetic field, and $\dot{z}$ the velocity of the electron along the magnetic field. As the particles exit the cathode with significant thermal energy, their initial velocity has to be taken into account. Herrmann theory [107] extends the theoretical approach by this. An analytical equation to the beam radius is given by:

$$r_\mathrm{H} = r_\mathrm{B} \sqrt{\frac{1}{2} + \sqrt{\frac{1}{4} + \frac{8 m k_\mathrm{B} T r_\mathrm{c}^2}{e^2 B^2 r_\mathrm{B}^4} + \frac{B_\mathrm{c}^2 r_\mathrm{c}^4}{B^2 r_\mathrm{B}^4}}}. \tag{4.2}$$

Here, e and m are the electrons charge and mass, respectively. r_c is the cathode radius and B_c is the magnetic field at the cathode. Note that the Herrmann radius r gives the radius in which 80 % of the electrons travel. From the equation, one can follow that if the field is minimized at the cathode ($B_\mathrm{c} = 0$), the radius will be governed by the thermal distribution of the particle. This is then typically in the range of a couple 10 µm.

To achieve this requirement of small B_c, there are typically two approaches: One is to design the main magnetic field of the EBIT in a way to have a zero field region at the place of the cathode. A mechanical manipulator is then used to move the cathode into the minimum. The other option is to implement a coil close to the cathode used to compensate the stray field of the main magnetic field. This is typically used in EBITs with strong magnetic fields. For this annealed iron is typically used to further screen the cathode to reduce the fringe field of the magnet.

After the beam traveled through the trap it leaves the strong magnetic field, and enters the collector which includes an inversion of the magnetic field polarity. There, the radius of the electron beam increases such that the electrons hit the collector with some residual kinetic energy. The field geometry is achieved similar to the one at the cathode, either by design of the main magnetic field, or by a solenoid, called here typically collector coil.

The thermal electrons in the cathode will tunnel out with increased likelihood based on the applied electric field on the surface of the cathode. The electron current that is flowing through the setup will then be given by the Child-Langmuir law, stating that the outflow of electrons will produce a space charge in front of the cathode, which counteracts the electric field, reducing the tunneling likelihood. Therefore, the current out of the cathode will reach the equilibrium where the space charge in front of the cathode compensates the electric field. Table 4.1 shows typical parameters for an EBIT. Note that this table is not generally applicable for any EBIT In example, the current in the Alphatrap Mini-EBIT, introduced later in this thesis, is only around a few single mA, therefore producing a much smaller current density in the central trap.

4.1.2 Ion Trap

The prior section shows how the electron beam behaves in the device. What makes this then a *true* electron beam ion trap is the fact that the beam takes integral part in the confinement of the ions within the trap. The space charge produces an additional radial force, pulling the positively charged ions into the trap. This added potential can be parameterized as in example discussed in [45]:

$$V_{\mathrm{r}} = \frac{1}{4\pi\epsilon_0}\frac{I_{\mathrm{e}}}{\dot{z}}(1-f). \tag{4.3}$$

Here, I_{e} and $\dot{z}$ are defined as above, f is the ratio between the present charge carriers coming from positive (HCI) and negative charges (electrons). For a trap with no HCI, f would therefore be 0 and the radial potential V_{r} is maximal. This takes into account that the HCI in the trap produce a field opposing the Coulomb force from the electron beam, pushing the ions outwards.

Within the trap, apart from simple Coulomb interaction, many other effects govern the overall behavior of the ions. A level scheme and a sketch of the most dominant processes is shown in Fig. 4.2. Due to the high electron density, there is a high chance of electron impact ionization. High energy electrons colliding with electrons bound to the nuclei can ionize it, bringing the particle into a higher charge state:

$$X^q + e^- \rightarrow X^{q+1} + 2\,e^-. \tag{4.4}$$

X^q is here an ion in charge state q, being ionized by the electron. To achieve this, the kinetic energy of the electron from the beam must be larger than the binding energy of the bound electron. Another regularly occurring interaction is charge exchange between ions:

$$X^q + Y^z \rightarrow X^{q-1} + Y^{z+1}(+\gamma). \tag{4.5}$$

Here, ion X and Y come in close proximity and an electron transfers from one ion to the other, losing energy in form of heat or radiation (γ). This effect is not desired, as it results in high charge states having a finite lifetime in the trap, counteracting the process of producing high charge states. Furthermore electron capture of an electron from the electron beam happens frequently:

$$X^q + e^- \rightarrow X^{q-1} + \gamma. \tag{4.6}$$

An electron with kinetic energy is captured by the ion, decreasing its charge state. This process is also known as radiative recombination, and will result in the emittance of a photon with a kinetic energy equal to the sum of the kinetic energy of the initial free electron and the binding energy of the specific eigenstate, the electron ends in. Detecting the produced photon and measuring their energy is therefore not only used to monitor the processes in the trap, but also enables to study the energy levels in the ion. On the right side of this figure, the related process of di-electric recombination is shown. Different to radiative recombination this is a resonant process. This is typically a two step process, where the energy available from the electron capture resonantly excites an electron from the inner shell into an upper level:

$$X_{\mathrm{i}}^q + e^- \rightarrow X_{\mathrm{j}}^{q-1} \rightarrow X_{\mathrm{k}}^{q-1} + \gamma. \tag{4.7}$$

Thus in the second step, there is a vacancy in a lower shell, making these configurations very short lived. They decay quickly, emitting a photon γ in the process. Studying these X-rays therefore enables to study the atomic levels even without accurate information of the electron beam energy.

Another source of radiation produced in the EBIT comes from electrons decaying from a high

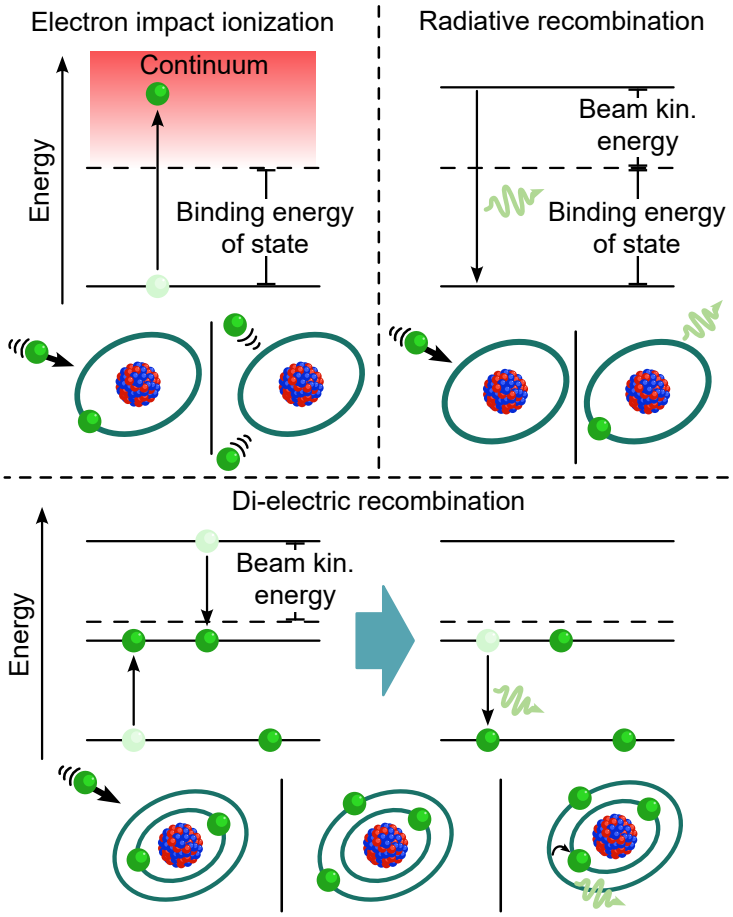

Fig. 4.2: Level diagrams of electron impact ionization (top-left), Radiative recombination (top-right) and di-electric recombination processes (bottom).

energy level into a lower one:

$$X_{\mathrm{i}}^{q} \rightarrow X_{\mathrm{j}}^{q} + \gamma. \tag{4.8}$$

X_{i}^{q} and X_{j}^{q} represent here an ion with an (arbitrary) charge state q, in two different electron configurations. An example for such event is K-alpha radiation, where an electron in the L-shell falls into a vacancy in the K-shell emitting a photon with the corresponding binding energy difference. In the plasma due to the ongoing ion-ion and ion-electron interactions, excited states are produced constantly, producing radiation that can be used to study atomic energy levels. In the past, this was used to measure Lamb shifts of different atoms in heavy ions and deep shells, where the electron-nucleus interaction is far stronger than in hydrogen. Famous for this is Peter Beiersdorfer, who measured the Lamb shift in lithium-like uranium. Specifically he measured the transition energy between the $2s_{1/2} - 2p_{1/2}$ level [31]. The measured value of 280.645(15) eV test QED theory in the strongest fields available for lithium-like ions, making this one of the most important tests of QED.

Chapter 5

The Alphatrap Experiment

The Alphatrap experiment was built up as a successor of the Mainz g-factor experiment [52]. At Mainz, the limit up to which highly charged ions (HCI) could be produced in-trap has been reached. g-factor measurements in this trap were therefore only performed with ions up to hydrogen-like silicon and lithium-like calcium. Therefore, to go into a new regime of much higher Z, a separate source was required. At the Max-Planck-Institut für Kernphysik the EBIT facility is located, where the EBITs can produce these charge states in much higher Z. Thus, Alphatrap was set up there, and the goal is to extend the g-factor measurements into the regime of high-Z systems.

This chapter covers the experiment as a whole, starting with the description of the different sources that are used for the production of various charged particles. Next, the beamline for ion transport into the experimental setup will be described. This is followed by a more detailed look at the Alphatrap magnet and the components necessary to perform Penning-trap spectroscopy using various trap sections. An overview paper with lots of in-depth details about Alphatrap can be found in [52]. Further details can be found in Ref. [108].

5.1 Ion Sources

For production of HCI, three different sources are connected to the Alphatrap-setup: Two are electron beam ion traps (EBIT) where HCI are produced via charge breeding in a high energy electron beam as described in Chapter 4. The third is a laser ion source (LIS), which uses a pulsed laser with a pulse length of 8 ns and around 2 mJ of beam energy to vaporize and ionize beryllium from a target. In the future, co-trapped $^{9}Be^{+}$ is intended for sympathetic cooling of an ion in the trap. This is most useful for high-precision measurements in light ions or with laser-spectroscopy, as the thermal distribution of the particles can be a limiting systematic. Since the LIS was not used during the scope of the thesis, the reader is referred to Ref. [109] for details.

5.1.1 Mini-EBIT

At Alphatrap, the prototype model [110] of the successful miniature EBITs [111] is connected as an ion source. Using permanent magnets, a magnetic field of around 0.7 T is generated in the center of the trap. In this setup, the electron beam from a $\varnothing$3.4 mm cathode can reach currents up to 10 mA. The maximum beam energy is limited to 5 keV, which under ideal conditions enables production of hydrogenlike ions up to $Z = 18$. Therefore the EBIT is used for production of medium-charged ions.

Previously it has been used for ions such as $^{12}C^{5+}$, $^{40}Ar^{13+}$, $^{84}Kr^{23+}$, $^{20,22}Ne^{9+}$ [95, 112–

114]. As no cryogenic components are present, the EBIT is operational on rather short notice, enabling quick reloading in case of ion loss due to electron capture or other catastrophic events[1]. With a gas inlet, various gaseous elements or organic compounds with high vapor pressures can be injected into the EBIT for charge breeding. During this thesis, the Mini-EBIT has been used for the production of hydrogenlike carbon, which was used as a mass-reference for a cyclotron-frequency-ratio measurement to determine the atomic mass of the tin-118 isotope, as described in Chapter 8.

5.1.2 Heidelberg EBIT

The Heidelberg-EBIT (HD-EBIT) is currently the EBIT with the highest electron beam energy at the institute. It incorporates an electron gun which can be biased in respect to the drift tubes by about 65 kV, enabling to ionize charge states with binding energies up to 40 keV. The superconducting magnet produces fields up to 8 T and is cooled by liquid helium in a tank which directly incorporates the magnet coils. A significant advantage of the liquid helium tank is the separation of the magnet from the high voltages present in the EBIT setup. Possible sparks are thus shielded very effectively, and damage to the magnet winding is very unlikely.

As the EBIT has not been modified during the scope of the thesis and was only used as to produce highly charged ions, no detailed overview will be given, but rather sources for more detailed information are given were necessary. A good starting point for a more complete overview of the EBIT can be found in [53, 115].

As any EBIT, it consists of three core sections, the electron gun (E-gun), the drift tubes and the collector. The central drift tube has several side-ports used for spectroscopy and injection of neutral atoms and molecules. For X-ray detection, the EBIT includes a beryllium window on the side. Attached to this is an X-ray detector, incorporating a large germanium crystal to detect X-rays from within the trapping region. This enables to detect the successful production of specific charge states, by observing characteristic X-ray lines, as explained in Chapter 4. The bottom port is used to feed the charge-breeding process in the EBIT with a constant flow of neutral atoms or molecules. Through a series of openings used to reduce the size of the neutral beam in order to avoid an unwanted high gas load which ensures a good vacuum in the inner trapping region. Gases can be loaded via a needle valve used to adjust the amount injected into the trap. Other options include organic sources with an inherently small vapor pressure, or oven sources where the vapor pressure is increased by heating a source material in a crucible. This is useful for metallic sources, as their vapor pressure at temperatures exceeding 1000 °C becomes rather high. For the production of hydrogen-like tin, both an organic source and an oven have been successfully used for injection, as described in Chapter 6.

5.1.3 Beamline

The HCI produced in the described sources then have to be transferred into the measurement apparatus. This is done through a high-vacuum room-temperature beamline. With an acceleration voltage between 1 kV and 8 kV, the ions move quickly through the vacuum. Various ion optics are used to steer and focus the ion bunch. Further details on the ion optical components of the beamline are given in the ALPHATRAP review paper [52]. Further information on the connection towards the HD-EBIT can be found in the PhD Thesis of Tim Sailer [95]. To monitor the transport, the beamline incorporates multiple multi-channel plates which can be moved into the beam with mechanical feedthroughs. After ejection the ions are separated by charge state with a Wien filter

[1] From personal experience this is typically accidental improper handling or an exploding TMP.

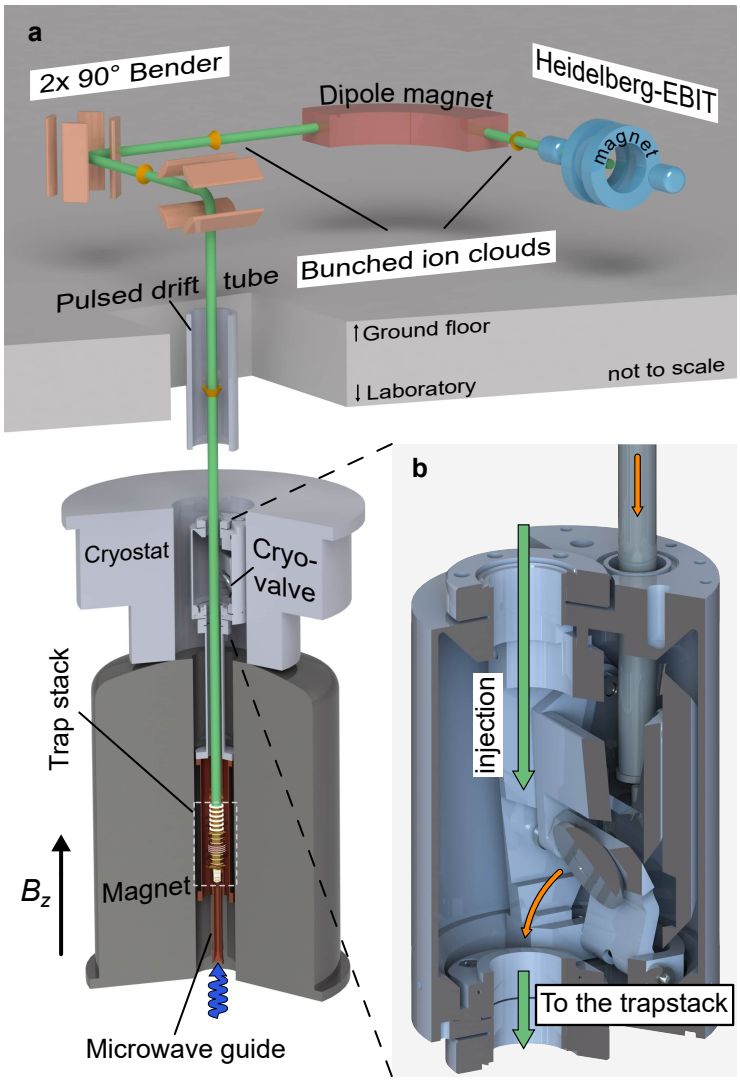

Fig. 5.1: Sketch of the experimental setup connecting the HD-EBIT to the ALPHATRAP apparatus (**A**). **B** shows the cryogenic valve which blocks the inflow of gas from the room-temperature beamline into the cryogenic trap setup. It is manually actuated and reduces the flow of gas by about two orders of magnitude [116, 117] Adapted from Ref. [54].

(mini-EBIT) or a dipole magnet (HD-EBIT). A sketch of the mini-EBIT beamline can be found in Ref. [52]. A simplified sketch of the HD-EBIT beamline has been published in Ref. [54], shown in Figure 5.1.

5.2 The ALPHATRAP-Measurement Apparatus

5.2.1 The Magnet

A superconducting magnet made by Oxford Industries is used for the experiment. The persistent superconducting coil is cooled below its critical temperature using liquid nitrogen and helium. It is charged to a field of about 4 T, which sets a lot of properties which are essential for Penning-trap spectroscopy. In example, as q/m of most ions of interest is between 0.3 e/u and 0.5 e/u, the cyclotron frequency is somewhere between 20 MHz and 30 MHz. Similar, the Larmor frequency for HCI with an s-shell valence electron is on the order of 100 GHz to 110 GHz. For boron-like systems, the g factor is typically around 0.66, and hence their transition frequencies are at roughly 36 GHz. The magnet has a so-called *warm bore*. The high-field section in the middle is separate from the magnet vacuum and therefore at room temperature. The alternative to these are the cold-bored type. A sketch of the magnet and its connection to the beamline is shown in Figure 5.1.

5.2.2 Cryogenics

The superconducting magnet is cooled by a two-stage cryostat, one for liquid helium, and an intermediate one with liquid nitrogen to reduce the thermal load on the 4 K section. The measurement apparatus with the trap and the trap electronics is similarly cooled to cryogenic temperatures. The inner part is cooled by liquid helium to about 4 K, and the dewar has a volume of 14.5 L. This is surrounded by a nitrogen shield, connected at the top to a 55 L liquid nitrogen dewar. This shields the 4 K section from the thermal radiation coming from the room-temperature vacuum chamber. The holding time is a few days. Therefore biweekly refill is needed. As for any high-precision measurements, the stability of the environment influences the achievable precision. Thus, the temperature of the trap section must be kept stable for the best results. To achieve that, the pressure within the cryostats is stabilized with a mass-flow controller that stabilizes the gas flow which is PID regulated to a specific pressure. The setpoint for the pressure is set to 1025 mbar, well above the ambient pressure typically present in the magnet room. The connection between temperature and pressure is directly related to the change of the helium boiling point for different pressures. Hence, if the pressure changes, the boil-off rate changes till a (new) temperature equilibrium is reached. With the setup present at the start of the thesis, the typical pressure jitter was on the order of a few µbar. As later described, during the scope of the thesis, using a very precise barometer, this pressure jitter was reduced to below a µbar. Note that this was done after the measurements performed with the different tin charge states.

Cryovalve

One important and rather unique component at ALPHATRAP is the cryogenic valve. Manual actuation makes it possible to open and close the connection between the cold XHV[2] trap chamber and the UHV[3] in the beam line. Typically the valve is closed, and only when loading ions it is opened briefly to avoid too much gas flowing into the chamber[4]. The valve is connected to a mechanical feedthrough, coupled through a rod which is retractable to minimize heat-load. This locks into a gear box, that translates the rotational motion which drives a metal block that *seals* the trap chamber entrance. The valve is located in the middle of the liquid helium cryostat, and is shown in Figure 5.1**B**. In cryogenic tests, this showed a reduced flow by about two orders of magnitude compared to when fully opened [116]. This effectively blocks the constant inflow of gas from the warm sections above, while still enabling slow[5] ions to be injected from the various sources when needed. As later described in Section 7.2, this keeps the pressure in the trap below 10^{-16} mbar, resulting in week long lifetimes even for extremely high charge states. Recently, this valve was upgraded to incorporate a window for optical access even when the valve is closed. This has been developed by Valentin Hahn within his bachelor thesis [117].

Above and below the valve, steel tubes attach it to the room-temperature beamline above, as well as the trap chamber below. The tubes incorporate an edge-welded bellow to reduce the thermal load and relief stress from the thermal contraction when the setup is cold. With this in the center, four vertical copper bars connect the trap chamber inside the magnet to the liquid helium reservoir.

[2] Extremely-high vacuum. In principal this is the correct term, but considering that our trap operates at pressures five orders of magnitude lower than the (upper) XHV limit, this category seems a bit inaccurate.

[3] Ultra-high vacuum. Typically in the low 10^{-11} range.

[4] Most critical is helium and H_2, as they are not as effectively pumped by the cryogenic walls in the 4 K environment

[5] Slow in the the sense that they are not fast enough to be injected through a degrader foil. At ALPHATRAP the speed is typically smaller than given by an acceleration potential of 10 kV.

5.2.3 Trap Chamber

Attached to the four pillars are the cryogenic electronics necessary to operate the experiment. This includes all the necessary filters which are supposed to block/reduce any noise that could be introduced into the setup from the outside. Additionally, the superconducting resonators, as well as the amplifier for ion detection are located here. Furthermore, the pillars connect the liquid helium bath to the trap chamber. This encloses the $< 10^{-16}$ mbar trap vacuum from the cryostat insulation vacuum. The cylindrical housing and the closing flanges at the top and bottom are made from OFE[6] copper. Centered on the top flange is the ion tube towards the cryovalve. It furthermore incorporates 36 electrical feedthroughs used for electrode biasing, as well as excitation and detection. On the bottom, a viewport in the center enables microwave irradiation to enter the trap, it is also designed to give optical access for laser spectroscopy as already shown by Alexander Egl in his PhD thesis and the resulting publications [112, 118].

Around the trap chamber, a self-shielding coil (SSC) is located [52, 108]. This is a persistent coil with a specific length-to-diameter ratio that is used to counteract external magnetic field changes for a better magnetic field stability in the trap. This is often used to achieve shielding factors of several hundred, meaning that an external homogeneous external field change coaxial with the coil is suppressed in the center by said factor [119]. After the tin campaign, the chamber was replaced, and instead of the SSC, two separate persistent coils that can be charged were implemented. Their geometry enables to change the magnetic field homogeneity B_1 and B_2 by varying the current running through them. Since the magnetic field stability is essential, instead of the removed SSC, a large superconducting shield (SCS) was put around the chamber. Similar to the SSC, a changing external magnetic field induces currents in the superconducting cylinder which counteracts the change within the cylinder, and hence suppresses field changes from external sources. This is a much simpler approach than the SSC, as here the geometry is far less critical. For the SSC, the length must be matched to the diameter, and hence any deviation from this results in a mismatch of the compensation. The insertion, and first results with the SCS are discussed later on in the Outlook chapter (Sec. 10.3).

5.3 Trap Stack

Located within the trap chamber is the trap stack, also called trap tower. Within these stacked cylindrical electrodes the measurement takes place. All electrodes are separated either with sapphire, or SiO_2 spacers. In total, the trap can be separated into three sections, in which ions can be stored, and in which the measurements take place. In Fig. 5.2 the trap stack is shown together with the essential electronic connections.

5.3.1 Capture Trap

The upper most trap consists of six identical 9 mm radius electrodes. These are used for two purposes, ion capture, as well as ion storage. Up to 600 V can be applied to these, enabling to slow down and capture the incoming bunch of ions. Details on the capturing procedure can be found in the ALPHATRAP-review paper [52]. Ideally after capture, a cloud of ions is kept in the capture trap, and whenever needed, a single ion is separated. Typical stored cloud sizes range anywhere from single ions to about 100. Combined with the high vacuum, week long measurement campaigns including detailed systematic studies are possible.

[6] Grade C10100 copper with a purity higher than 99.99 %.

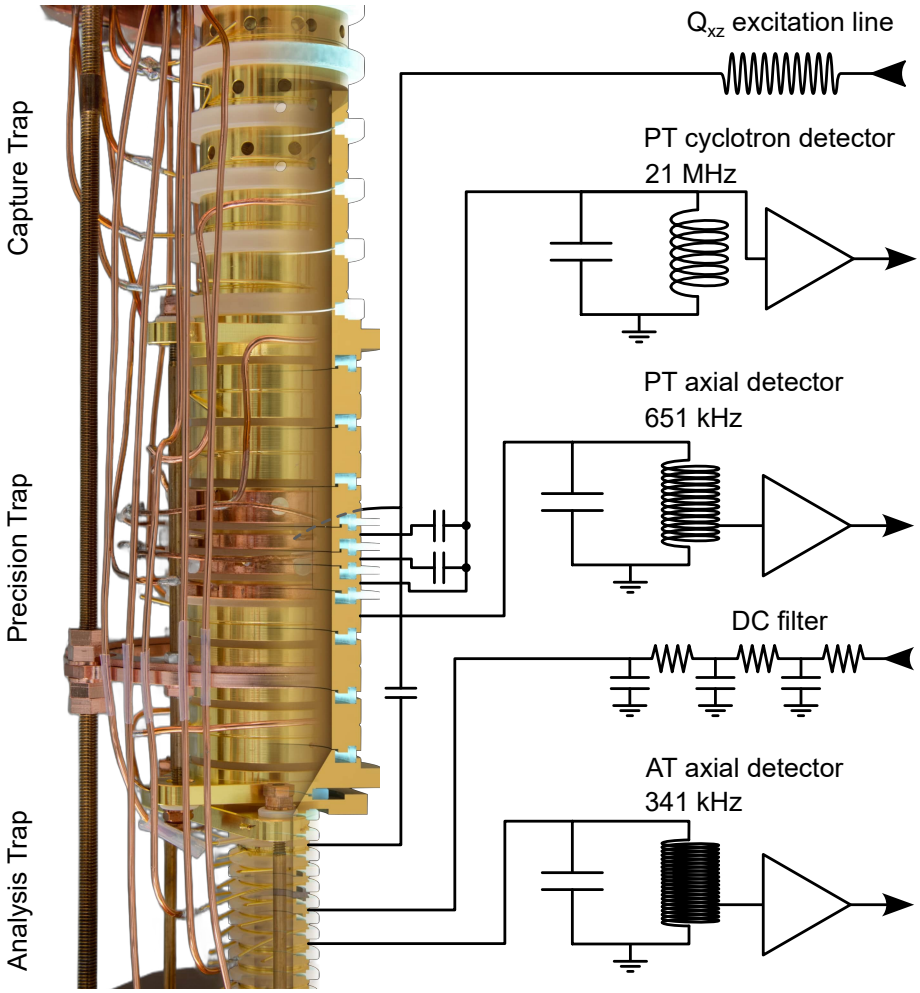

Fig. 5.2: Selection of the electrical connections to and from the trap stack. The Q_{xz} excitation line is connected to a split electrode in both the PT and the AT, separated by a 220 pF capacitance. Simplified versions of the resonator circuitry are also shown. The PT cyclotron detector is connected to the ring electrode as well as the two inner correction electrodes for a better effective electrode distance. The DC filters – connected to every electrode but here only shown for an AT electrode – are made with 50 kΩ resistors and 22 nF capacitors. The picture on the left is the assembled trap (Photo kindly provided by Ralf Lackner).

5.3.2 Precision Trap

Once an ion is singled out, it can be moved to other sections of the trap by adiabatic transport. Below the capture section is the Precision Trap (PT). It also has a diameter of 9 mm, which is chosen for a small image-charge shift (see Sec. 3.2.2). The design of the trap is described in the thesis of Florian Köhler [86], it is a 7-pole trap. This axial symmetry design incorporates a ring electrode, together with four correction electrodes and two grounded outer electrodes called endcaps. The voltage ratio between the two pairs of correction electrodes and the ring electrode is called tuning ratio ($TR_{1/2}$), as it is used to optimize the harmonicity of the trap. Therefore systematic studies include a tuning and a characterization of the residual anharmonicity coefficients. The second trap defining characteristic is the magnetic field. Here it must be as homogeneous as possible. B_1 (see Eq. (3.12)) in this trap is 2.64(3) mTm^{-1} [52]. The second-order field inhomogeneity coefficient B_2 is about 60 mTm^{-2} in the trap, which is already quite homogeneous, and produces only small shifts for the tin ions. This is achieved by the implementation of a compensation ring, which cancels the stray field of the magnetic bottle at the lower part of the trap where the spin-state detection

takes place (see Sec. 3.4) [52]. B_2 is furthermore minimized by moving the particle axially from the center, which results in a residual B_2 of less than $10\,\mathrm{mTm}^{-2}$. For this, the position is controlled by the electric potential applied to the electrodes as explained in Ref.[95]. This is possible, as slightly off-center ($\approx$1 mm) a position with $B_2 = 0$ exists. Since the particle is no longer in the geometric center of the axially symmetric trap electrodes, the trapping potential is prone to be asymmetric at the shifted position, which could potentially induce additional shifts from odd-order C_n coefficients as discussed Chapter 3. These have been studied for this specific trap in the thesis of Tim Sailer [95], with the result that the measurement uncertainty for C_3 is basically identical to the one in the symmetric trap due to patch potentials, manufacturing tolerances and absolute accuracy of the high-precision voltage sources.

5.3.3 Analysis Trap

As described in Sec. 3.5, for spin-state detection a second trap with a large magnetic field inhomogeneity is needed. This is often called Analysis Trap (AT), and at Alphatrap it is located below the PT, separated by some transport electrodes. With 3 mm radius it is significantly smaller than the PT. The size is chosen such that the lower cut-off frequency for the microwaves traversing the trap is above 30 GHz, which is required for boron-like g factors. The inner ring electrode of the AT is made from a piece of cobalt-iron, which magnetization is saturated in the 4-Tesla field. This perturbs the magnetic field, producing a drop in magnetic field in its center. In this minimum, often referred to as a magnetic bottle, the second-order gradient B_2 is large. At Alphatrap it has a value of about $42.77\,\mathrm{kTm}^{-2}$. Below the AT are a few electrodes which can be used for ion storage. These are followed by a circular microwave guide that enables the injection of microwaves from the outside.

Chapter 6

Experimental Results: Ion Production

This chapter is presenting the steps taken to produce hydrogen-like tin in the Heidelberg-EBIT (HD-EBIT), which is followed by the subsequent injection into the ALPHATRAP apparatus. Initially the HD-EBIT was supposed to be able to reach the beam energy required to ionize K-shell electrons in lead and beyond [53]. Over the last few years a few roadblocks were hit, limiting the achievable energy to about 65 keV. While this enables production of any lithium-like ion, K-shell binding energies are often higher for high-Z elements, and hence impossible to produce.

6.1 Hydrogen-like Tin Production

As previously explained, a room-temperature beamline is used to connect the high-precision Penning trap to the external ion sources[1]. To optimize the tin production, the HD-EBIT was operated two times for a few weeks: The first run was used to re-commission the EBIT, and see whether the hydrogen-like tin production is possible. In the second run, the goal was to capture hydrogen-like tin in the ALPHATRAP apparatus in order to measure the bound-electron g factor. In the ALPHATRAP apparatus, occasional collision with background gas has been observed which resulted change of the charge state due to electron capture. Since the cross section of such collision scales roughly linear with the charge of the ion, it would be substantially higher with the highly charged tin ions, and collisions would be more frequent. While the lifetime of the ions, the average time till a charge-exchange happens, was always observed to be on the order of multiple months, it was never fully investigated, and therefore unclear how it would be for highly charged tin. Thus the goal of this capture procedure is to inject as many ions as possible.

6.1.1 Neutral Atom Injection

One thing that is critical for the production is the injection of neutral tin into the EBIT for ionization. For metals there are a number of options, in this case, for the hydrogen-like tin production, an organic compound source, as well as an oven source were tested. Other EBITs sometimes employ even more versatile methods, e.g. laser ablation sources, which might become necessary in the future if the amount of source material becomes too small for the other methods [120].

[1] Please forgive me José for reducing these magnificent scientific tools to being *just a source*.

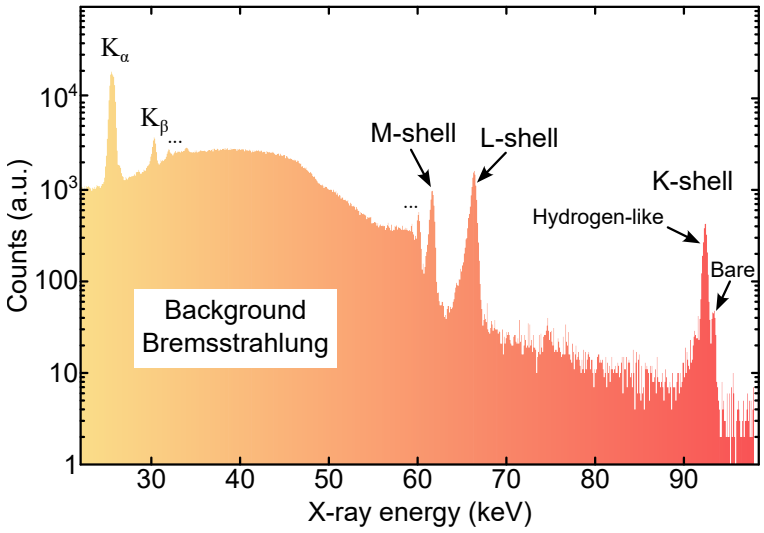

Fig. 6.1: X-ray spectrum taken during the tin production. This shows evidence for the production of hydrogen-like (and even bare) tin. This is shown by the distinct peaks corresponding to K-shell electron captures at roughly 92 keV. These X-rays are produced in events where an electron from the beam is captured directly into a vacant spot within the shell. The emitted X-ray energy is then given by the sum of the electrons kinetic energy and the binding energy of the atomic level.

Organic Compound Source

The organic compound is a simple choice, as with the molecular form, the vapor pressure increases significantly compared to a pure metal form. Often, these can be operated without heating. A subsequent needle valve is used to precisely control the inflow of atoms. In the test run, such an (already existing) source was used to inject tin into the HD-EBIT. With that source the production was tested, and using a germanium detector, the amount of produced hydrogen-like tin ions was estimated. This included first tests of ejection onto an MCP[2] behind the dipole magnet in the transport section after the EBIT. This run proved that production and ejection is possible. One problem though is that the source is not enriched, so the isotopic distribution is that of naturally occurring tin. With 10 stable isotopes, tin has the most of any element. Additionally, no isotope has above 35 % abundance, reducing the amount of desired HCI with the wanted configuration and neutron number. Hence, in the second run, a different source was used.

Oven Source

In this oven source, a tiny sample of the metal is put in a crucible and heated by a tungsten resistor to a temperature between 1000 °C and 1300 °C. In this range, the vapor pressure of tin is similar to the pressure in the vacuum chamber [121]. Thus, the sample slowly evaporates, and a neutral atom beam is flowing out of the source. It is located below the magnet, and a small clear path from the oven to the trap enables efficient injection without excessive contamination of the trap region. Thus, with an enriched Sn-118 sample of a few 10 mg, it worked for a rather long time[3]. Here, the heating current, and therefore the vapor pressure, is a simple way to control the flow of atoms into the trap. Due to the slow charge-breeding time in the EBIT, this has to be optimized for the highest yield of hydrogen-like ions.

6.1.2 Charge Breeding

This is due to the many different events that can happen to an ion/atom in the trap. The rate of ionization must be optimized in respect to the rate of recombination and charge exchange. Meaning that bringing more neutral particles into the trap results in also more electrons being distributed in

[2] Multi-channel plate

[3] It was not estimated for how long the sample should work, but after roughly 2 weeks of (near) continuous operation no reduction of flow was observed.

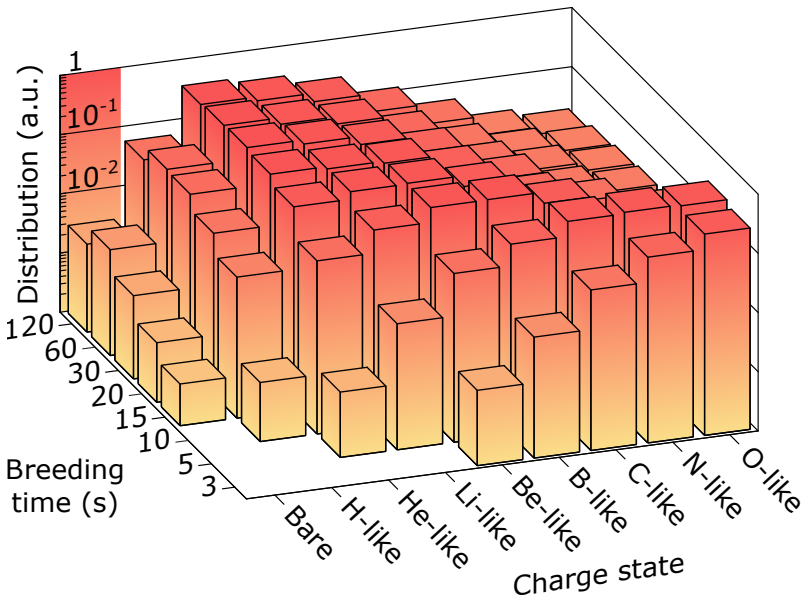

Fig. 6.2: Qualitative measurement of the charge-state distribution after ejection for various charge-breeding times. For the shortest times, no high charge states can be observed, showing that in the charge breeding process high charge states are only produced late. Points without data showed no detectable signal on the Faraday cup.

the plasma, increasing the chance of losing hydrogen-like ions in the process. During the production campaigns, the first indications for the successful production of hydrogen-like tin were seen in the X-ray spectra taken with the germanium-detector connected to the HD-EBIT. Once the injection was set up correctly, and the electron beam energy exceeded the K-shell binding, first electron re-combinations into the K-shell were observed. The rate at which these appear is used to tune the various EBIT parameters, for highest production rates. An energy spectrum recorded over a couple of hours is shown in Fig. 6.1. The EBIT was set to an acceleration potential of -58 kV, which stems from the set voltage difference between the cathode and the central drift tube. At the time, the electron-beam current reached values up to 200 mA. The observed peaks at around 92 keV show the production of hydrogen-like (and bare) tin[4]. From the rate at which photons from these K-shell radiative recombinations occur it is possible to roughly estimate the amount of hydrogen-like/bare ions in the trap [122]: $N_{\mathrm{ions}} = {}^{R}/_{(j\,\epsilon\,\sigma_{\mathrm{RR}}\Omega)}$, R is the rate of detected photons from such a radiative recombination[5]. j is the electron density $j = {}^{I_{\mathrm{e}}}/_{(e\pi r_{\mathrm{H}}^2)}$ based on the current I_{e}, the charge of the electron e and the Herman radius r_{H} as given in Eq. (4.2). $\Omega \approx 1\,\%$ is the solid angle of the X-ray detector, which can be estimated based on its size and distance to the trap center, and $\epsilon \leq 4\,\%$ is the quantum efficiency of the detector. The radiative recombination cross section σ_{RR} can be estimated using analytical formulas, as presented for example in Ref. [123]. During the here presented production of hydrogen-like tin, rates of up to R =4 Hz were observed. From this we can estimate to have at least 10000 hydrogen-like ions in the EBIT.

To gather some more information on the production, at the end of the second run, data on the charge breeding was taken. For this, the amount of ejected atoms was measured for different charge states as a function of the charge breeding time. Charge-state separation was done by a dipole magnetic located in the beamline of the HD-EBIT. A following Faraday cup was used to determine the amount of ions ejected ion bunch. Its signal is proportional to the amount of ions (and their charge state) hitting the cup. By varying the time between the ion ejection, the change of the charge distribution as a function of the charge breeding time can be observed. The recorded data is presented in Fig. 6.2. Note that this measurement is less about a quantitative prediction for

[4]The energy scale of the spectrum was calibrated using an americium-241 source.

[5]This assumes that the spatial distribution of the ion plasma is smaller than the electron beam. Since it cannot be excluded that a substantial amount of the ions is outside of the electron beam during operation, the resulting estimate N_{ions} is rather a lower limit of the amount of ions in the EBIT.

the production rates, but rather serves to show the workings of the EBIT in the run. This is due to the various effects that influence the measurement, as in example the neutral atom flow from the oven source or the current of the electron beam can change the result on time-scales similar to the data acquisition time. Additional, it is hard to give reasonable estimates for certain systematic effects that might shift the results. Here an example would be the non-identical distribution of the different charge-states in the trap. This is due to their different charge, and therefore different force from the trapping potentials. Nonetheless, the data serves its purpose in giving an idea of the required charge breeding time for optimized HCI production.

6.2 Ion Capture

For the final capture, the EBIT was set to similar settings as presented above. With an overall beam energy of 58 keV, and a beam current of 200 mA, highest production rates were observed with the X-ray detector. To then transfer the ions into the ALPHATRAP apparatus, the ions were ejected from the EBIT with a fast pulse on the central drift tube. In the beamline after the EBIT, the ions pass through the following dipole magnet. Here the different charge states are separated by q/M, and by adjusting the current through the dipole magnet, the charge state can be selected. Calibration is done by identifying prominent peaks from residual gases in the trap region, i.e. carbon nitrogen and oxygen, along with the evenly distributed tin charge states. Once the correct current setting of the dipole magnet is identified, the ion path is further optimized based on the signal on the MCPs which are implemented regularly within the beamline.

One critical component is the pulsed drift tube, which is used to slow down the ions before entering the magnetic field. This is set to remove most of the kinetic energy of the ion bunch, typically an energy less than $600\,\mathrm{eV} \times N_q$, with $N_q = q/e$. That way, ions can be stopped in the trap with acceptable voltages on the electrodes (below 1 kV for ALPHATRAP). Once the ions reach the MCP closest to the Penning trap and are centered reasonably, the cryovalve is opened, and the charge-amplifier is used to measure the amount of particles crossing the trap section. This is done by measuring the amount of charged particles colliding with the microwave guide below the trap stack. Using an amplifier similar to the ones used for the ion detection, the signal is amplified, and one can directly optimize the amount of particles traversing the trap stack. For hydrogen-like tin, the optimization is typically done with a lower charge state, as large amounts are already abundant after a few seconds, compared to the hydrogen-like state where the charge-breeding[6] takes more than 30 seconds. For the final capture, the dipole magnet is set to the hydrogen-like charge state. How the capturing works is described well in the theses of Andreas Weigel and Tim Sailer [95, 108], as well as in the ALPHATRAP-review paper [52]. Simply said, the ions are slowed down by an electric potential which is matched to the kinetic energy of the ion bunch. Thus, the velocity of the ions reduces in the electric field. By pulsing the neighboring electrodes to a high voltage, the slowed ions can be trapped with low residual kinetic energy. Due to the longitudinal distribution of the ions, only a fraction of the ions can be captured. This stems from the thermal distribution of the ions in the EBIT, and the acceleration potential that ejects the ions.

For the presented injection of hydrogen-like tin, at most two ions were captured in a single shot. Usually for light HCI from other sources, the amount of trapped ions was larger, often in the hundredth range. A large fraction of this is due to the much smaller fraction of ions. Ultimately in the tin production run, with a few shots, four hydrogen-like ions were stored in the Penning trap.

[6] Till a steady state is reached

Chapter 7

Experimental Results: ALPHATRAP

This chapter gives an overview about some measurements and changes done before or during the tin campaign. As their outcome is (near) indifferent of the subsequent measurement chapters, here they are presented separately.

7.1 Pulse Shaping

PnA, as described in Chapter 3.3.1, consists of an excitation and a coupling pulse. For correct motional phase determination, the phase of these two must be locked throughout multiple measurements. This is taken care of by an arbitrary waveform generator[1] (AWG). The required PnA sequence is uploaded to the AWG beforehand. A pulse generator with multiple outputs triggers the AWG as well as the FFT analyzer and the microwave generator (if needed). Typically, the phases of the pulses are randomized between different sets[2], but are kept identical during a single set. These random starting phases require the sine-wave of the pulse to start at a non-zero voltage. This causes a sudden change in the voltage applied to the excitation line, causing high-frequency components in the Fourier-spectrum. Since these are at rather high frequency, and very short in time, their resonant influence on the ion is negligible. Other non-resonant effects can be large though, causing chirps in the applied voltages. Some of these are related to the cryogenic switch which is used to suppress noise from the outside by using a mixture of resistive and capacitive divider where the resistance can be changed with an SW239, a GaAs switch. The electrical connection of the *switch* is shown in Fig. 7.1. It changes the ratio of the voltage divider, so more signal is let through if the switch is set to high impedance. In the *off* state the impedance of the SW239 drops, and the signal is attenuated. In the *on*[3] state, the impedance rises to a few MΩ,

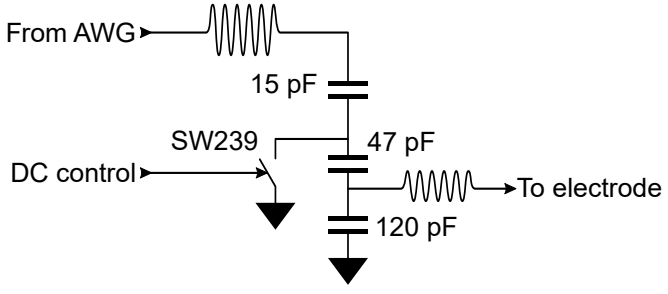

Fig. 7.1: Electrical connection of the cryogenic *switch* using an SW239 with both *inputs* connected to ground, and both controls connected to the *DC gate control*, effectively switching between low resistance (typ 2 Ω) and high impedance (typ. 2 MΩ at 4 K) to ground.

[1] Agilent 33612A, 80 MHz 2-channel arbitrary waveform generator.
[2] A set refers to consecutive phase measurements for a single full measurement of ν_+.
[3] From her on the *on* state refers to an applied control voltage of -3 V, which *closes* the FETs, resulting in a high impedance to ground. The *off* state means shorted control input, resulting in a low impedance to ground,

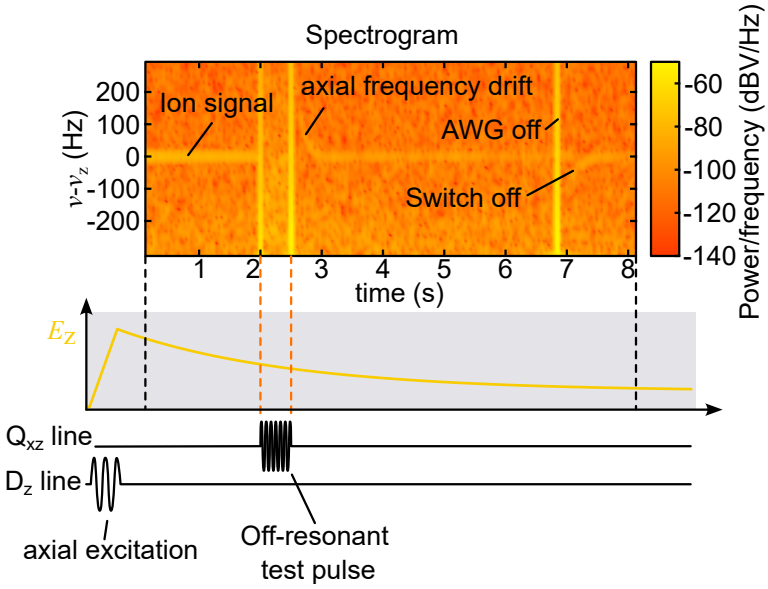

Fig. 7.2: Procedure for testing the switches. After the excitation of the axial mode, the FFT is continuously recorded and after 2 seconds, the off-resonant pulse is applied to the Q_{xz} line. During the pulse and after the pulse, the axial frequency is drifting. The time constant of the drift is determined by the *RC*-filters attached to the electrodes. For the excitation electrodes these have a time constant between 50 ms and 100 ms. Further details can be found in the text.

and the signal is let through nearly unperturbed. This design, albeit simple, is a rather intricate system with some effects onto the measurement that have to be taken into account. One effect is the non-linearity in the *on* state, where the FETs within the SW239 are at a given work-point. Large signals from the AWG therefore cause a partial rectification, producing (on average) a non-zero shift on the output side. Despite the electrode being only capacitively connected, this causes shifts of the particle frequencies on the timescale of the electrode's RC filters (a few 10 ms).

This has been studied qualitatively by measuring the particle frequency after off-resonant pulses. The measurement procedure is the following: The axial frequency is detuned from the detector by a few 100 Hz, to reduce the cooling time of the particle to a few seconds. A dipolar excitation increases the axial amplitude of the ion. Thus, by the off-resonant coupling with the detector, the motional amplitude reduces, and a peak in the FFT signal appears which SNR is roughly given by Eq. (3.21). By continuously acquiring the FFT while the signal is decaying with the dropping amplitude, it is possible to track the motional frequency over short time scales. Here, an 8 s measurement time is chosen, in which the effect of the switch is studied. Shortly after the spectrogram recording starts a radio-frequency pulse is applied with the AWG, non-resonantly to not interact directly with the particle, but only testing the effect of the pulse on the switch and the system. Testing various parameters, i.e. the switch state, the voltage and the pulse-length, enables to test their influence on the axial frequency. A schematic of the procedure is shown in Fig. 7.2. In the example spectrogram multiple things can be observed: Firstly, with the start and the end of the 0.5 s AWG pulse starting at t =2 s the resonator noise increases, resulting in a strong signal over the complete frequency range. Additionally, after the pulse, the particle oscillation frequency is shifted away by around 100 Hz. For these tests, the amplitude is chosen as 6 V_{pp} which is about an order of magnitude stronger than typical excitation pulses as used in PnA. Nonetheless, the observed shift is rather significant and should be still present for typical pulse strengths, although it is hard to estimate this due to the non-linearity of this effect. Importantly, even if there is still a considerable shift with the used AWG amplitudes, this axial frequency drift does not cause a shift of the ν_+ frequency measured with PnA. This is because it will cancel out in the difference between reference phase and the *long* evolution time phase measurement[4]. In the switch *off* case,

suppressing the signal reaching the electrode.

[4]This is only true if the first and the second pulse do not interact, second order effects, as a frequency shift of the axial frequency after the initial modified cyclotron excitation pulse might only shift the final phase in the short evolution times, causing a systematic shift on the resulting frequency. Nonetheless, the amplitude of the dipolar

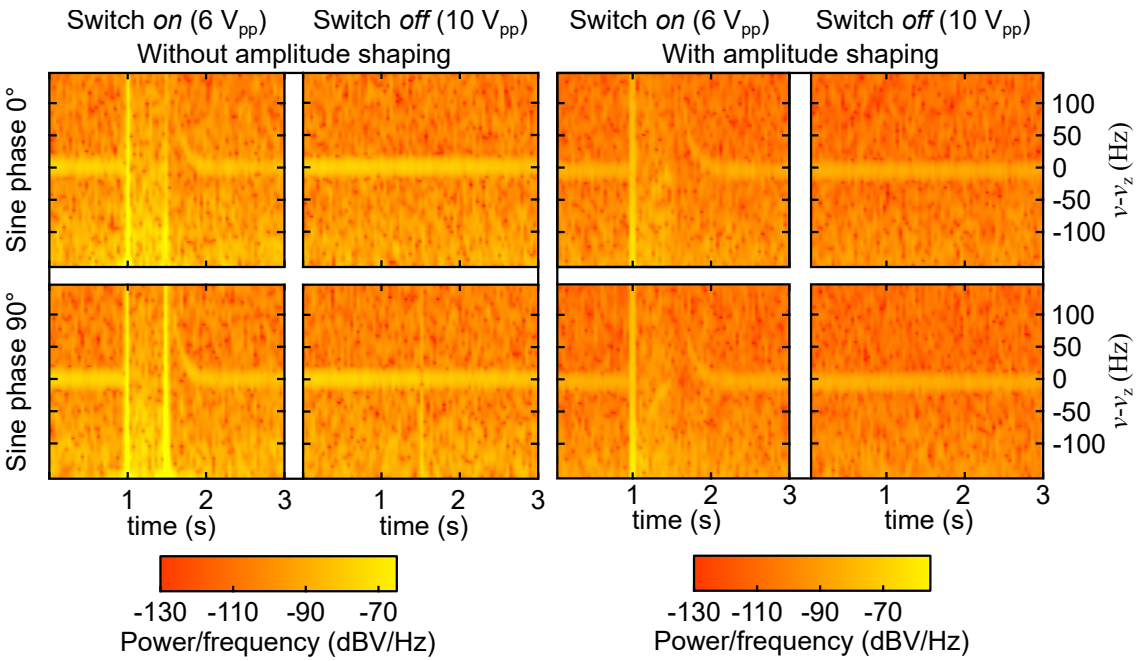

Fig. 7.3: Various parameters and their impact on the particle frequency are shown. The resonator center is roughly 200 Hz lower than the ion axial frequency. The upper four subplots show the non-shaped cases, while the lower show the AM pulse. Comparison between 0° and 90° starting phase show a significant heatup of the whole frequency range for non-zero starting phases in the switch *on* case. With switch *on* the particle frequency also chirps, providing evidence that the non-linearity of the switch causes a change of the electrical potential, causing a shift of the axial frequency. In the switch *off* case, the complete sequence seems to be noise free. So the combination of AM and switch *off* provides the best measurement conditions.

no detectable shift was visible. Thus from then on, PnA measurements were solely performed in that state. In Fig. 7.3, a comparison between various measurement parameters is presented. The ion is visible as the continuous peak. A large change in frequency is observed in the switch *on* case after the rising/falling flank of the pulse, which is due to the non-linearity of the switch. Thus, from that moment on, the switch was kept *off* for the following measurements. Additionally, a pulse shaping routine was implemented into the PnA sequence, that additionally suppresses the high-frequency components in the non-zero starting phase conditions. By ramping the pulse using a $\sin^2$-function as an envelope for the rising and falling flank, the sudden jump that causes high frequency noise is significantly reduced. It is implemented by using the secondary output of the AWG to amplitude modulate (AM) the RF output with the correct envelope including the 1 ms $\sin^2$ falling and rising flank. With this though it is not possible anymore to use two separate channels from a single AWG for two separate electrodes for the two PnA pulses. Thus with AM both pulses must come from the same channel, and also the same electrode. Therefore the Q_{xz}-electrode, to have the quadrupolar component necessary for the axial-radial coupling pulse is used.

Employing this does not excite the resonator as can be seen in the falling flank of the AM pulse. In the rising flank of the switch *on* case, there is still visible excitation of the resonator. It was discovered that this is due to the AWG, which seems to cause some noise when the start of the first pulse coincides with the external trigger. This could be circumvented by adding a short (0.5 s) delay between the trigger and the start of the first pulse. These changes are included in all

pulse is more than an order of magnitude weaker than the coupling pulse, making this effect quite small, and no shift could be seen in the measurement, as it would be clearly visible in the phase measurements with intermediate evolution times.

spectroscopy measurements shown in this thesis, as well as in the last few measurements of the prior measurement campaign of the neon g factors, as presented in the thesis of Tim Sailer [95]. After the measurements it was later on decided to take out the switch completely, to remove all resulting effects from its non-linearity completely.

7.2 Ion Lifetime

Single ion high-precision spectroscopy tends to take significant amount of time. This is simply due to the measured observable and the measurement accuracy. If the particle motion is to be measured, and mHz precision is to be reached, a single measurement needs to be longer than a few ten seconds to reach such accuracy in a single shot. Thus, for a full measurement, i.e. a g-factor measurement, the lifetime[5] must be long to avoid downtime and frequent reloading. This is especially the case when measuring hard-to-produce ions, as the production in itself can take a long time. Room-temperature setups are typically limited due to out-gassing of H_2 and background gases to residual pressures at around 1×10^{-11} mBar. Cryogenic experiments with closed vacuum chambers have shown to provide pressures below 1×10^{-17} mBar at 4 K [124]. The cryogenic environment is advantageous, as any background gas is adhering to the surfaces either by cryocondensation or cryosorption [125]. Cryocondensation is the process of background gases changing from a gasous state directly into the solid state, adhering to the surface. At these temperatures this freezes out any rest gas with the exception of H_2 and He[6]. Cryosorption on the other hand is the domination of weak intermolecular forces when a free particle collides with a surface, effectively decreasing the vapor pressure, resulting in a better vacuum as more H_2 and He can be *cryopumped*. For these, the dominating pumping mechanism is the cryosorption, which saturates the surface once a few mono-layer are built up on the surface. Thus, the amount of gas that can be pumped is limited, and once this is reached, the pressure increases, degrading the vacuum in the trap volume. Therefore, the inflow of these gases has to be minimized in order to avoid saturation. This is typically done by hermetically sealing the vacuum chamber before cooling it down, which effectively blocks virtually any inflow of gas from the non-cryogenic regions.

For obvious reasons sealing the chamber makes it more difficult to inject particles from an external source. For very fast particles ($\geq$ 100keV) it is possible to use thin degrader foils that are sometimes even used to slow down the particles for efficient capturing procedures in the trap, as shown in example with antiprotons in the BASE apparatus [126]. Here the HCI produced in the EBIT are ejected with much lower energy and in smaller numbers, making it virtually impossible to efficiently trap ions using this method. Therefore at ALPHATRAP another approach is followed. In order to allow both slow ion injection and reducing the inflow of gas from a room-temperature beamline, a cryogenic valve actuated from the outside is implemented into the setup [52]. After ion injection the valve is closed, blocking the inflow of gas from the room-temperature sections. Here we discuss the effectiveness of the implemented valve by evaluating the measured lifetime of the stored highly charged tin ions.

Since the interaction of a HCI with the background gas typically results in the charge transfer from the neutral atom/molecule (typically H_2/He), the charge state changes after collision. During the tin campaign, electron capture has been observed a few times. Of the initially four stored hydrogenlike ions, two have been stored at the side and were not checked or cooled after initial

[5] The word lifetime is not meant in the same sense as for radionuclides. Here it refers to the finite storage time due to collisions with background gas resulting typically in charge exchange.

[6] This is principally also the case for the hydrogen Isotopologues, and the lightest noble gas Ne. In the following the focus lies on H_2 and He, which are far more naturally abundant, although all described processes apply to the heavier gases as well.

Tab. 7.1: Single electron capture cross sections using theoretical and semi-empirical (Müller Salzborn formular) models, along with the respective pressure for the observed lifetime. The 1-sigma uncertainty given in the brackets results from the uncertainty of the lifetime.

Model	Cross section σ (cm^2)	vacuum (mbar)
Absorbing spheres model	1.5×10^{-13}	$3(2) \times 10^{-17}$
Classical Barrier model	3.1×10^{-14}	$14(7) \times 10^{-17}$
Müller Salzborn [127]	7.7×10^{-14}	$6(3) \times 10^{-17}$

capture for more than three month. One captured an electron and became helium-like, the second ion was not found again. As it had an unknown motional amplitude due to lack of cooling after capture, the worst case is assumed: that the missing particle got lost on the first day. The other two ions were checked regularly. One survived the complete 98-day campaign without a recombination, while the other recombined for the first time after 7 days becoming lithiumlike (47+). Two month later this recombined again, resulting in boronlike tin[7] (45+). Both recombination events were rather fortunate, as the g factor of the lower charge states could be measured as well, without injection from an EBIT. Averaged[8], this gives a lifetime of roughly 44^{+24}_{-14} d.

From this, the vacuum can be estimated by the equation:

$$p = nk_{\mathrm{B}}T = \frac{k_{\mathrm{B}}T}{\sigma \hat{v} \tau}. \tag{7.1}$$

Here, p is the pressure, n the particle density, k_{B} the Boltzmann constant, v the relative speed of the particles, σ the electron-capture cross section, τ the lifetime, and T the temperature. The speed of the background particle is thermally distributed, and the mean velocity is given by $\sqrt{3k_{\mathrm{B}}T/m_{\mathrm{ion}}}$. The cross sections of electron capture have been studied in the past with a broad variety of charge states and velocities [128–132]. Furthermore, theoretical (and empirical) models exist to estimate the cross section. I. e. using the classical barrier model, the cross section can be estimated by

$$\sigma = \pi \left(27.2\,\mathrm{eV} \times \frac{2\sqrt{q}+1}{I_p} a_0 \right)^2 \tag{7.2}$$

with the charge state q, the ionization potential I_p in eV ($\approx 15.4\,\mathrm{eV}$ for H_2), and $a_0 \approx 0.528 \times 10{-}10\,\mathrm{m}$ as the Bohr radius. The absorbing sphere model [128] estimates the cross section via:

$$R^2 \exp\left(-0.718\sqrt{I_p}/qR\right) = 2.864 \times 10^{-4} q(q-1)\hat{v} \tag{7.3}$$

with R in atomic units ($R/a_0 = R_{\mathrm{SI}}$) as the 'absorbing sphere' radius. A comparison of different models and their cross sections with the resulting vacuum are shown in Table 7.1.

To the best of our knowledge, for the thermal energies present in the cryogenic conditions of the ALPHATRAP setup ($\equiv 30\,\mathrm{meV}$) no measurements determining the cross sections exist. The lowest energies tested have been in the single eV range, far above the present energies. Although some of the models include a velocity dependence, these have not been validated for these conditions, therefore it is difficult to give accurate absolute pressure values. Tests with the most similar conditions have been performed with H_2 collisions at a few eV, where the absorbing spheres model

[7] It is remarkable that two of the three observed recombination events were double electron captures. There are some measurements and theoretical work to estimate the likelihood of single and double capture, but none consider factors as in example the strong electromagnetic field storing charged particles in Penning traps, which will likely play a role in the likelihood of either event.

[8] It could be possible that the pressure is not constant over time, as it might be higher for some time after the cryovalve was opened for loading. Nonetheless, to estimate an upper limit for the lifetime, taking the average is justified.

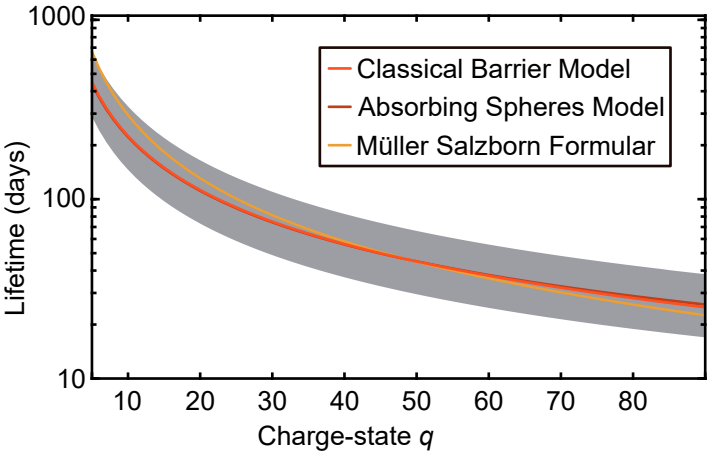

Fig. 7.4: From the measured lifetimes using the tin ions, the scaled lifetime for different charge states is shown. The different models are all rather similar as they all show near linear behavior with q. The gray band is the 1-sigma C.L. from the uncertainty of the measured lifetime.

showed good agreement with the experimental values [128, 132].

A much better estimation can be made for the lifetime of other particles with a different charge state. All cross-section models exhibit a dominantly linear scaling. Thus, for future experiments using even higher charged ions like $^{208}Pb^{81+}$, one can estimate the expected lifetime rather well. In Fig. 7.4 the measured lifetime is scaled according to the models for different charge-states q. For example, in hydrogen-like lead a lifetime of at least 19 days is expected.

To conclude, even though the vacuum is worse compared to a completely sealed chamber [124], it can still be limited to be less than 2.1×10^{-16} mbar using the most conservative estimate for the cross section. Other experimentally better tested models suggest pressures in the low 10^{-17} range. And with the cryogenic valve, the injection is significantly easier and the setup is much more versatile compared to a setup with a degrader foil. This will enable ALPHATRAP to perform many more measurements in this very same setup, especially with the most recent added feature of a window in the cryogenic valve for laser-access [117].

7.3 Phase-Sensitive Spin-Flip Measurement

As one of the key techniques, the spin-state detection in the analysis trap (AT), is of utmost importance for the measurements performed at ALPHATRAP. As discussed in Sec. 3.4, the axial frequency shift $\Delta\nu_z$ in the magnetic bottle is[9]:

$$\Delta\nu_z = \frac{B_2\hbar q}{4\pi^2 m^2 \nu_z}\left(\Gamma_0 \Delta m_s + \hat{n}_+\right). \tag{7.4}$$

Γ_0, the Larmor to cyclotron frequency ratio, is rather large for electron g factors. Thus, a change in the quanta of motion $\Delta\hat{n}_+$ results in a small frequency change, so that they can be basically neglected. For example in hydrogen-like tin, the spin flip is around 300 mHz, while a change due to a cyclotron motion change $\Delta\hat{n}$ is less than 100 µHz. With typical heating rates in (large) Penning traps [100] this is far from being a problem in the state detection of HCI. Therefore, the spin-state detection of electrons bound in HCI mainly depends on stable voltage sources as well as reliable and (ideally) fast frequency readout.

Furthermore, as only the change $\Delta\nu_z$ has to be detected, systematic effects on the frequency can be neglected. As initially proposed in Ref. [133], the frequency can be determined with a phase-sensitive approach. This can significantly shorten the readout times compared to FFT averaging methods. Here, the concept is briefly explained, further details can be found in Refs. [92, 133].

[9] Here the magnetic moment of the magnetron motion is neglected as this is typically negligibly small, especially for electron g factors.

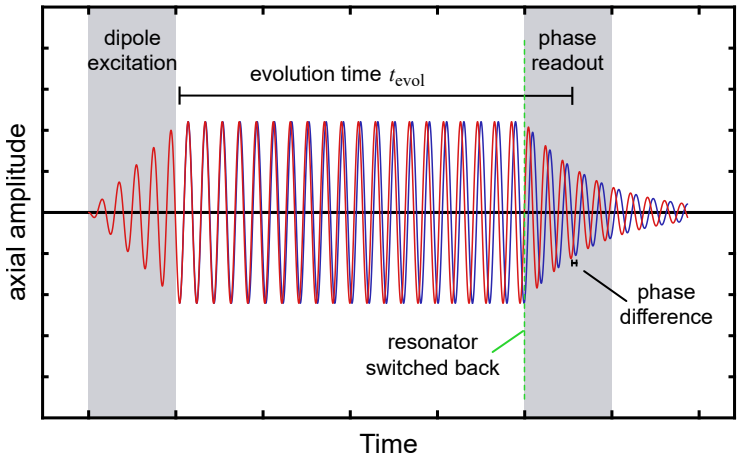

Fig. 7.5: Schematic of the axial phase-sensitive frequency measurement. Beforehand the resonator is detuned by a few kHz. Then the axial radius is increased by a dipole excitation, imprinting a fixed starting phase. After some time, the resonator is switched back, and the phase is read from the peak in the FFT analyzed detector signal. Doing this before and after changing the spin state (red and blue curves) results in a change in the measured phase.

A schematic of the procedure is shown in Fig. 7.5. At first, the axial motion of the particle is excited by a short radio-frequency excitation pulse. After a free evolution time, the accumulated phase of the motion is measured from the peak signal in the detector. To avoid cooling of the motion during the evolution time, the resonator is detuned multiple kHz using a GaAs switch in a circuitry that enables to change the parallel capacitance of the resonator by a few picoFarad. So the sequence is as following: shift resonator – excite axial motion – wait – shift resonator back – measure Fourier signal and extract the phase from the peak. If then the spin-state changes, a subsequent measurement will have a shifted phase of $^{\Delta\phi}/_{2\pi} = t_{\mathrm{evol}}\Delta\nu_z$. For efficient readout, the time t_{evol} is chosen to produce a spin change of roughly $\pi/2 \equiv 90°$. Therefore, depending on the sign of the change, the spin-orientation can be unambiguously determined. In hydrogen-like tin the used time is around 0.9 s. Since the peak signal in the detector, as introduced in the Penning-trap chapter (Chapter 3), is proportional to

$$\mathrm{SNR} \propto \frac{q\sqrt{t}}{\sqrt{T}} z_{\mathrm{rms}}, \tag{7.5}$$

the SNR produced from a highly charged tin ion is very large due to the high charge q. This enables a fast readout, i.e. $t = 256\,\mathrm{ms}$, in addition to a small excitation radius z_{rms} with minor impact on the measured stability from trap anharmonicities. The measured SNR suggests roughly an excitation amplitude of 170 µm, a factor of 10 above the thermal radius of tin in the AT which results in quite small phase-jitter from the thermal starting distribution.

To further improve the stability and therefore the fidelity of the readout, four phases are measured and averaged. Afterwards, the microwave drive is turned on for a few seconds, and four phases are measured again. Figure 7.6 shows exemplary the AT amplitude/phase data of the boron-like tin run. In subfigure **b** the unwrapped phases[10] are shown for the approximately 115° phase shift after a spin change. In the different g-factor measurements, two different evolution times were used, and are compared in Fig. 7.7. Furthermore, with the boron-like ion, some additional longer evolution times were probed for their stability. For short times the frequency stability was limited by readout jitter, as suggested by the reduced frequency jitter at longer t_{evol}. For the longest evolution times the stability sometimes reached 5 mHz of shot-to-shot jitter. This shows the exceptional stability of the setup, and will enable future measurements of even smaller frequency changes. This could be in example a measurement of boron-like lead, its 50 mHz SF will be hard to resolve, but the observed stability suggest that this is possible with an acceptable error rate. It might also improve further in lead, since with a higher q the signal will be larger (see Eq. (7.5)),

[10] Unwrapped and phase normalized, meaning that the phases are adjusted so that the 4 averaged phases before the microwave injection are zero.

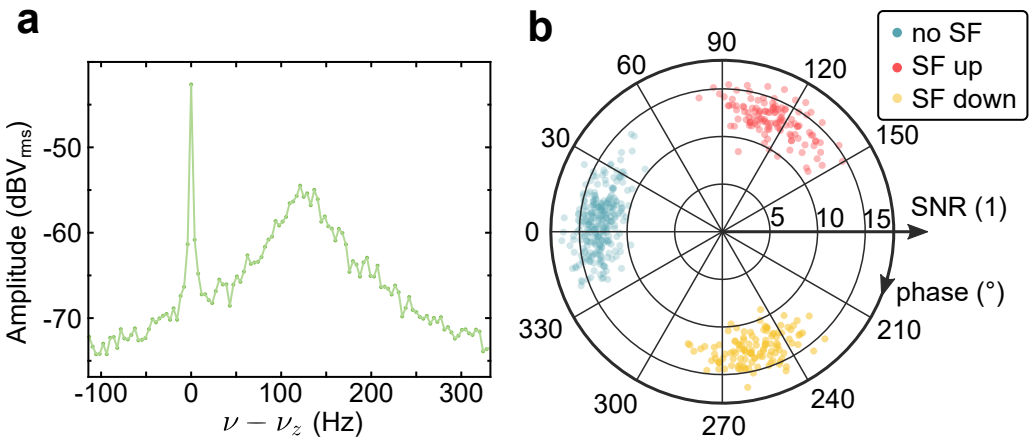

Fig. 7.6: **a** shows the averaged spectra recorded during the boron-like g-factor measurement. The resonator frequency is at roughly 341 kHz. The ion is detuned to a frequency 180 Hz lower than the resonator in order to increase the cooling time. The recording time for each spectra is 256 ms, which results in 3.9 Hz frequency resolution. Subfigure **b** shows the recorded phases, adjusted so that the four initial phases before the microwave injection average to zero. From this, one can clearly see the great resolving power of this method. The 100 mHz spin flip and the 3 s evolution time cause an approximately 115° phase shift of the FFT peak signal. The many points show a clear separation between the three clusters, showing arbitrarily close to 100 % accurate spin-flip determination, further enhanced by averaging multiple phases.

and therefore one could use smaller excitation radii, making the anharmonicity less crucial for the measurement. Other interesting candidates are SF of highly charged ions with a nuclear moment, or even the proton with an approximately 54 mHz frequency change, which would be interesting, as its ratio Γ_0 about a factor of thousand smaller than with bound-electron g factors. Thus, the frequency change from a modified cyclotron quantum jump would be on the same order of magnitude as the SF itself. This would be interesting to get a precise measurement of the heating rate in the trap, which could be compared to that measured in other Penning traps [100].

Along with high precision, the phase measurements are also rather fast. Depending on the needed axial thermalization time and the SF frequency jump, a typical phase-determination can take less then 5 seconds, which was the case for the here presented tin charge states. Overall, the spin-state determination during the measurement campaign was essentially 100 % successful[11].

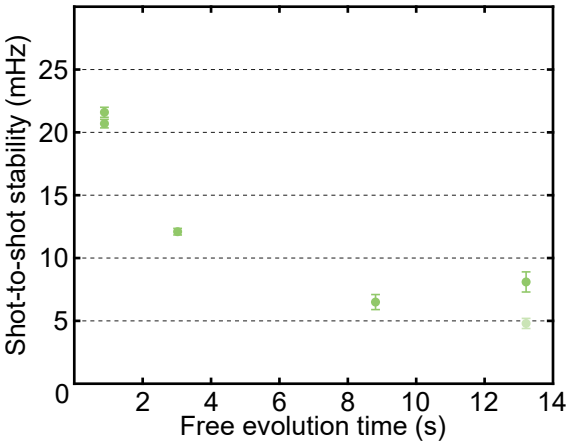

Fig. 7.7: Shot-to-shot frequency stability of the phase-sensitive axial frequency measurement with different evolution times without averaging. The two points at 1 s are extracted from the g-factor measurements of hydrogen-like and lithium-like tin. The 3 s point is from the data of the boron-like g-factor measurement. Points with higher evolution time are dedicated measurements to test the axial frequency stability with long evolution times. The light-green point is a second dataset with 13.4 s evolution time, which showed an exceptional shot-to-shot stability of roughly 5 mHz.

[11] This was only possible after the power supply of the AT endcap electrodes was exchanged for a more stable one. Initially a LoCepps [134] was used, which limited the voltage/frequency stability.

Chapter 8

Experimental Results: The Tin-118 Mass

Since the g-factor determination via Eq. (3.3) depends on external parameters, it is crucial to know these to sufficient accuracy. The electron mass is one of the two external parameters. For nearly 10 years it was extracted from a g-factor measurement of hydrogen-like carbon with 29 ppt accuracy [24]. Only recently a determination using spectroscopy of ro-vibrational levels in HD^+ provided an improved value for the mass of the electron [85]. Thus, the electron mass is known precisely and does not limit any test of the theoretical prediction, especially at high-Z.

This is not necessarily the case for the second external parameter, the mass of the ion. Off all available elements and isotopes, the precision varies quite largly, and can potentially limit the final result for the g factor. In the Atomic Mass Evaluation (AME) 2020 a tin-118 value with an uncertainty of about 4 ppb is given [135]. For the hydrogen-like and the boron-like charge states, this is sufficient, as the theory uncertainty is larger than 0.1 ppm. Only in the case of the lithium-like g factor, the 6 ppb uncertainty of the theoretical value is quite close to the AME uncertainty [64]. Thus, an improved value of the tin-118 mass strengthens the results.

During the tin campaign, the mass of $^{118}Sn^{49+}$ was measured in the ALPHATRAP apparatus. In Penning traps masses are determined by performing a *Cyclotron Frequency Ratio* (CFR) measurement between the ion of interest and some reference ion. For the tin-118 mass, hydrogenlike carbon was selected since the charge-to-mass ratio of $^{12}C^{5+}$ and $^{118}Sn^{49+}$ is identical to 99.7 %, reducing systematic effects, as explained in the following sections[1]. From Eq. (3.1) this means if we measure the free-space cyclotron frequencies of both ions in the same magnetic field B_0 it drops out in the ratio and we are left with the relation

$$R = \frac{\nu_c\left(^{12}C^{5+}\right)}{\nu_c\left(^{118}Sn^{49+}\right)} = \frac{q\left(^{12}C^{5+}\right)}{q\left(^{118}Sn^{49+}\right)}\frac{M\left(^{118}Sn^{49+}\right)}{M\left(^{12}C^{5+}\right)} = \frac{5}{49}\frac{M\left(^{118}Sn^{49+}\right)}{M\left(^{12}C^{5+}\right)}. \tag{8.1}$$

Carbon is also a good reference ion, as it has a small binding energy which can be overcome in the mini-EBIT, so it could be loaded during the ongoing tin campaign. Furthermore, Carbon-12 is used for the definition of the atomic mass units, therefore having a small mass uncertainty[2].

Following up on Section 7.2, multiple ions with different charge states were stored during the 98

[1] This similarity was actually part of the motivation to chose the tin-118 isotope. Shout out to José Crespo, who provided an enriched tin sample from his isotope storage.

[2] While the neutral mass is defined as exactly 12 u, the hydrogen-like ion must be corrected for the removed electrons and their binding energies, leaving a small uncertainty on the mass of the ion, which actually completely cancels in the g-factor error budget when using the old Codata value for the electron mass, which was determined by the g-factor measurement of hydrogen-like carbon. Nonetheless, the uncertainty of the hydrogen-like carbon mass is too small to be of relevance here.

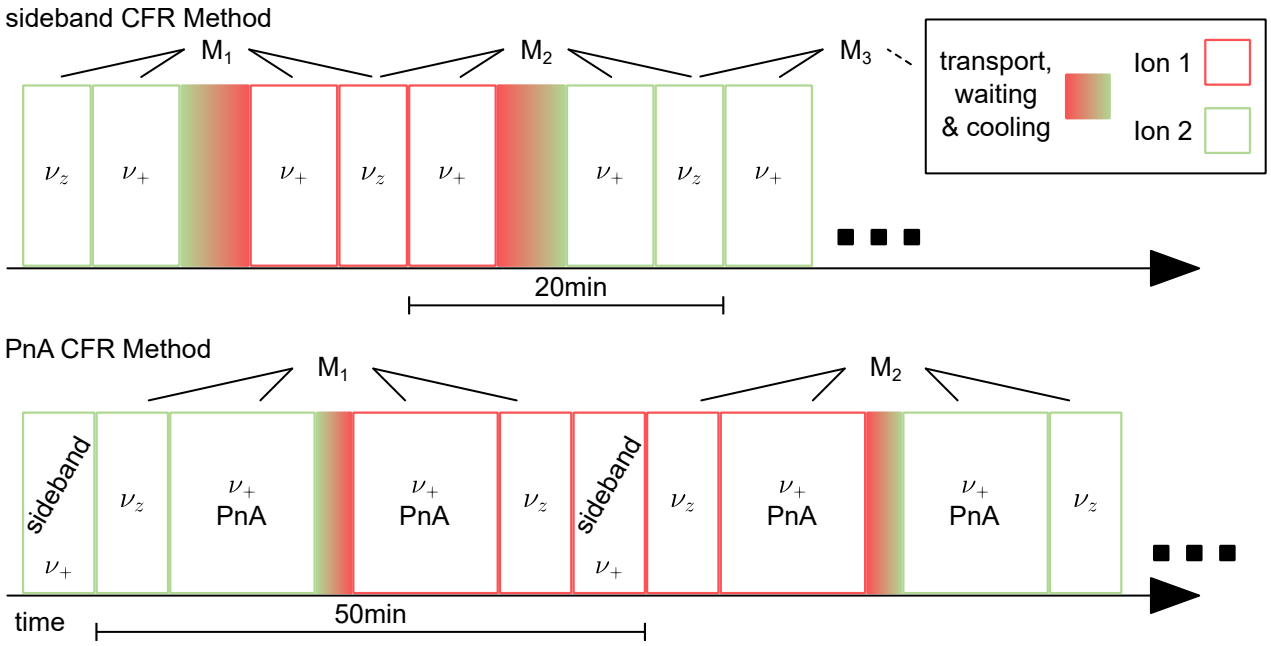

Fig. 8.1: CFR measurement schemes for the *double-dip* measurement and the phase sensitive method. Although the sideband method has a quicker cycle time, the precision of the PnA method is much higher, as the frequency measurement is more accurate.

day long tin campaign. At the time of the mass measurement, the two available tin charge states in the trap were hydrogen-like and boron-like, both of these were used for the mass measurements in order to test for additional systematic effects.

8.1 Double-Dip CFR

Prior to phase-sensitive measurements, cyclotron frequencies were often measured with the *double-dip* method, introduced in the Penning-trap chapter (Chap. 3). These are very useful for a number of reasons. From a technical point they are simpler, and typically quicker, than the nowadays frequently used phase-measurements [98]. Nonetheless, it comes with two main drawbacks:

On the one hand, the shot-to-shot stability is significantly worse than with the phase measurements. Therefore, requiring more averaging to achieve a similar uncertainty[3]. The second problem with the *double-dip* method lies in the lineshape used for the fit, which can cause systematic shifts in the frequency determination. This typically requires rather involved studies to quantify/reduce the connected systematic effects. This is because the fit uses a large number of auxiliary parameters, such as the resonance frequency of the tank circuit and it is therefore a difficult task to give good estimates of the overall systematic effects. Thus, the *double-dip* CFRs presented here are for the sole purpose of cross checking the PnA measurement, which is described in the following section. Fig. 8.1 shows the measurement sequence used for the mass determination. It is an adapted version of the Extended Data Figure from Ref. [54].

For the measurement, the two ions are stored separately above and below the PT[4]. One after the other are transported into the PT to determine the free-space cyclotron frequency. For each ion the electric potential is changed to bring the axial frequency in resonance with the detector. The ν_+ measurement via *double-dip* is carried out directly before transporting out of the PT and

[3] Additionally, the achieved uncertainty scales only with the square root of the number of measurement points, while a better shot-to-shot jitter translates linear to smaller statistical uncertainty.

[4] In the AT and the capture section.

directly after transporting into the PT, although here a wait time is added since the electrostatic potential needs a certain settling time. The axial frequency ν_z is measured in between the two *double-dip* measurements. Combining the neighboring frequency measurements to extract the free-space cyclotron frequency[5], as shown in Fig. 8.1, allows the determination of a ratio M_n. This is repeated several times and analyzed to extract a mean value and a statistical uncertainty.

8.2 Phase-Sensitive Measurement

In addition to the measurement with *double dips*, the PnA technique, as explained in the Penning-trap chapter Sec. 3.3.1, was also used to determine the CFR of hydrogen-like tin and carbon. The measurement sequence is shown at the bottom of Fig. 8.1.

An advantage of PnA is that due to the similar q/M, each ion can be measured in the same electric potential. This is not possible for the sideband method, as each ion must be in resonance with the detection circuit in order to have a good signal. For hydrogen-like tin and carbon the same set of voltages on the electrodes results in an axial frequency difference of a bit more than 830 Hz.

In PnA the particle is axially excited to measure the phase as explained in the Penning-trap chapter. This still works 830 Hz detuned from the center. Especially with the highly charged tin ion, the detection of the peak signal, which scales with the charge q, results in precise phase readout of the peak signal. Therefore, to detect both ions using the same set of voltages, the axial frequency of $^{12}C^{5+}$ is set in resonance with the detection circuit while the tin ion sits off-resonant on the side. This far detuned, the *dip* and *double-dip* technique are slow. Good convergence of the FFT signal was only achieved after an averaging time of more than 4 minutes. Furthermore, the lineshape used for fitting could potentially add additional systematics to the measurement. The measurement of ν_+ with PnA does not depend on a large number of parameters included in the fitting of dips and double dips, suppressing all related systematics.

The decrease in signal due to being off-resonant is compensated by a stronger coupling pulse, increasing the axial radius for a higher SNR as shown in Eq. (3.21). With tin this can still be achieved without the trap anharmonicities causing problems in the measurement. As with the *double-dip* sequence, the ν_+ measurement with PnA happens directly before and after transport, since ν_c is most sensitive to ν_+ due to the frequency hierarchy of the motional frequencies. The axial frequency is measured before and after the PnA sequence respectively. In the middle of both, ν_+ is measured with a *double dip* to ensure correct phase unwrapping with the PnA measurement. Since the PnA sequence is quite long, the cycle time of 50 min is significantly higher in this approach. Although with the higher shot-to-shot stability, the measurement points M_n have much smaller spread and average quicker than in the sideband method.

Note that for this measurement in particular, special care was taken to measure the two particles in the very same trapping state. That means that all electrodes were set to the exact same setting for the measurement of both particles.

8.3 Systematic Effects

For an accurate determination of the mass(ratio), the systematic effects must be quantified carefully. In the following the most important findings are presented.

[5] The magnetron frequency is only measured before and after the CFR measurement takes place. This is sufficient since with the invariance theorem, it barely influences ν_c.

Electrostatic Potential

It is known that the sudden voltage changes during the transports subsequently cause a minute-scale long drift of the trap potential, which can easily translate into a systematic shift of the measured CFR. Fortunately, since the ions are measured in alternating order, this cancels out because the shift is opposite in both cases.

Another effect that is not trivial to quantify is the shift due to a different axial potential. For the *double-dip* method, each particle is measured in resonance with the axial detection circuit. To tune the ion frequency to the resonator, the electric potential is changed. This tuning can lead to subtle systematic shifts. While the electrode voltages are changed symmetrically, in reality that symmetry is broken by inhomogeneous patch potentials on the electrodes[6]. Consequently, the trap minimum can differ slightly for both ions. Combined with unavoidable inhomogeneities of the magnetic field, the two ions probe different magnetic fields, which in turn shifts the measured CFR. In a different setup with a similar trap design the patch potentials have been measured to be smaller than 10 mV [47], although values up to some 100 mV have been reported before [136]. Such a shift in position, combined with the present magnetic field inhomogeneities (i.e. $B_1 = 2.64(3)^{\mathrm{mT}}/_{\mathrm{m}}$), would therefore cause a systematic shift in the measurement. To avoid this, instead of the ion's frequency the resonator could be shifted to keep the electrical potential constant [137]. At ALPHATRAP the necessary circuitry is not implemented, as it was not built for this specific purpose. Therefore, the *double-dip* CFR measurement relies on shifting the ion onto the resonance.

The charge-to-mass ratio q/M of $^{118}\mathrm{Sn}^{49+}$ and $^{12}\mathrm{C}^{5+}$ differs only by 0.3 %. The change in the axial potential is therefore only 0.15 V, which is quite small compared to the trap voltage of around -59 V. To quantify this systematic effect, the CFR between hydrogen-like tin and boron-like tin was measured along with the CFR of boron-like tin and hydrogen-like carbon. These have a significantly different q/M ($\approx 84\,\%$) but the mass difference of the two different charge states is known quite well. Therefore if the patch potentials cause a significant shift these ratios should exhibit large disagreement to the expected difference. As these two measurements showed agreement with the prediction to about 0.2 ppb this particular systematic effect must be significantly smaller in the CFR of the hydrogen-like tin and carbon ion[7]. Assuming linearity, this would be a shift of 3.6 ppt, negligible in the measurement. Shifts due to the electrostatic anharmonicity of the trap have been studied in detail as explained in the following chapter. In the mass measurement these have a negligible effect since the precision is lower than in the g-factor measurement. Furthermore, these shifts are suppressed in the PnA result, since both use the same trap and therefore experience the same shift in first order.

Temporal Drifts

Something to consider is also the time separation of the frequency measurements for each ion. A continuous drift of the magnetic field would therefore cause a systematic shift in a single measurement point M_n. However, due to the dual measurement scheme, where the ions are always measured in alternate order, linear drift does not cause a systematic shift in the final result, as ratios where ion 1 is measured first are shifted in the opposite direction to those where ion 2 is measured first. The observed magnetic field drifts during the measurements show that second order effects are to small to be of significance for the values presented here.

[6] Due to surface contaminants, which have different work functions and change the potential at the surface.

[7] For this to be true we assume the shift to be a linear function, which is the case if it is purely caused by patch potentials.

Image-Charge Shift

Another systematic effect that shifts the CFR is the image-charge shift (ICS) as explained in Sec. 3.2.2. It scales linearly with particle mass, so it affects the tin ions much more than carbon. For any measurement of tin against carbon this is a shift of 1.4×10^{-10} with an uncertainty of 0.7×10^{-11}. For measurements between different tin charge states, the shift is suppressed by a few orders of magnitude because the masses of both particles are very similar.

Relativistic Correction

The relativistic correction, as explained in Sec. 9.2.2, has a negligible effect on the double-dip measurements, since for particles thermalized by sideband coupling to an axial temperature of 6 K[8] the resulting shift is less than 0.2×10^{-12}. In the PnA measurement though the particle is excited to rather high amplitudes, causing a shift and a connected uncertainty that has to be included in the error estimation.

8.4 Measurement Overview

The complete mass campaign is summarized in Tab. 8.1. Fig. 8.2 visualizes the performed CFR measurements of the three ions. R_1 is the PnA-based CFR determination between hydrogen-like tin and carbon. R_2, R_3 and R_4 are the individual ratios between the three ions $^{118}Sn^{49+}$, $^{118}Sn^{45+}$ and $^{12}C^{5+}$ measured via *double dip*. R_5 is the mass ratio between boron-like and hydrogen-like tin measured with PnA, both ions on resonance, as the q/M is too different. R_6 is a cross check measurement with the hydrogen-like tin ion comparing the *off resonance* case 830 Hz away with the *on resonance* one. It uses the same measurement scheme as for R_1 but without transport and instead a change of potential to shift the particle off and on resonance. Lastly, R_7 is a direct comparison between the sideband method and the PnA method. R_8 is the theory value for the mass ratio, namely the binding energy and the masses of the additional electrons. The binding energy difference between the hydrogen and boron-like case was calculated by Chunhai Lyu in the group of Zoltán Harman, the total binding difference is 58457.2(8) eV[9]. With this a more precise comparison can be done compared to only using the values reported in the Atomic Spectra Database [50]. R_9 is the AME literature value of the mass ratio $^{118}Sn^{49+}$ to $^{12}C^{5+}$ [135].

8.5 Result

Overall, the measurements provide a value for the hydrogen-like tin mass with a precision of 4×10^{-10}. In certain measurements, systematic effects are more difficult to quantify. A major uncertainty in the sideband measurements lies in the treatment of the vastly different dip widths and its impact on the determination of ν_+. In R_4, the two ions exhibit similar dip widths, so any systematic shift on the modified cyclotron frequency would cancel largely. R_2 and R_3 though, incorporate a 10-fold different dip width, causing an unknown systematic effect on these ratios. Much safer in their systematic treatment are the phase measurements. R_1 is independent of the linewidth for the ν_+ determination[10]. Therefore, the remaining systematic effects are due to the relativistic mass increase and the image charge shift (ICS). The ICS scales with the particle mass, therefore it does not drop out in the ratio due to the vastly different masses.

[8] This temperature was measured in the apparatus, as explained in the next chapter (Chapter 9).

[9] Private communication.

[10] It still relies on the fitting of the axial frequency, but this gives as later discussed for the g-factor measurements an uncertainty on the 2×10^{-11} level, too small to be of relevance.

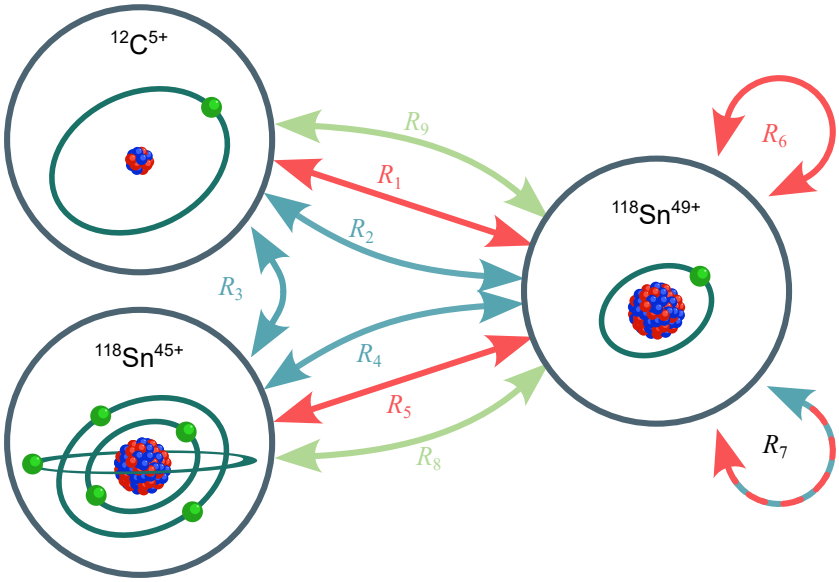

Fig. 8.2: Overall seven measurements on the mass were performed (R_1 to R_7). These were performed either with PnA (red), or with sideband methods (blue). The green lines are those taken from theory (R_8) or AME (R_9).

The relativistic effect is dominated by the modified cyclotron radius $\hat{r}_+$ during the free evolution time. Both particles are roughly at the same radius of 40 µm. Since the frequencies are very similar, the relativistic shift is correlated and mostly drops out. To be conservative, the correlation is neglected, and the error is taken fully into account. After correction, this brings an additional relative uncertainty of 2.8×10^{-10}. Note that the uncertainty here is quite large because the radius calibration for the carbon ion was less accurate than for tin. Therefore an error of 100 % is assumed on the relativistic correction for the free-space cyclotron frequency of carbon. In reality this should be smaller, as identical excitation parameters were used for carbon and tin. Because the frequencies are so close and the radius after excitation scales with q/M, their radii must be very similar [86]. This is further supported by the measurements performed with the boron-like tin ion. With the same parameters as hydrogen-like tin it showed a nearly identical excitation radius (see Tab. 9.2). Nonetheless, the conservative error estimate is chosen for the relativistic effect. Overall, the mass ratio between hydrogen-like tin-118 and carbon-12 is determined to be:

$$\frac{M\,(^{118}\mathrm{Sn}^{49+})}{M\,(^{12}\mathrm{C}^{5+})} = 9.8251510645(39)_{\mathrm{stat}}(27)_{\mathrm{sys}}. \tag{8.2}$$

Note that this is based on a rather small dataset of only five recorded ratios, therefore, to be safe, the statistical error is based on the standard deviation, and not on the standard deviation of the mean. Combined with the carbon mass – corrected for missing electrons and binding energies[11] – enables to extract the hydrogen-like tin mass.

$$M(^{118}\mathrm{Sn}^{49+}) = 117.874869069(47)_{\mathrm{stat}}(32)_{\mathrm{sys}}\,\mathrm{u}. \tag{8.3}$$

This is a factor 10 improvement over the value reported in the Atomic Mass Evaluation[12] [135].

Tab. 8.2 is a compilation of relevant cross checks testing the consistency within the measurements. Apart from the 1.8-sigma tension between R_1 and R_2, the measurements seem to be in good agreement. It is not clear why these show this tension. While it could simply be a statistical error, other systematic effects like the lineshape of the *double-dip* could be the reason for this. For

[11] The hydrogenlike carbon mass is 11.99725768029217(43)(8) u with the uncertainty in the brackets coming from the binding energies and the electron masses respectively. (Ref. [50, 138])

[12] Corrected with the binding energy from the Atomic Spectra Database [50] and the electron mass from CODATA [138]

Tab. 8.1: Summary of all recorded CFR measurements along with the theory value calculated by Chunhai Lyu in the group of Zoltán Harman (R_8) and the ratios taken from AME (R_9). All measured values are corrected for the relativistic shift and the image-charge shift. Apart from the separately labeled uncertainties in R_1, the shown uncertainty brackets only show the 1-sigma statistical uncertainty.

Ratio	Method	Value	# of cycles
$R_1 \equiv \frac{M\left(^{118}\mathrm{Sn}^{49+}\right)}{M\left(^{12}\mathrm{C}^{5+}\right)}$	PnA	$9.825\,151\,064\,5(39)_{\mathrm{stat}}(27)_{\mathrm{sys}}$	5
$R_2 \equiv \frac{M\left(^{118}\mathrm{Sn}^{49+}\right)}{M\left(^{12}\mathrm{C}^{5+}\right)}$	sideband	$9.825\,151\,054\,8(22)$	44
$R_3 \equiv \frac{M\left(^{118}\mathrm{Sn}^{45+}\right)}{M\left(^{12}\mathrm{C}^{5+}\right)}$	sideband	$9.825\,328\,730\,3(27)$	33
$R_4 \equiv \frac{M\left(^{118}\mathrm{Sn}^{45+}\right)}{M\left(^{118}\mathrm{Sn}^{49+}\right)}$	sideband	$1.000\,018\,083\,55(29)$	82
$R_5 \equiv \frac{M\left(^{118}\mathrm{Sn}^{45+}\right)}{M\left(^{118}\mathrm{Sn}^{49+}\right)}$	PnA	$1.000\,018\,083\,50(12)$	16
$R_6 \equiv \frac{\nu_c^{\text{on Resonance}}}{\nu_c^{\text{off Resonance}}}\left(^{118}\mathrm{Sn}^{49+}\right)$	PnA	$1.000\,000\,000\,08(24)$	15
$R_7 \equiv \frac{\nu_c^{\mathrm{DD}}}{\nu_c^{\mathrm{PnA}}}\left(^{118}\mathrm{Sn}^{49+}\right)$	sideband & PnA	$1.000\,000\,000\,31(21)$	72
$R_8 \equiv \frac{M\left(^{118}\mathrm{Sn}^{45+}\right)}{M\left(^{118}\mathrm{Sn}^{49+}\right)}$	Theory	$1.000\,018\,083\,27(10)$	–
$R_9 \equiv \frac{M\left(^{118}\mathrm{Sn}^{49+}\right)}{M\left(^{12}\mathrm{C}^{5+}\right)}$	AME	$9.825\,151\,032(45)$	–

reference, the data of the measurements R_1 and R_2 are shown in Fig. 8.3.

8.5.1 Neutral Mass

With the hydrogen-like tin mass improved by a factor of 10, it follows that the neutral mass can be improved by the same factor. This requires to adding the mass of the 49 extra electrons and subtracting the difference in binding energy between the neutral atom and the hydrogen-like ion. The electron mass is known with sufficient precision, but the binding energy is only known to about 150 eV [50]. This limits the result for the neutral mass to about 1.4×10^{-9}, which would be only a factor of three better than the previous literature value [135]. Therefore, to combine it with this measurement, the binding energy was calculated by the group of Zoltán Harman. Chunhai Lyu performed *ab initio* multiconfiguration Dirac–Hartree–Fock (MCDHF) calculations as described in detail in Ref. [54]. This predicts the binding difference as 132748(5) eV, a factor of thirty improvement over the NIST atomic spectra database. Combined, the neutral mass is

Comparison	Results (ppb)	Agreement
$R_2/R_3 \times R_4 - 1$	-0.16(46)	-0.3
$R_2/R_3 \times R_8 - 1$	-0.45(36)	-1.2
$R_1/R_3 \times R_8 - 1$	0.52(56)	0.9
$(R_1 - R_2)/R_1$	0.96(53)	1.8
$(R_1 - R_9)/R_1$	3.4(46)	0.7
$(R_4 - R_5)/R_4$	0.06(32)	0.2
$(R_4 - R_8)/R_4$	0.28(31)	0.9
$(R_5 - R_8)/R_5$	0.23(16)	1.5
$R_6 - 1$	0.08(24)	0.3
$R_7 - 1$	0.31(21)	1.5

Tab. 8.2: Cross checks of the various measurements performed on the three ions. For reference, the final relative measurement uncertainty of the 118-Sn mass is 0.47 ppb. The *Agreement* column is in units of σ, the confidence level for the compared measurements.

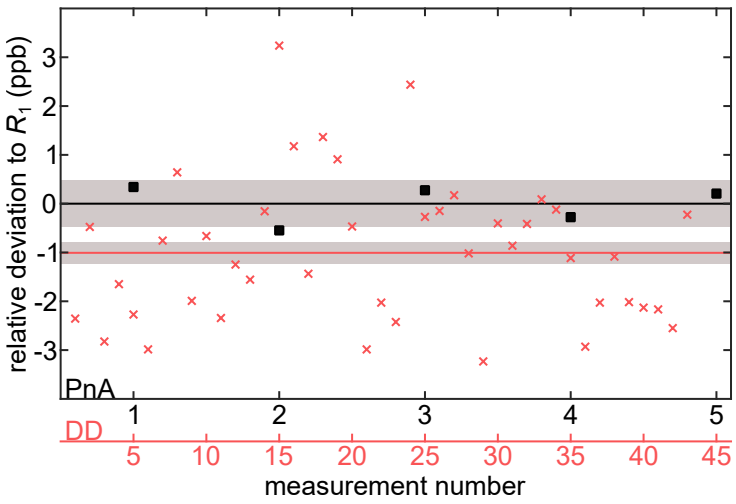

Fig. 8.3: Data from the PnA CFR measurement R_1 and from R_2, the *double-dip* (DD) CFR determination. The horizontal lines are the mean values, with the corresponding confidence interval in grey. The two measurements deviate by about 1.8-sigma.

determined to be:

$$\begin{aligned} M\left(^{118}\mathrm{Sn}\right) &= M\left(^{118}\mathrm{Sn}^{49+}\right) + 49m_\mathrm{e} - \frac{\Delta E}{c^2}, \\ M\left(^{118}\mathrm{Sn}\right) &= 117.901606974(56)_\mathrm{exp}(5)_\mathrm{theo}\,\mathrm{u}. \end{aligned} \tag{8.4}$$

It agrees with the AME literature value, but is ten times more precise. Nevertheless, the presented precision is about an order of magnitude worse than the Γ_0 precision, which ultimately limits the uncertainty of the g-factor measurements to 5×10^{-10}. At present, a more precise measurement is not required, as any QED test using highly charged tin is limited by the theoretical uncertainty. However, dedicated mass measurement experiments have achieved uncertainties that are more than an order of magnitude lower, so the mass can be further improved if necessary [139–141].

Chapter 9

Experimental Results: Highly Charged Tin g Factors

The main goal of the tin campaign was to determine the bound-electron g factor of hydrogen-like tin. This was possible by combining two rather unique setups, namely the Heidelberg EBIT and the ALPHATRAP apparatus, to test QED under the extreme conditions of a tightly bound $1s$ electron. During the campaign, the initially hydrogen-like ion underwent electron capture processes to the lithium-like and later to the boron-like charge states. Conveniently, these events occurred on timescales that enabled to measure the g factor of these charge states as well, each providing an interesting and useful test of their respective theory, probing the Standard Model in different ways at medium-to-high Z.

This chapter describes the measurement methods, followed by the discussion of systematic effects. Finally, the measurement results are presented. The comparison with their respective theoretical predictions, can be found in the conclusion in Chap. 11.

9.1 Measurement Sequence

The three different ions for which the g factors were determined are similar enough that the same measurement scheme could be used for all three cases. Furthermore, they all share the same systematic effects to similar extend. Nevertheless, the critical parameters must be investigated for each ion individually to ensure accurate results, as discussed in the following sections on systematics. The sequence is shown in Fig. 9.1, employing the double-trap method [20] which exhibits low systematic effects, important to achieve highest precision on Γ_0.

The measurement starts in the Analysis Trap (AT), here the continuous Stern-Gerlach effect (Sec. 3.4) is employed to determine the spin-orientation/spin-state of the ion. As described in Sec. 7.3, for all three charge states, this is performed using the prior described phase-sensitive method, which results in a near 100 % spin-flip fidelity[1]. Afterwards, the ion is transported into the Precision Trap (PT), where it initially waits for two minutes to let the applied voltages settle for a stable axial frequency. Next, using sideband coupling, the modified cyclotron motion is determined which is necessary to ensure correct unwrapping in the subsequent PnA sequence. Afterwards, the axial frequency is measured with a *dip* measurement. This is directly followed by the PnA sequence, which includes the phase measurement of four different evolution times (0.2 s, 0.5 s, 2.2 s and 5.2 s). Each cycle, referring to the measurement of the accumulated phase with

[1] Over the course of complete measurement run, the data suggests a perfect unambiguous spin-flip determination.

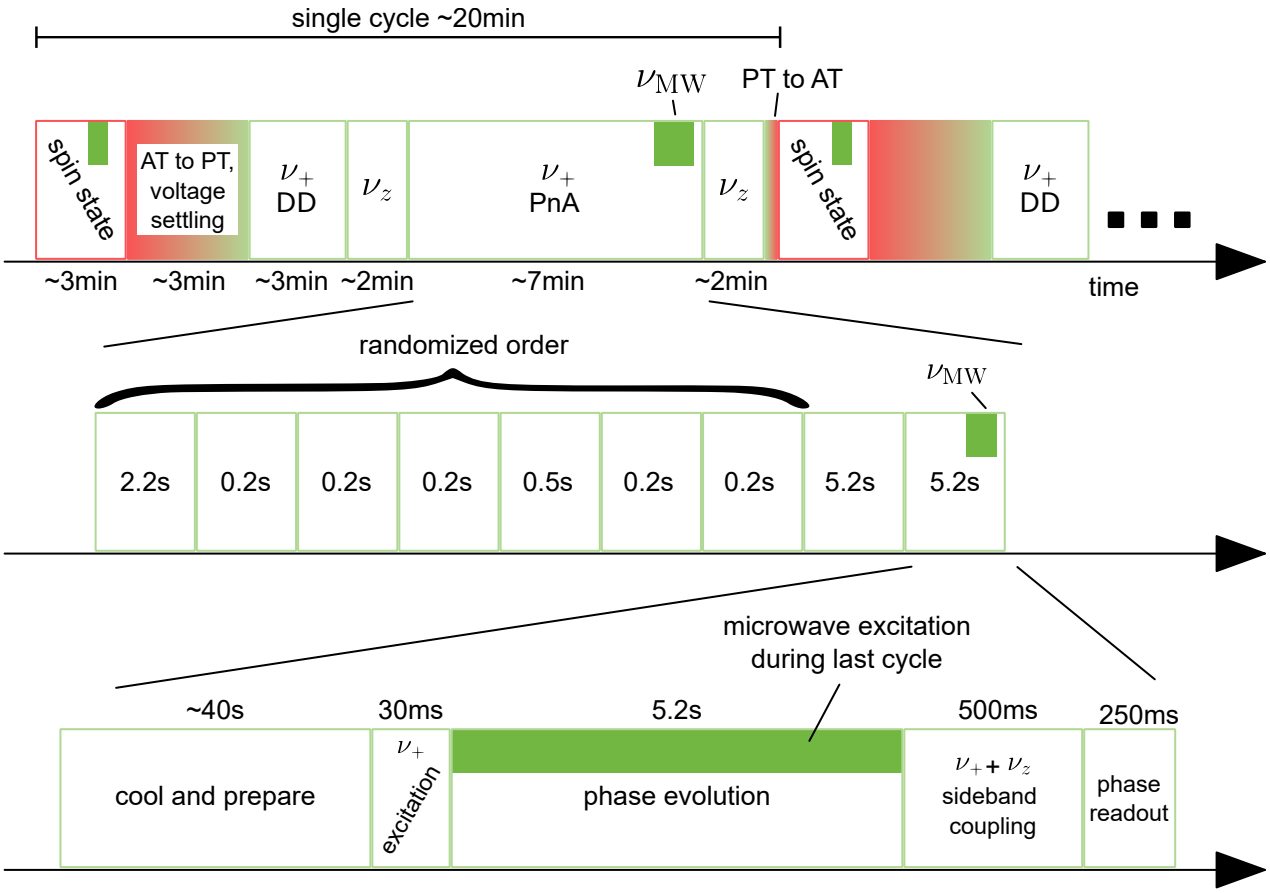

Fig. 9.1: Detailed measurement scheme for the determination of Γ_0. Figure adapted from Ref. [54]. Details can be found in the text. DD is short for double dip.

one specific evolution time, starts by sideband cooling the modified cyclotron mode. The shortest evolution time is for the reference phase, which is measured five times and averaged to reduce additional uncertainty from its readout jitter. The 0.5 s and the 2.2 s measurements are used for unwrapping, in order to perform n determination for the long evolution time with the microwave irradiation. These are also used to check for systematic effects, as any inconsistency with the other phase measurements would exhibit non-linear behavior of these. The shorter evolution times are in randomized order and lastly followed by two phase measurements with 5.2 s evolution time. The first is used to predict ν_c precisely for the subsequent cycle. This is helpful, as during the following cycle, the microwave with frequency ν_{MW} is injected. Therefore the prior determination of ν_c gives a better guess of the Γ that will be tested by this cycle, avoiding to probe points far away from the intended value, which would not contribute (significantly) to the final uncertainty of the measurement. The microwave frequency ν_{MW} being probed is then chosen with a random distribution around the expected center. To resolve both the center, the flanks and the outside of the resonance, this distribution is chosen wider than the expected width, which is estimated based on prior resonances taken.

After the PnA sequence, the axial frequency is measured again. Transport back into the AT completes a cycle, which then starts anew with the spin-flip detection. From the individual spin-flip measurements in the AT, one can then determine which microwave injection in the PT caused a spin flip. This results in a binomial type dataset with successful PT spin flips at the ratios Γ_{SF}, and with the unsuccessful PT spin flips at the ratios Γ_{noSF}. For each, ν_c is determined via the invariance theorem, Eq. (3.8). ν_+ is taken exclusively from the five reference phases and the last long evolution time during the microwave injection. ν_z is taken from the weighted

average of the two dip measurements before and after PnA. The weighting is biased towards the second ν_z measurement as this is chronologically closer to the microwave injection. So basically ν_z is linearly interpolated between the two dips to better estimate the frequency during the PnA sequence. Lastly, ν_- is taken from a dedicated sideband measurement which is conducted every few measurement cycles, since it typically drifts only sparsely, and contributes only little to ν_c.

A complete measurement typically consists of a few hundred points scattered around the resonance. Using maximum-likelihood methods, the fit parameters including the center of the resonance Γ_{stat} are extracted. Correcting this for systematic shifts, as detailed in the following, enables to extract the Larmor-to-cyclotron frequency ratio Γ_0, which is combined with the literature values for the particle masses and the charge ratio to extract the g factor.

9.2 Error Sources and Systematic Effects

Heavy highly charged ions (HCI) have a significant advantage over lighter ions[2]. Due to their high charge and mass the thermal radius is small, which ultimately leads to significantly smaller systematic shifts since the higher anharmonicity coefficients impact the motional frequencies less. Nonetheless rigorous treatment of systematics is a *must-have* for any high-precision measurement. A complete tables summarizing the systematic effects for the three g-factor is given in Tab. 9.3.

9.2.1 Image-Charge Shift

The image-charge shift (ICS) was introduced in the Penning-trap chapter (Sec. 3.2.2). While most other systematic effects reduce with heavier masses, this is directly proportional to it:

$$\frac{\Delta\nu_c}{\nu_c} \propto \frac{M}{B_0^2 r_0^3}. \tag{9.1}$$

ALPHATRAP was designed with heavy HCI in mind, so a large trap radius of $r_0 = 9\,\text{mm}$ was chosen. For tin, the three charge states have roughly the same masses[3], so the ICS is very similar for each. The shift is therefore, following Ref. [93]:

$$\frac{\Delta\nu_c}{\nu_c} = 1.484(75) \times 10^{-10}. \tag{9.2}$$

The error is chosen as to 5 % of the overall shift [93]. This is a rather conservative estimate, as the system is well understood, and the manufacturing error is quite small. Note that there are possibilities to measure the ICS in order to achieve higher accuracy for a better cyclotron frequency determination. In Ref. [141] an uncertainty of about 1 % was achieved. Nonetheless, for the results presented here, a higher accuracy is not necessary, as the 5 % uncertainty is significantly smaller than the statistical uncertainty.

9.2.2 Relativistic Correction

Another shift that plays a significant role is the relativistic mass increase of the particle. Although the particle, with a velocity of about $2\,000\,\text{m/s}$, is orders of magnitude slower than the speed of light, the relativistic correction still has a significant effect on the result of the measurement due to the high precision achieved. Also introduced in the Penning-trap chapter, the shift scales simply with the energy of the particle, therefore in first order with the velocity of the

[2] Highly charged means in this context that most of the electron are removed, as is the case for the three charge states presented here.

[3] On the level of ICS uncertainty this assumption is correct

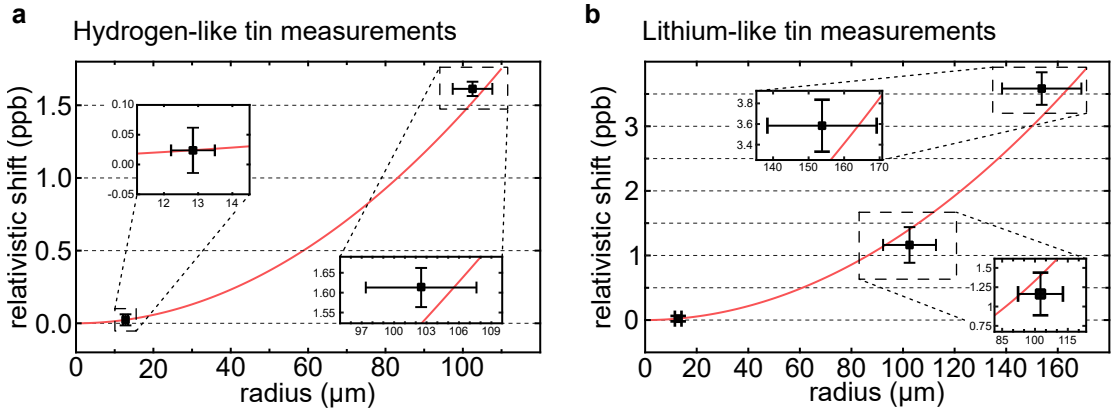

Fig. 9.2: The relativistic correction for a given radius is shown. The different measurements (**a** includes those with hydrogen-like and **b** those with lithium-like tin) with their measurement uncertainty and their radius uncertainty are shown.

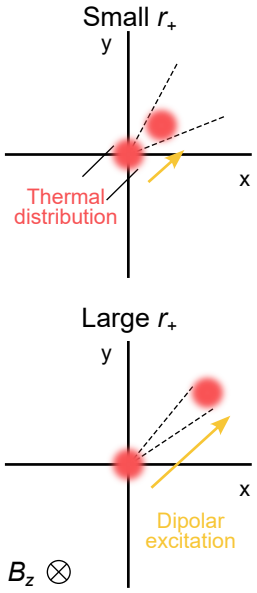

Fig. 9.3: The starting phase of the free evolution time to measure ν_+ is far better defined for stronger dipolar excitation.

particle squared[4]. During PnA, the modified cyclotron radius is increased to produce a repeatable starting phase for the motion. The radius must be significantly above the thermal radius, otherwise the measured jitter is limited by the jitter of the starting phase, as shown in Fig. 9.3. Because of the relativistic mass increase, the modified cyclotron frequency is shifted, which requires to correct the measured frequency as described in Sec. 3.2.2. In all three main resonances, the same *amplitude* × *time* product for the modified cyclotron excitation pulse was used. For each, a calibration measurement was carried out to determine the radius after excitation. For this the trap is intentionally detuned that it has a well defined and non-zero fourth-order electrostatic coefficient C_4, which shifts the axial frequency with an r_+^2 scaling, as shown in Eq. (3.11). The shift is measured for different dipole excitation strengths, as the excitation radius increases proportionally with the *amplitude* × *time* product[5]. The shift versus excitation strength is fitted to obtain the calibration. For all three charge states the calibration showed similar radii around 12.5 µm for a 0.2 V× 30 ms pulse, which is the setting used for the g-factor measurements. A conservative 10 % uncertainty is assigned, resulting in a 20 % uncertainty in the relativistic correction.

Two separate methods were used to cross check this systematic effect. For once, multiple resonances at varying cyclotron radii have been measured for hydrogen-like and lithium-like tin. The comparison is shown in Fig. 9.2. All agree within the measured uncertainty. This is often used to extrapolate the shift to zero radius, which makes sense if higher precision is needed. Instead the error was kept with 10 % uncertainty on r_+. Nonetheless, to cross-check a third method was used to confirm correct radii. This is done with a PnA measurement. By repeatedly measuring short and long phases for different radii the frequency shift can be determined precisely. The phase difference $\Delta\phi$ will in first order obey:

$$\Delta\phi(\hat{r}_+) \approx \Delta t\, \omega_+ \frac{\omega_+^2 \hat{r}_+^2}{2c^2}. \tag{9.3}$$

This agreed with both other methods, although suggesting that the radius might be 10 % higher than measured with C_4. Since it is still within the given error bar, and higher accuracy is not required, further investigation was not done.

[4] Or radius, as $\hat{v} = \omega r$

[5] Assuming that the frequency of the particle is still resonant with the pulse in the frequency domain which gets narrower for long pulses, requiring to precisely set the frequency of the pulse.

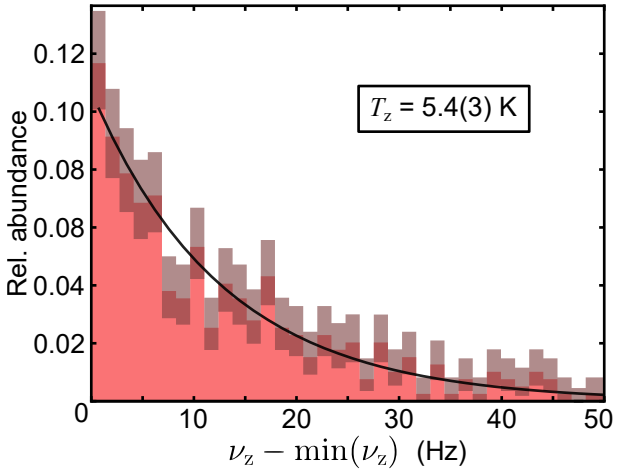

Fig. 9.4: Axial frequency distribution in the AT. Data from the hydrogen-like tin g-factor measurement. The uncertainty from each point is evaluated from the amount of points in each bin. From the fit, the temperature of the axial mode is evaluated as 5.4(3) K.

9.2.3 Motional Temperature

As discussed in the Penning-trap chapter (Chapter 3), the particle is thermalized with the axial detector, which results in a T_z near the temperature of the detector. The radial modes are cooled via sideband coupling to a temperature of $T_+ = T_z\, \nu_+/\nu_z$. This temperature distribution can be measured in the AT, where the strong $B_2 = 42.77\,\mathrm{kT/m^2}$ and the magnetic moment of the cyclotron motion[6] cause an axial frequency shift, following Eq. (3.24). The shift scales with the radial quantum number $\hat{n}_+$. Based on the observed distribution of the axial frequency in the AT the expectation value of $\hat{n}_+$ can be determined.

During the Γ_0 measurements, every measurement cycle the particle is transported into the AT where the trap voltages are set to the same potential. Each time, the axial frequency is slightly different based on value of the $\hat{n}_+$. The distribution observed during the complete measurement run can be fitted, to measure the expectation value of $\hat{n}_+$. From this, the average axial temperature follows as due to the sideband coupling $n_z = \hat{n}_+$. For all three g-factor measurements, the frequency distribution was analyzed, and the resulting axial temperatures are given in Tab. 9.2. Fig. 9.4 shows the AT axial-frequency distribution (subtracted by the smallest observed frequency) in the hydrogen-like tin measurement. The uncertainty of the measured frequency is taken from the fit.

9.2.4 Dip Lineshape

In the presented measurement, the axial frequency is measured by fitting the FFT signal of the detector output. While the lineshape for the fit is known well, it incorporates many auxiliary parameters that can impose systematic shifts on the measured frequency. For a single dip, the dominant uncertainty lies in the correct treatment of the image-current shift, which is an effect that comes from the interaction between the resonator and the particle. If the motional frequency is slightly detuned from the resonance center, it is shifted closer to the resonator, hence it is often referred to as *frequency pulling*. The shift of the axial frequency is given by

$$\Delta\nu_z = \frac{q^2 \mathrm{Im}\,(Z)}{4\pi M d_{\mathrm{eff}}^2}, \tag{9.4}$$

with q as the charge, M as the mass, d_{eff} as the effective electrode distance and Z the impedance of the LC circuit as given in Eq.(3.16).

While it is theoretically well understood and accounted for by the lineshape model, it can

[6] The shift from the magnetic moment of the magnetron mode can be neglected here as the axial frequency shift is a factor of ν_-/ν_+ smaller.

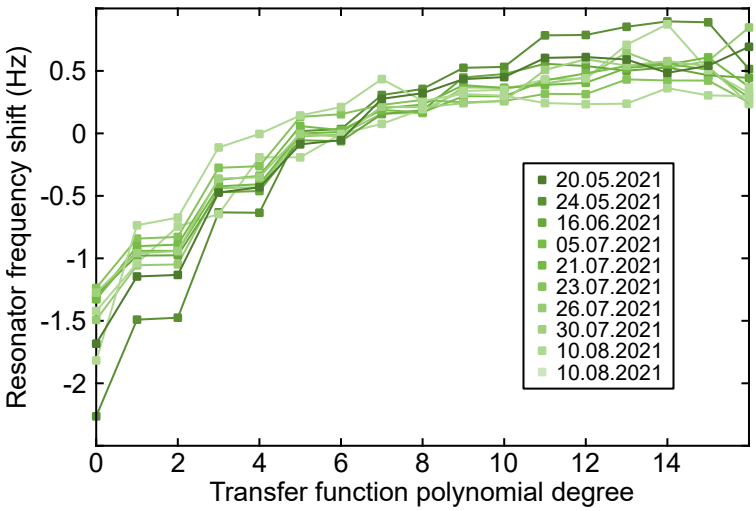

Fig. 9.5: Multiple resonator spectra recorded regularly during the measurement campaign are shown. They are fitted with the theoretical resonator function combined with a polynomial to include the transfer function of the amplifier. The x axis is the highest included polynomial order k in the fit. They seem to follow a clear pattern over the course of the three month. Each individual dataset is subtracted by its mean frequency, to overlap the individual measurements.

cause problems if the resonance frequency is systematically shifted in the fit. Specifically, if the resonator frequency is uncertain, the resulting image-current shift is uncertain, which translates into an uncertainty in the measured axial frequency [142].

Estimation of the magnitude of this means testing the accuracy of the detection circuits resonance frequency. From an electrical point of view, the circuit appears to be simple, but the complete signal chain from the resonator to the FFT analyzer is quite long, resulting in incomplete knowledge of the transfer function, which can easily become non-linear due to parasitic capacities and inductances. Thus a the resonator frequency determined by the fit (which assumes a linear transfer function) might be systematically shifted.

For the presented measurements this uncertainty is estimated by fitting the resonator with the idealized lineshape model together with a transfer function of varying polynomial degree of the form

$$u_{\mathrm{out}}(\mathrm{dBV_{rms}}) = u_{\mathrm{in}}(\mathrm{dBV_{rms}}) + \sum_{n=1}^{k} A_n(\omega - \omega_{\mathrm{res}})^n. \tag{9.5}$$

In Fig. 9.5, various empty[7] resonator spectra recorded during the measurement campaign were tested on how their frequency shifts as a function of the fitted polynomial order for the transfer function. Interestingly, throughout the campaign, the overall trend stays the same, suggesting that the transfer function is rather constant over time. Between zeroth and sixteenth order the frequency varies by about 2 Hz. This suggests, that a ν_{res} uncertainty of ± 1 Hz is a reasonable estimate. This uncertainty in turn results in a 20 mHz uncertainty of the image-current shift for the highly charged tin, and with it the axial frequency of the particle. For example in the Γ_0 measurement of hydrogen-like tin, this results in a 2.0×10^{-11} uncertainty of the free-space cyclotron frequency.

The similar behavior of the spectra in Fig. 9.5 recorded over a time span of multiple month suggests that principally it might be possible to get a better estimate for the resonator frequency by further studying the transfer function. Nevertheless, the fitting routine would become more complex, potentially introducing other unaccounted systematics. Therefore, where higher accuracy is required, e.g. for an electron mass determination using a hydrogen-like carbon ion, a smaller dip width[8] is required, which can be achieved by selecting a different pick-up electrode with a

[7] In this context empty means that there is either no ion in the trap, or the axial frequency is detuned that there is no resonator perturbance by the ion-resonator interaction.

[8] A smaller dip width means a smaller image-current shift, and therefore less uncertainty from an inaccurate resonator frequency.

larger effective electrode distance D_{eff}, or by using a detector with a smaller parallel resistance R_{p}. A smaller dip width comes unfortunately with additional caveats. Longer averaging times are required, which may require higher axial frequency stability for both dip and peak detection. Therefore, albeit possible to reduce this systematic effect by choosing a smaller dip width, this approach is limited. To give some numbers, in the ALPHATRAP setup with hydrogen-like carbon in the PT with a Q value of about 7500, the dip width is about 0.4 Hz. This would give an axial frequency uncertainty of 4 mHz, which is a relative ν_{c} uncertainty of 4×10^{-12}, far better than any of the high-precision g-factor measurements. For even better results a phase-sensitive approach might help reduce the overall uncertainty. Achieving accurate absolute frequency measurements in the PT requires the circuitry and rigorous studies of the systematic effects, but could ultimately lead to a further reduction of the systematic uncertainty of the measurement. At the LIONTRAP experiment, initial studies of the systematic effects were carried out, which will be presented in the thesis of Olesia Bezrodnova.

9.2.5 Electromagnetic Imperfections

As introduced in the Penning-trap Chapter (Chap. 3), the imperfection of the trap can shift particle frequencies, resulting in systematic shifts that have to be optimized and characterized for highest precision. The optimization is done by a tuning ratio scan, as introduced earlier. By adjusting the correction electrode voltages, harmonicity can be improved by compensating deviations from the predicted potential due to machining and electronic imperfections. This is done by measuring the frequency shift for particles with excited magnetron radius. Repeating this for different tuning ratios enables to tune for minimal anharmonicity. It is then necessary to characterize the residual anharmonicity in the final chosen configuration to obtain limits on the systematic shift. By measuring the residual frequency shift in the trap as a function of the magnetron radius. Exemplary data for such a measurement is shown in Fig. 9.6. This is the data taken for the lithium-like ion in the optimized trap which is used in the Γ_0 measurement. The fitted values are: $C_4 < 2.9 \times 10^{-5}$ and $C_6 < 2.2 \times 10^{-3}$, which results in a relative uncertainty on Γ_0 of $< 6 \times 10^{-14}$ and $< 3 \times 10^{-18}$, respectively.

To acquire the magnetic field anharmonicity B_2 one performs the same measurement with an excited modified cyclotron radius instead of magnetron. Including the before measured C_n coefficients into its analysis provides a value for the second order magnetic field coefficient. This is possible since the C_n shift the axial frequency identically as a function of both radial radii $\hat{r}_{\pm}$. B_2 on the other hand shifts ν_{z} a factor of ν_+/ν_- more for the modified cyclotron radius $\hat{r}_+$. For all three charge states, B_2 has been determined to be less than $10\,\mathrm{mT/m^2}$. B_2 in this trap is so small for mainly two reasons:

For once, there is a CoFe ring placed around the trap stack that aims to compensate the stray field of the ferromagnetic ring in the AT[9] [108]. This was built in in the past, and reduced the stray fields by more than an order of magnitude, limited by manufacturing tolerances, placement accuracy and how similar the magnetization of the two parts is. Additionally, the electric potential in z direction is slightly shifted to move it into the inflection point of the magnetic field where B_2 is even smaller. To first order, this shift cancels, as it affects equally the Larmor frequency and the modified cyclotron frequency ν_+, in the ratio Γ_0 it therefore suppressed by a factor ν_z/ν_+ As discussed in Sec. 5.3.2, the added asymmetry in z might change odd order coefficients the first relevant odd coefficient being C_3. In the very same trap these have been studied in the past, and

[9]The material is the same for both the AT ring and the compensation ring (VACOFLUX 50). A simulation was used to find the optimal position and size to compensate the stray field (B_1 and B_2) in the PT [108].

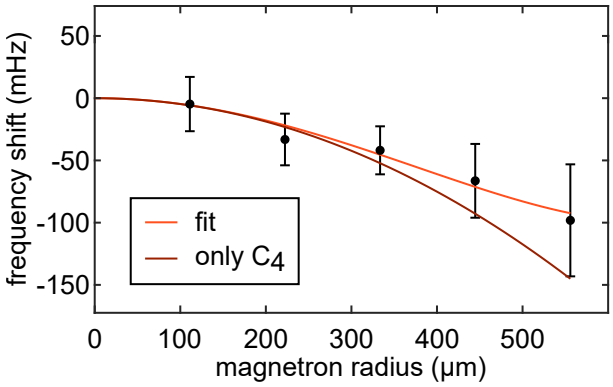

Fig. 9.6: Example data and fit of the lithium-like tin anharmonicity measurement. This data is acquired by measuring the axial frequency difference between a thermalized ion and magnetron excited ion. The errorbars are given by the uncertainty of the average at each excitation. The data seems to suggest that there might still be a residual C_4, which is used as an absolute upper limit in the systematics evaluation.

could be limited to be less than 4×10^{-3} [95]. Since the axial frequency scales identically with z^2 for C_4 and C_3^2, this would mean that in the tuning ratio optimization, the trap is optimized so that the C_4 and C_3 shift cancel each other. So $C_4 = 0$ is not achieved, but $C_4 = {}^{3C_3^2}/_{4C_2} < 2\times10^{-5}$, which is similar in size as the uncertainty of C_4 itself, which has negligible impact on the measurement (see Table 9.3). Due to the small radii, the small B_1 and C_3, the cross term $C_1 \times B_1$ has a remaining relative systematic shift to the measurement of less than 1.1×10^{-15}.

Frequency Drift

Another uncertainty to investigate is a possible drift of the axial frequency. Since this is measured only after the ν_+ measurement, a continuous drift would cause a systematic shift in the extracted ν_c. If it is due to a random drift of the axial frequency, it should average out over the whole measuring period. However, if there is a continuous drift, e.g. due to transport and the associated changes in voltage, this could potentially be problematic. Therefore, the axial frequency is measured multiple times after transporting into the PT. At first closely after transport, during the implemented settling time which is included to let the system stabilize. Then again before PnA and a final time after PnA (see the measurement scheme shown in Fig. 9.1). Since the microwave is always on in the last PnA cycle, the third axial frequency determination is much closer in time than the others. The axial frequency for the determination of the free-space cyclotron frequency is taken from a weighted mean of the two axial measurements surrounding the PnA sequence. They are weighted by the temporal proximity to the actual microwave injection. The frequency difference between these two axial dips can also be used as a measurement for the drift, from this one can assign a potential residual uncertainty on the determined axial frequency. This should be considered an upper limit, as the weighted mean accounts for a linear drift. Example data for the observed drift is shown in Fig. 9.7, as measured in the lithium-like tin g-factor run. After transport there is clear indication of a significant, several 10 mHz large drift, which was observed in all the measurements. This seems to follow either an exponential or a power law, as the difference between the last two measurements is much smaller. Fortunately, by using the weighting of the latter two dips, the first order drift is corrected. Since it is only linear in first order, there is some remaining uncertainty from the observed drifts. Thus, conservatively an error is assigned stemming from the uncertainty of the measured drift between the two axial dips. It is shown in the following error budgets for the three measured charge states, and is always smaller than 1 ppt.

One question that follows from the observed drift pattern is its origin. It was present in prior measurement in this apparatus, and thus has been studied in the past as well [94, 95]. If this were to be understood, one could potentially fix or reduce this effect, enabling to shorten the settling time, reducing the time for a single measurement cycle.

After the here presented measurement campaign it was suspected that this might be caused

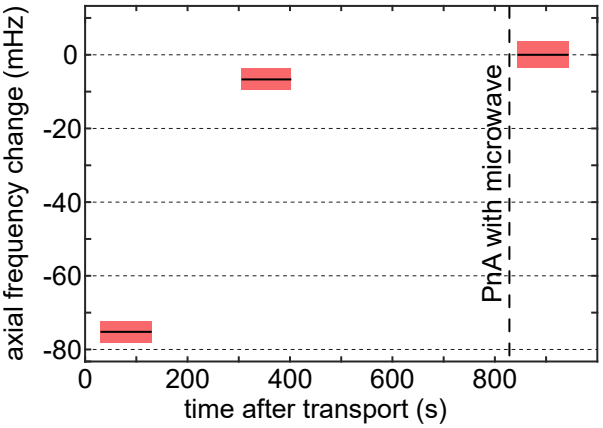

Fig. 9.7: Frequency difference between the last axial frequency measurement and the two previous ones. For each the averaging time is 100 s. The black bars are the fitted value averaged over the shown time range. The red box the frequency uncertainty, which is the standard deviation of the mean for the first two dips, and the drift corrected standard deviation of the complete g-factor measurement for the last one. Each g-factor measurement was separately analyzed. The shown data is from the lithium-like g-factor measurement.

by the *RC* filters in the DC electrode biasing wiring which are required to filter out noise. The capacitors are of type C0G (NP0), which is a class of ceramic capacitors that have low losses and small temperature coefficients. They are furthermore known to function at cryogenic temperatures without losing a significant portion of their capacitance [143].

Basically all capacitors suffer from polarization effects of the dielectric material, which is a charging effect of the dielectric material [144]. After a discharge of the capacitor, the charges stored in the dielectric are partly recovered over minute long time scales, causing a built-up of charges in the capacitor poles. In the configuration at ALPHATRAP these would therefore discharge over the *RC* filters into the DC power supplies. This current would cause a voltage drop over the resistance, which therefore shifts the voltage on the trap electrode, with the decline following a power law [144]. After changing the applied voltage during transport, it seems logically that it would cause a significant drift of the potential, and hence the axial frequency. For the used *RC* filters[10], assuming a dielectric absorption of 0.6 %[11] [145], with a 1-over-t decline of the current, this would result in large voltage drifts. E.g. after 100 s the shift would still be a few µV. Depending on the electrode in the trap stack, this can translate to frequency changes of several 10 mHz.

First results in a coldhead show that this effect is also present at cryogenic temperatures, which makes this a likely candidate to explain the observed drift behaviour. A possibility to reduce this is to chose different capacitors with smaller dielectric absorption, as in example Polypropylene, or PTFE.

9.2.6 Resonance Lineshape

In this section, the lineshape of the Γ_0 resonance is briefly discussed. There is no explicit discussion of the change in lineshape caused by the second order magnetic field inhomogeneity B_2. In the results presented, $B_2 < 10^{\mathrm{mT}}/\mathrm{m}^2$ is very small, which combined with a small thermal radius results in negligible shifts smaller than 0.001 ppt [91]. Therefore, the discussion focuses on the line shape as a result of the magnetic field jitter. In a perfect two-level system, the curve follows a Rabi transition probability with a width given by the amplitude and the irradiation length. Magnetic field instability influences this significantly. Since the transition energy is proportional to the magnetic field, its stability is of utmost importance, and changes the expected lineshape. For the weak microwave power used here, the drive looses coherence over the 5-second irradiation time, which makes the expected lineshape a Lorentzian with a maximum spin-flip probability of 50 %. Reducing the power further results in a narrowing of the resonance, up until the point that the

[10] Three filters in series with $R = 50\,\mathrm{k}\Omega$ and $C = 22\,\mathrm{nF}$

[11] Meaning that 0.6 % of the original charge retains after discharge and then slowly dissipates as soakage current.

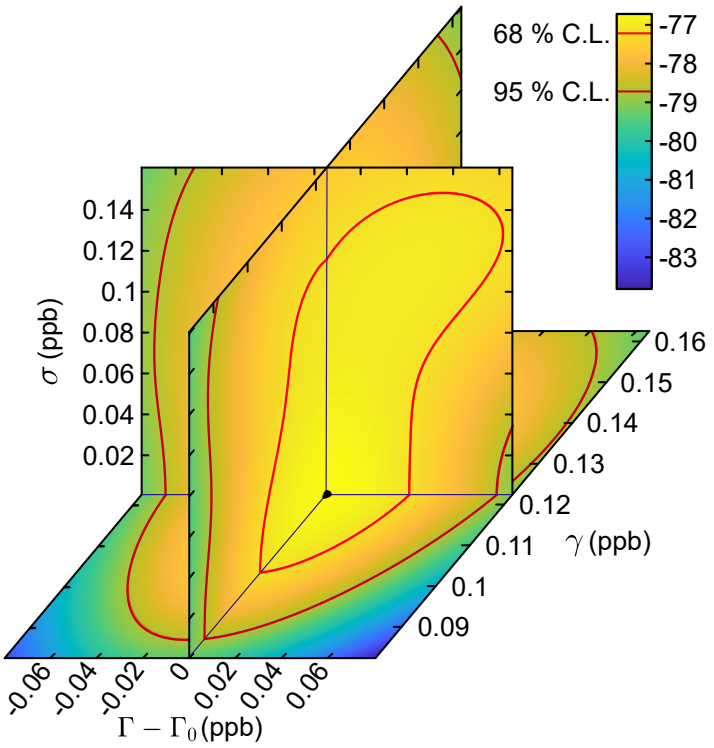

Fig. 9.8: Maximum-likelihood planes of the Voigt fit for the lithium-like Γ_0 measurement. The highest likelihood point lies in the crossing of the three planes, marked by the black dot. The light- and dark-red lines respectively mark the 1-sigma and 2-sigma likelihood surfaces. The minimum at $\sigma = 0$ suggests a power broadened resonance, which is rather unlikely given the used power and seen PnA stability in comparison to the hydrogen-like measurement. More details can be found in the text.

magnetic field instability takes over and the maximum goes below 50 %. At this point, the random walk dominated magnetic field jitter causes the lineshape to transform into a Gaussian bell.

Overall the lineshape can be described best by a Voigt function, a convolution of Gaussian and Lorentzian distributions. Therefore, the convolution of the Lorentzian

$$f_{\mathrm{Lor}}(\Gamma) = I\frac{\gamma^2}{(\Gamma-\Gamma_0)^2+\gamma^2} \tag{9.6}$$

and the Gaussian[12]

$$f_{\mathrm{Gauß}}(\Gamma) = \frac{1}{\sigma\sqrt{2\pi}}e^{-\frac{(\Gamma-\Gamma_0)^2}{2\sigma^2}} \tag{9.7}$$

is parameterized by only three missing parameters, since $I = 0.5$ follows from the two-level system. Fitting a Voigt therefore determines the magnetic field jitter in the form of σ, the Lorentzian width γ given by irradiation power and duration, along with the center of the resonance Γ_0. The problem is that in many cases the correlation between σ and γ can be quite large, making it hard to fit those reliable. The here presented resonances were all fitted with the three discussed lineshapes. In Tab. 9.1 the results are shown. The different fit results for the resonance center agrees within the statistical uncertainty for every possible lineshape. The uncertainties are similar, only some minor differences can be observed. Note that the Voigt fit of the lithium-like value is exhibiting

Tab. 9.1: Uncorrected fits of the main three resonance datasets using different lineshape models. Marked in red are the final values chosen for the determination of Γ_0.

	Hydrogen-like	Lithium-like	Boron-like
Lorentzian	4189.05824247(17)	4526.89426647(12)	1539.24204262(37)
Gaussian	4189.05824237(16)	4526.89426668(20)	1539.24204260(42)
Voigt	4189.05824239(17)	4526.89426658(17)	1539.24204260(37)

[12] Which must conserve the area under the curve due to the quantum mechanical processes and the random drift behavior of the magnetic field. Therefore it is convoluted with the normalization factor $\frac{1}{\sigma\sqrt{2\pi}}$

correlation between the parameters. According to the (voigt) fit results, shown with the maximum-likelihood planes in Fig. 9.8, the Gaussian jitter σ seems to be zero, making it a pure Lorentzian shape. This is very unlikely to be the case, as this would mean the magnetic field stability during this specific run was significantly better than ever seen. This would be even more surprising, as the phase stability was not particularly different in this run. Therefore, even for this, considering that the width is pretty identical to the hydrogen-like measurement, the Gaussian fit still seems to be more suitable. Furthermore both fits show agreement in the extracted value of the center. Using the Gaussian with the higher uncertainty is therefore the more conservative choice. In the end, for simplicity reasons, either a Lorentzian or a Gaussian curve was chosen for the final results, even though those might often not be the one with the largest error. This is justified, as for once the difference in uncertainty is near negligible, while also from the overall width, and the chosen microwave power, one line shape is clearly favorable due to the set power and spin-flip probability in the center. For a better differentiation, significantly more data points would be needed, which would take extensive time, as the cycle time here is ca. 20 min.

9.3 g Factor of ...

The following sections summarize the results of the measurements for the three individual charge states. The used sequence is described previously. In the following the differences between the measurements are pointed out. First an overview table summarizing the relevant parameters of the measurements for each is shown in Tab. 9.2. In Tab. 9.3 the three results and the systematic corrections are shown for each. A discussion about the comparison with the theoretical prediction follows in Chapter 11.

Note that for hydrogen-like and lithium-like tin, additional resonances were recorded. These were either used for testing of systematic effects (see Sec. 9.2.2), or were part of the microwave power optimization to get a non-saturated resonance. Here, the focus will lie on the final, and therefore most precise measurement of each.

Tab. 9.2: Values and limits of important parameters in the recorded main resonances for hydrogen-like, lithium-like and boron-like tin. Parameters that are shown in the middle are identical in all three measurements. Details can be found in the text.

Parameter	Hydrogen-like	Lithium-like	Boron-like
Precision Trap:			
Ring voltage V_0	-58.975 V	-61.410 V	-64.139 V
ν_-	8 267 Hz	8 619 Hz	9 003 Hz
ν_z		651.5 kHz	
ν_+	25.672 MHz	24.623 MHz	23.575 MHz
ν_c	25.680 MHz	24.632 MHz	23.584 MHz
ν_L	107.578 GHz	111.508 GHz	36.301 GHz
$\lvert C_3\rvert$		4×10^{-3}	
$\lvert C_4\rvert$	$< 1.9 \times 10^{-5}$	$< 2.9 \times 10^{-5}$	$< 1.2 \times 10^{-4}$
$\lvert C_6\rvert$	$< 7.5 \times 10^{-3}$	$< 2.2 \times 10^{-3}$	$< 1.3 \times 10^{-2}$
B_1		2.64(3) $^{\mathrm{mT}}/_{\mathrm{m}}$	
$\lvert B_2\rvert$		$< 10\ ^{\mathrm{mT}}/_{\mathrm{m}^2}$	
Temperature T_z	5.4(3) K	5.5(2) K	6.3(3) K
PnA settings:			
Excitation pulse	30 ms@0.2 V	30 ms@0.2 V	30 ms@0.2 V
Coupling pulse	500 ms@9.9 V	500 ms@9.9 V	500 ms@9.9 V
Radius	12.8(1.3) µm	12.8(1.3) µm	12.1(1.3) µm
t_{ref}		0.2 s	
t_{unwrap}		0.5 s, 2.2 s	
t_{long}		5.2 s	
PnA results:			
phase jitter at t_{ref}	5.6°	6.3°	5.8°
phase jitter at t_{long}	10.1°	11.3°	8.4°
SNR	23.7 dB	20.7 dB	21.5 dB
Relative PnA jitter	2.1×10^{-10}	2.4×10^{-10}	1.8×10^{-10}
Analysis Trap:			
Ring voltage V_0	-1.333 V	-1.390 V	-1.451 V
ν_z		341 kHz	
ν_L	103.412 GHz	107.189 GHz	34.895 GHz
$\lvert B_2\rvert$		42.77 $^{\mathrm{kT}}/_{\mathrm{m}^2}$	
$\Delta\nu_z$ (spin flip)	311 mHz	322 mHz	105 mHz
t_{evol}	0.88 s	0.88 s	3.02 s
ν_z jitter	22 mHz	24 mHz	13.4 mHz

Tab. 9.3: Error budgets of the three Γ_0 and g-factor measurements. [a] refers to the old CODATA 2018 value of the electron mass [138]. [b] is that of the newly published 2022 value that includes the measurements via HD^+ which slightly shift the value [146]. The old value is presented here to stay consistent to the values published in [54, 64]. Details can be found in the text.

	Γ_0 **error budget**					
	$^{118}Sn^{49+}$		$^{118}Sn^{47+}$		$^{118}Sn^{45+}$	
Uncorrected Γ_{stat}	4 189.058 242 37(16)		4 526.894 266 68(20)		1 539.242 042 61(37)	
	Relative shift (ppt)	Uncertainty (ppt)	Relative shift (ppt)	Uncertainty (ppt)	Relative shift (ppt)	Uncertainty (ppt)
residual C_4 shift	-	<0.04	-	<0.06	-	<0.3
residual C_6 shift	-	<0.000 02	-	<0.000 003	-	<0.000 3
ν_z drift	< 0.05	<0.3	< 1	<0.4	< 0.6	<0.6
ν_- measurement	-	3.8	-	4.3	-	4.9
Relativistic shift [96]	23.7	4.8	21.8	4.4	20.0	4.0
Image-charge shift [93]	148	7.5	148	7.5	148	7.5
ν_z line shape	-	20	-	22	-	22
Total systematic uncertainty	-	22	-	24	-	24
Statistical uncertainty	-	38	-	42	-	240
Total Γ_0 uncertainty		44		48		241
Corrected Γ_0	$4\,189.058\,241\,643(160)_{stat}(93)_{sys}$		$4\,526.894\,265\,905(191)_{stat}(107)_{sys}$		$1\,539.242\,042\,354(370)_{stat}(37)_{sys}$	
	External parameters and g error budget					
m_e [a]	$5.485\,799\,090\,65(16) \times 10^{-4}$ u					
m_e [b]	$5.485\,799\,090\,44(10) \times 10^{-4}$ u					
mass M	117.874 869 069(56) u		117.875 920 534(56) u		117.877 000 632(56) u	
g factor [a]	$1.910\,562\,058\,962(73)_{stat}(42)_{sys}(910)_{ext}$		$1.980\,354\,799\,750(84)_{stat}(47)_{sys}(944)_{ext}$		$0.644\,703\,826\,518(155)_{stat}(16)_{sys}(308)_{ext}$	
g factor [b]	$1.910\,562\,058\,889(73)_{stat}(42)_{sys}(909)_{ext}$		$1.980\,354\,799\,675(84)_{stat}(47)_{sys}(943)_{ext}$		$0.644\,703\,826\,493(155)_{stat}(16)_{sys}(307)_{ext}$	

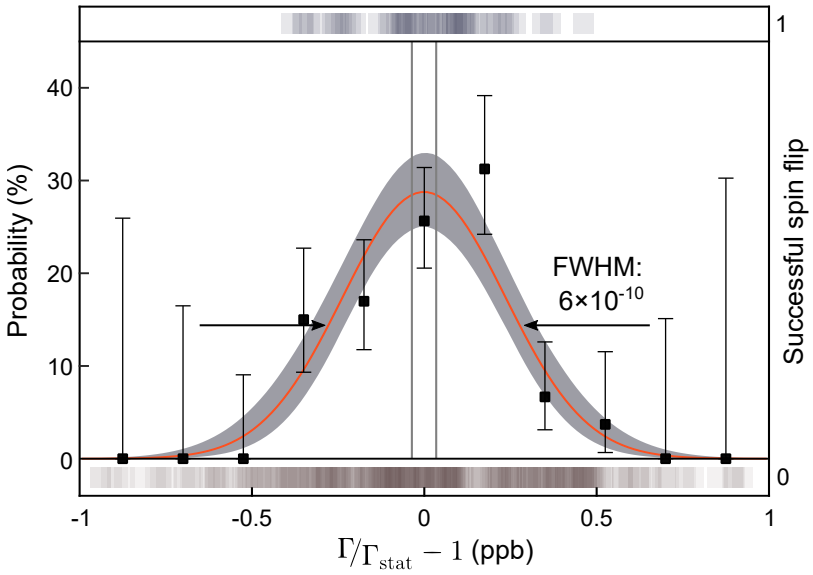

Fig. 9.9: Measured Γ_0 resonance of hydrogen-like tin. The squares above and below are the individual successful and unsuccessful data points. The black points are an arbitrarily binned set of this data. This binned set is for visualization purposes only. The red line is the fitted curve, surrounded by the 1-σ confidence interval in gray. The figure is adapted from [54]. More details can be found in the text.

9.3.1 ... Hydrogen-like Tin

The measurements with the hydrogen-like tin ion took the most time. This ion was used to write reliable measurement programs that perform the measurement sequences and takes care of readable and extensive data-acquisition for rigorous analysis. These programs built upon prior work by former members of the ALPHATRAP team, but are further developed towards a more object oriented style, with more focus on frequent and abundant saving of workspace variables and code for better tracking of taken data and the code that ran to measure said data. This ion was also used to test the system, as well as the code and various systematic effects. For the final resonance, the power of the microwave was determined for a non-saturated resonance, and Γ_0 of hydrogen-like tin was measured. The programs written for this ion were then later used for the measurements of the other two charge states.

The hydrogen-like Γ_0 resonance probed in total 387 Γ values. In 54 of these the PT microwave flipped the spin. The maximum-likelihood analysis using a Gaussian fit function, as discussed earlier, has a relative precision of 38 ppt on the resonance center. The FWHM of the resonance is 0.56(3) ppb (relative to Γ_0), and the amplitude is 29(4) %. Thus, the line splitting is roughly 7 %. The measured statistical center is extracted as:

$$\Gamma_{\text{stat}}\left(^{118}\text{Sn}^{49+}\right) = 4\,189.058\,242\,37(16). \tag{9.8}$$

Correcting this for the statistically relevant systematic shifts, the relativistic correction and the ICS, gives a final value

$$\Gamma_0\left(^{118}\text{Sn}^{49+}\right) = 4\,189.058\,241\,643(160)_{\text{stat}}(93)_{\text{sys}}. \tag{9.9}$$

The summary table of all the different systematic effects that are knownis given in Tab. 9.3. Putting this into the equation for the g factor results in an experimentally determined value of:

$$g\left(^{118}\text{Sn}^{49+}\right) = 1.910\,562\,058\,962(73)_{\text{stat}}(42)_{\text{sys}}(910)_{\text{ext}}. \tag{9.10}$$

Note that this is using the CODATA 2018 value for the electron mass [138]. This is used to stay consistent with the earlier publication [54]. In Tab. 9.3, the value for the newer CODATA 2022 value is included as well.

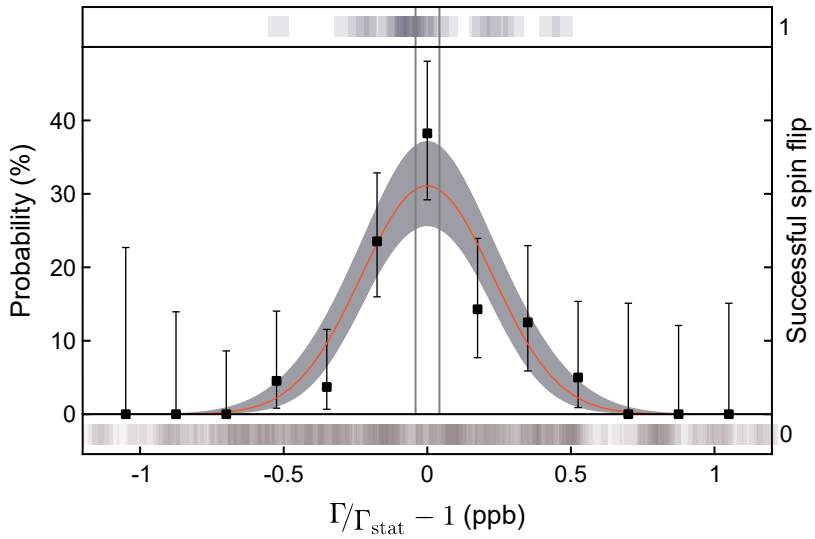

Fig. 9.10: Measured Γ_0 resonance of lithium-like tin. The squares above and below are the individual successful and unsuccessful data points. The black points are an arbitrarily binned set of this data. This binned set is for visualization purposes only. The red line is the fitted curve, surrounded by the 1-σ confidence interval in gray. The figure is adapted from [64]. More details can be found in the text.

9.3.2 ... Lithium-like Tin

The measurement procedure for lithium-like tin is very similar to that of the hydrogen-like measurement. Apart from adjusting parameters like the trap voltages and frequencies, not much had to be changed in the measurement script. Systematic effects are studied similarly, by measuring the electromagnetic trap imperfections and the excitation radius during PnA. In the end, the final resonance includes 330 points with 31 successful PT spin flips. The statistical precision on the center is 42 ppt, and the FWHM is determined as 0.54(3) ppb. 31(6) % is the extracted value for the amplitude. The statistical center is extracted as

$$\Gamma_{\mathrm{stat}}\left({}^{118}\mathrm{Sn}^{47+}\right) = 4\,526.894\,266\,68(20). \tag{9.11}$$

Corrected for the two dominant systematic effects, Γ_0 is extracted as:

$$\Gamma_0\left({}^{118}\mathrm{Sn}^{47+}\right) = 4\,526.894\,265\,905(191)_{\mathrm{stat}}(107)_{\mathrm{sys}}. \tag{9.12}$$

Putting this into Eq. (3.3), along with the mass values and the charge ratio of $q/e = 47$, results in a g factor for the lithium-like tin ion of

$$g\left({}^{118}\mathrm{Sn}^{47+}\right) = 1.980\,354\,799\,750(84)_{\mathrm{stat}}(47)_{\mathrm{sys}}(944)_{\mathrm{ext}}. \tag{9.13}$$

As for the hydrogen-like value this is using the 2018 value for the mass of the electron. The g factor with the CODATA 2022 value, as published in Ref. [64], is:

$$g\left({}^{118}\mathrm{Sn}^{47+}\right) = 1.980\,354\,799\,675(84)_{\mathrm{stat}}(47)_{\mathrm{sys}}(943)_{\mathrm{ext}}. \tag{9.14}$$

9.3.3 ... Boron-like Tin

Overall, the boron-like measurement run was slightly different compared to the other two. Most notably, the Larmor frequency is about a factor of 3 smaller, requiring a change of the microwave setup. The frequency tripler, needed for the more than 100 GHz larmor frequencies ν_{L} of the s-shell g factors, was removed and replaced by a frequency doubler[13] followed by a simple microwave

[13] Note that the *Anritsu* microwave generator can directly supply the microwave frequencies needed for the Larmor frequency of boron-like tin, but the frequency doubler has a higher output power, which helped finding the resonance frequency as the larger power further broadens the linewidth.

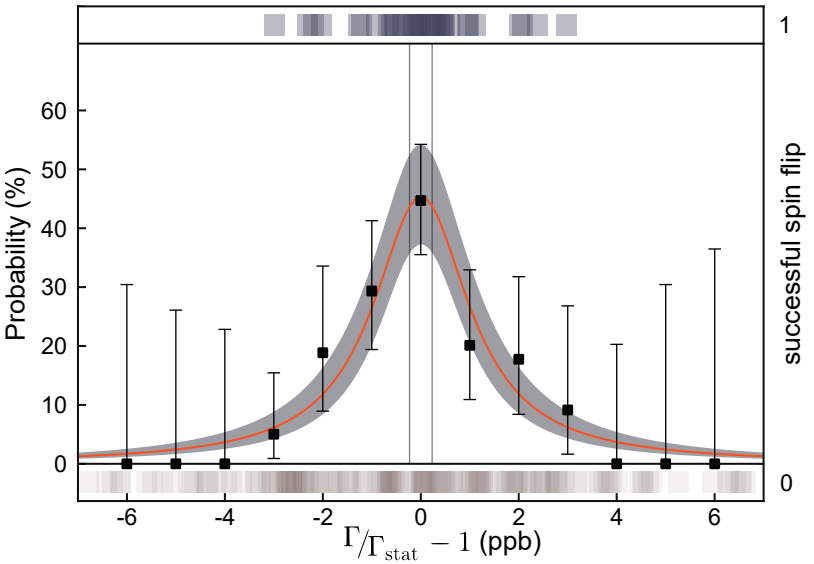

Fig. 9.11: Measured Γ_0 resonance of boron-like tin. The squares above and below are the individual successful and unsuccessful data points. The black points are an arbitrarily binned set of this data. This binned set is for visualization purposes only. The red line is the fitted curve, surrounded by the 1-σ confidence interval in gray. The figure is adapted from [72]. More details can be found in the text.

launcher to switch from the coaxial cable to a rectangular waveguide.

Also because of the reduced Larmor frequency, the spin flip in the AT is about a factor of three smaller, so the free evolution time for the spin-flip detection was adjusted to 3.02 seconds, which resulted in a phase shift of around 115° for a spin change. The PnA parameters stayed the same, as well as the trap parameters. Similar to the others, the anharmonicity was measured, but with a smaller sample size and therefore not as precisely, as can be seen in Tab. 9.2.

Another specialty of the g-factor measurement of boron-like tin was that no theory value available at the time of the measurement. This required to extrapolate from theoretical values of nearby elements, which in themselves had uncertainties in the parts-per-million range [62, 147]. Thus, the range which would have to be tested to find the Larmor frequency in the PT was at least in the 10^{-5} range. Another uncertainty is the width of the resonance at maximum output power of the microwave generator, this might be rather small requiring a small step size in order to not miss the resonance in the search. With these difficulties the search for Γ_0 took a few days.

Furthermore the remaining time to perform the measurement was short since the start of the following HD^+ campaign was imminent. Therefore only a saturated resonance was recorded, as there was no time to optimize the microwave power. Overall, 195 Γ ratios were probed, of these 35 were successful PT spin flips. The resonance is saturated as can be seen in Fig. 9.11. As discussed in the line shape section, a Lorentzian curve was used.

The statistical accuracy is 240 ppt, and the height is fitted as 45(8) %, and the FWHM is extracted as 2.4(3) ppb. Corrected for relativistic and ICS Γ_0 is extracted as

$$\Gamma_0^{\text{B-like}} = 1\,539.242\,042\,354(370)_{\text{stat}}(37)_{\text{sys}}. \tag{9.15}$$

As with the other charge states, the g factor is extracted as

$$g^{\text{B-like}} = 0.644\,703\,826\,518(155)_{\text{stat}}(16)_{\text{sys}}(308)_{\text{ext}}, \tag{9.16}$$

using the CODATA 2018 electron mass value to stay consistent. The g factor with the newer value can be found in Tab. 9.3. Since the dataset consists of less points, and the resonance is much wider, the precision is significantly worse than for the other charge states. Nonetheless, the limiting factor is still the mass, and if there ever is a need, the measurement can easily be redone, as production of boron-like systems is much easier with their lower binding energy, and optimization of the power can also be done as shown with the measurements of the other two charge states.

Chapter 10

Outlook

This chapter will cover various topics that will be of interest for future measurements performed at ALPHATRAP. It starts with the description of the high-voltage upgrades for the Hyper-EBIT. It is intended that this setup will eventually produce hydrogen-like atoms up to uranium with $Z = 92$. The chapter further covers some upgrades that were implemented after the tin measurement campaign. This includes a mechanical capacitor, which can be actuated at 4 K using a Bowden wire connected to a mechanical feedthrough. Also, first results of a superconducting cylindrical shield are presented, which is aimed to improve the magnetic field stability by screening the trap from external magnetic field changes. First measurements were performed with this to test the magnetic field stability. Lastly, a new trap design is introduced that incorporates a different manufacturing technique for the cylindrical electrodes. Instead of using copper electrodes stacked and isolated via sapphire rings, a monolithic fused silica design is suggested. This would use a selective laser etching [148] process to shape the trap. A trap with a similar manufacturing approach is currently being designed by Paul Holzenkamp for the LSym experiment (ERC grant ID: 101097850).

10.1 Hyper-EBIT

The Hyper-EBIT was designed to be a successor of the HD-EBIT enabling higher acceleration potentials, and hence more versatile charge state preparation. This includes larger distances in vacuum for high-voltage carrying components. While the HD-EBIT relies on a cryostat filled with liquid helium to cool the superconducting magnet, the Hyper-EBIT magnet is attached to a coldhead, enabling continuous operation for long times without ramping of the magnetic field coils to refill liquid helium[1].

The design goal of the Hyper-EBIT, to achieve arbitrary charge state preparation, is set high with an acceleration potential of 300 kV at half an ampere of electron beam current. If these goals are met, production of bare uranium with a $1s$ binding energy of ca. 130 kV should be possible, as demonstrated in the Super-EBIT with less than 200 keV of beam energy [51].

The setup is briefly introduced followed by the presentation of the required upgrades for the high-voltage operation. Since lots of information on this EBIT is broadly available, the introduction is kept short and it is referred to prior work for more in depth description, i.e. in Ref. [102, 105].

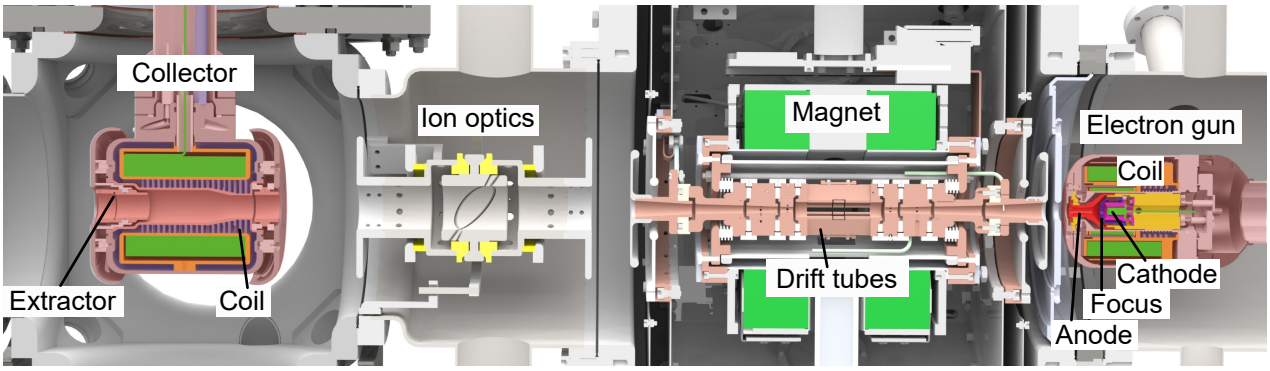

Fig. 10.1: Cut view of the inner components of the Hyper-EBIT. Parts shaded in red are those that are isolated from the rest of the apparatus, in order to bias them to several 100 kV. The configuration is similar to the sketch shown in Fig. 4.1. The electrons are emitted from the cathode and accelerated towards the anode and the drift tubes, where they are compressed in the magnetic field. In the trap region, the beam diameter is compressed to a few 10 µm, as described in Eq. (4.2). Eventually several components here will be replaced, for once, the drift tubes will be exchanged for the updated version used in the CANREB EBIT. The Sikler lens between the magnet and the collector is likely to be replaced by a smaller version to increase the safety distance to the high voltage on the collector.

Setup

The EBIT was built a bit more than 10 years ago, the setup is described in ample detail in the thesis of Thomas Baumann, who designed and built the EBIT in the group of José Crespo [105]. Back then, the EBIT was connected to the CryPTEx experiment, which worked on laser spectroscopy of HCI in a Paul trap [149]. As introduced above, the Hyper-EBIT is set up around a commercial superconducting magnet from *Cryomagnetics, Inc.* It is attached to a cryogenic coldhead for low-maintenance operation. The magnet supports magnetic fields up to 7 T to give a strong electron beam compression, which is important for a high current density and therefore for efficient ionization (see Eq. (4.2)). Fig. 4.1 in Chapter 4 is a simplified sketch of the inner components that are also found in the Hyper-EBIT. As standard for the high-power EBITs[2], the electron gun and the collector are separated from the laboratory ground, and can be biased with a high-voltage power supply [53, 150–153]. While this was considered in the original design of the Hyper-EBIT, the necessary upgrades were never fully designed or implemented. Thus, for high-voltage operation only few modifications are necessary. Rather additional components, to enable the intended use of the core setup, have to be designed and finished. The current setup of the inner components is shown in Fig. 10.1. On the right, the head of the electron gun is close to the superconducting magnet, within the gradient of its magnetic field. The vacuum chamber itself is incorporating four isolators, separating the vacuum enclosure of the electron gun from the main housing of the magnet and other components which are connected to the common ground, as is shown in Fig. 10.2 which shows the intended high-voltage upgrades for the EBIT. The isolators are rated to 50 kV of potential difference each, but were tested with up to 75 kV without any sign of electrical breakdown. Thus, four isolators should be able to hold the desired voltage difference of 300 kV. To further ensure this, a fifth will be installed during the implementation of the upgrades.

The electron gun can be moved in vacuum with an xyz-manipulator. This is on the high-voltage side of the isolators, and connects to the electron gun with a tube towards the magnet, as shown in Fig. 10.2. At its end, the head of the electron gun is connected. The feedthroughs for the gun

[1] Note that this is not typical for superconducting magnets. Usually the cryostats can be refilled during operation, but this led to problems in the past with the HD-EBIT, so the current in the magnet is ramped down during filling operation.

[2] In this context high power refers to a large acceleration potential for the electron beam.

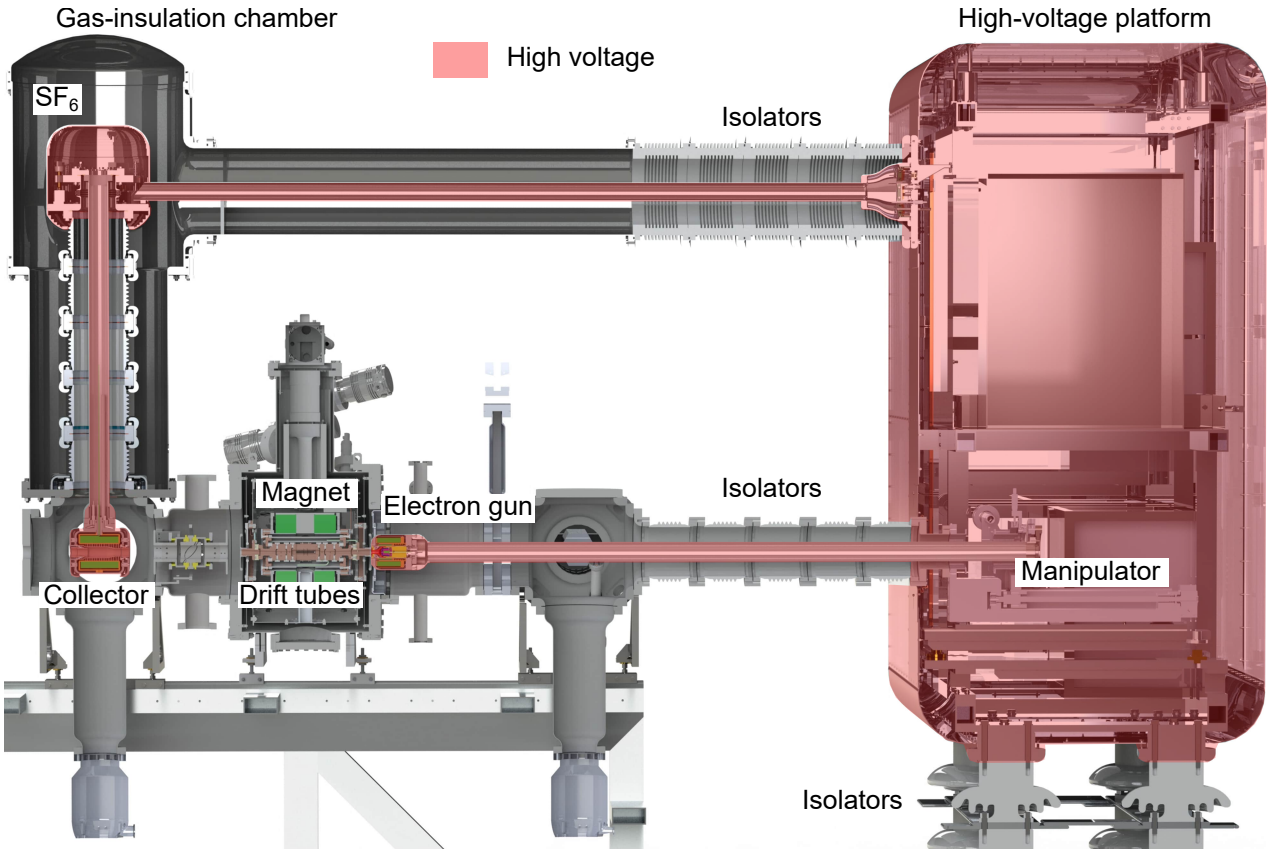

Fig. 10.2: Upgraded Hyper-EBIT setup including the high-voltage platform and the gas-insulation chamber that are currently being manufactured. Highlighted in red are the parts that will be isolated from ground, enabling to bias them to a few hundred kilovolt.

electrodes are at the end of this tube where the gun head starts. Within the vacuum, the long tube is supported by two 45 ° ceramic rods, which can be adjusted in length via linear mechanical feedthroughs for additional degrees of freedom in the gun positioning.

The collector is similarly isolated from the rest of the vacuum chamber. As shown in Fig. 10.2, the collector will also be upgraded with an additional ceramic isolator. The collector is suspended from a steel tube containing the cooling water pipes and the cables that connect to the electrical feedthroughs.

Within the superconducting magnet, the drift tubes are placed. Nine electrodes separated by ceramics are used to set the confining potential for the ions in axial direction. Within the center electrode, the charge breeding takes place. Vertically through some holes in the superconducting magnet, neutral atoms can be injected into the EBIT to feed the trap with atoms to ionize. Between the collector and the drift tubes, the EBIT also incorporates an ion-optical lens, to help transport ions out of the trap [105].

To reach the design goals there are various components that must be changed, and some that can be changed to further optimize the conditions for high-voltage operation. While the inner setup of the EBIT is set up for this, the supporting infrastructure must be modified to enable biasing of the high-voltage components, starting with the laboratory.

High-Voltage Laboratory

The EBIT was last operated in 2018, when it was used to produce boron-like argon for the CryPTEx experiment. High-voltage operation is not possible in the CryPTEx laboratory where the EBIT

was originally located. It will eventually replace the HD-EBIT to connect it to the beamline to ALPHATRAP. But since the HD-EBIT is still in use, the Hyper-EBIT can only be moved once it demonstrates to be an improvement over the predecessor. Therefore, to perform the necessary changes for operation with up to 300 keV of beam energy, a new laboratory was set up by the Technicians from the Christian Kaiser Workshop at the Max-Planck-Insitut für Kernphysik.

To enable the operation with lots of high-voltage carrying components, the laboratory housing is made completely from metal, with the walls and ceiling being supported by aluminum profile. With a size of 6 m × 8 m × 6 m (width × length × height) large distances for high-voltage carrying components are planned to increase the electrical breakdown voltage. The walls, floor and ceiling are covered on the inside with 1 m × 1 m aluminum sheet panels, fully enclosing the room, acting as a Faraday cage. After it was relocated to the new laboratory, checks were performed to determine the condition of the EBIT.

Recommissioning

This included a test run at low beam energies to see whether the essential components are functioning as intended. This is documented in detail in the bachelor thesis of Simon Heidrich [102]. In summary, this was overall successful with the EBIT performing as intended. Production of highly charged argon and krypton was demonstrated, limited only by the acceleration potential which can not be further increased until the high-voltage upgrades are implemented.

For further details on the recommissioning it is referred to Ref. [102]. Here the focus will be on the required upgrades to achieve hundreds of kV of acceleration potential. For this the next major step is to complete the separation of the ground of the electron gun and the collector which is required to bias both to several -100 kV. The two major missing components for this are a high-voltage platform, and a gas-insulation chamber surrounding the collector, which are presented here.

10.1.1 High-Voltage Platform

On the high-voltage platform, the necessary devices to operate the gun and the collector are located. It is electrically separated from the common laboratory ground by a set of isolators rated for the required voltage difference. The isolators used for this platform were taken from an old setup with a similar purpose. Fig. 10.3 shows a CAD model of the platform. The platform itself consists of a welded aluminum frame, which rests on the insulators below. The frame is surrounded by a hull made from aluminum plates and curved edges/corners, which provides a flat surface for smooth potential curves which avoid electrical breakdown originating from sharp corners. Located on the platform are a set of 19-inch racks, providing space for the required hardware to operate the gun and the collector electrodes. Also on the table is the gun manipulator. With an adjustable table it can be aligned relative to the rest of the EBIT. This helps to reduce the mechanical stress of the setup. Otherwise, with the long lever, the vacuum isolators could break, causing failure of the machine.

On the upper part of the frame, additionally to the 19-inch racks, a water chiller is located. This removes excess heat from the gun and the collector. In the gun it cools the bucking coil, which is required to null the magnetic field at the cathode. In the collector it removes the heat generated by the electrons colliding with the electron collector. The residual kinetic energy of the electrons at impact comes from the potential difference between the cathode and the collector, which is typically set to voltages up to -3 kV, which means for a typical electron beam current of up to 500 mA, the beam will dump about 1.5 kW as heat into the collector. Within the chiller, the

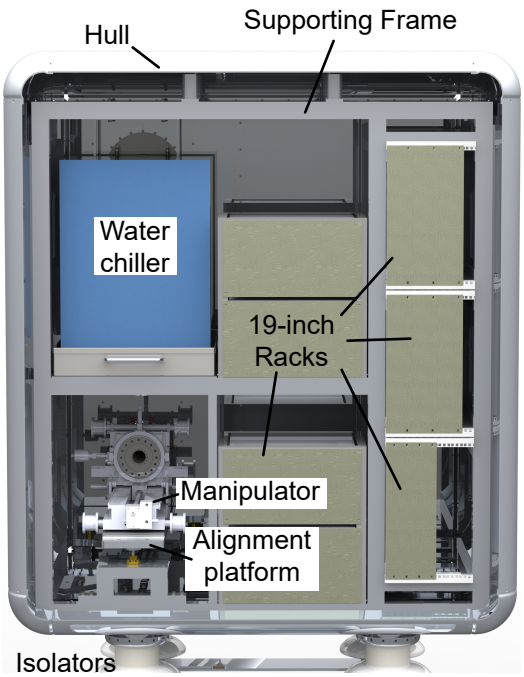

Fig. 10.3: Front view of the high-voltage platform. The front hull is cut open to show the inside of the platform. In the bottom left, the alignment table is located, on which the manipulator for the electron gun rests. Above it is the water chiller which cools both the collector and the electron gun. The rest of the platform includes 19-inch racks which will support all the power supplies and control devices required for the operation of the electron gun and the collector.

heat is transferred to the air with a heat exchanger. This comparably compact solution enables operation on top of the high-voltage platform. No liquid coolant must be transferred between the platform and the laboratory, which is difficult due to the large potential difference. The only requirement is sufficient air flow through the platform to transfer the heat into the room, which will be ensured by a grid of holes within the top and the bottom of the hull with the option to add fans to increase the air flow if required.

Power Requirements

Since the gun platform will be completely isolated the power to operate the components on the platform must be transferred onto the platform without electrical contact to the laboratory ground. To do this, two approaches are considered here, but no decision has been made yet. The simplest solution, albeit expensive is the use of an isolation transformer. The requirements for this are an electrical isolation of up 300 kV, while transferring a power of 5 kW to 10 kW[3]. It is possible to buy transformers with these specifications. The company *Guth* (which now belongs to *XP Power*) built one for the Max-Planck-Institut für Kernphysik which is currently being used for similar purposes in the cryogenic storage ring CSR [154].

The alternative approach is the use of a motor in combination with a generator. Such a setup is in use at the HD-EBIT, where an asynchronous 3-phased motor is driving an identical motor via an insulating drive shaft, which here acts as a generator on top of the high-voltage platform. Due to the configuration of the generator it produces a star-configured output. The 3×230 V are used to power the devices on the platform.

A low impedance to a common ground for all the components on the platform must be ensured. For once it connects to the neutral conductor of the generator and to the output of the high-voltage power supply which biases the complete platform to the required voltage. Furthermore, the whole frame and the outside hull must be connected with low impedance too. This ensures that, in case of electrical breakdown, the energy can discharge quickly and without large voltage differences within the platform and between the various devices, protecting the equipment from failure.

[3]This is an upper estimate of the total power consumed by all components located on the platform.

10.1.2 Gas-Insulation Chamber

The second component that is currently in the manufacturing stage, is a gas-insulation chamber. This is required for the connection between the high-voltage platform and the collector since both sides need to be biased to the same voltage as explained in Chapter 4. The collector, the tube and the vacuum assembly on top of the isolators is biased to the voltage of the electron gun. To ensure a high breakdown voltage, they will be enclosed by a gas-insulation chamber as shown in Fig. 10.2. In there, the minimum distance between any two points with a high potential difference is 10 cm, to ensure a high breakdown voltage. To ensure this, the chamber has an inner diameter of 50 cm at the upper section. At the top the chamber will continue horizontally towards the high-voltage platform. The outer diameter of the horizontal section is 25 cm, centered within is an additional steel tube with 5 cm diameter. Within the 5 cm tube, the cables and the hoses transporting the cooling water are located. The electrical connections into the gas-insulation chamber are done via commercial vacuum feedthroughs at the end flange of the vertical section within the high-voltage platform. The water is let through via steel tubes tubes which are welded into the flange. Since the flange is connected to the high-voltage platform, and is therefore biased to high voltage, it must be isolated from the rest of the gas-insulation chamber. To achieve this, five custom isolators made from high-density polyethylene are placed within the vertical section, as can be seen Fig. 10.2. While the end flange of the gas-insulation chamber is fixed to the platform, the manipulator is not fixed to the platform to avoid problems from the manufacturing tolerances.

The gas-insulation chamber is supposed to be filled with suitable gas to increase the breakdown voltage. According to the Paschen-law [155], at ambient pressure and distances above a few centimeters, the breakdown voltage increases with a higher *pressure*× *distance* product. The chamber is designed to withstand gauge pressures up to 0.5 bar. The gas used for isolation is not decided yet, as multiple options exist, and a later exchange can be done without a modification of the setup. The first tests would be done with pure nitrogen, which is already a significantly better insulator than than ambient air, due to the dry conditions in the chamber [156]. Furthermore, at 1.5 bar and 10 cm clearance it should withstand voltage differences up to 400 kV [157, 158].

If it is required to further increase the breakdown voltage, SF_6 could be an alternative, which has a factor four higher breakdown voltage [158]. Nonetheless as a far more potent green-house gas than CO_2 [159], SF_6 should be used with care and the proper equipment to avoid leakage.

To further reduce the risk of breakdown, sharp corners are avoided on the inside, and the flanges of the isolators are covered with flat metal covers to shield the sharp edges of the bolts and nuts. Furthermore, all surfaces are electropolished for a smooth surface finish.

Next Steps

Both the gas-insulation chamber and the high-voltage platform are currently being manufactured by the workshop at the Max-Planck-Institut für Kernphysik. Apart from these two, further upgrades and changes are planned to improve the EBIT for the hydrogen-like ion production. This includes a rework of the drift-tube setup, which is supposed to be exchanged for the updated version used in the *sister* EBIT, the CANREB EBIT [153]. Furthermore, to reduce the risk of breaking the superconducting magnet, slight modifications are necessary to better protect it for the case of in-vacuum high-voltage breakdown. The place with the highest risk of high-voltage breakdown is between the electron gun and the front electrode of the drift-tube setup as here the distance is the smallest. To enable safe discharge in case of a breakdown, implementation of a thick plate, connected to the laboratory ground, is planned. It will be directly connected to the vacuum chamber, and act as a barrier between the gun section and the magnet section. At the

collector, the plan is to use a similar approach, although due to the higher distances the safety constraints are relaxed. Along with a proper interlock system for the safety of people and equipment, these upgrades will then allow first tests of the high-voltage capabilities of the EBIT, which will at first be performed without an electron beam. Eventually both can be combined, and first production of heavy HCI can be demonstrated. Successful production can be shown either via an X-ray detector, which was implemented in the Hyper-EBIT setup before [102], or by ejection and q/M separation followed by a multi-channel plate and a phosphor screen for ion detection. This was also successfully shown for light ions with the Hyper-EBIT setup by Luca Geißler, who is about to submit his bachelor thesis on this topic.

10.2 Largely Tunable Mechanical Varactor

As introduced in Sec. 3.3, cyclotron detectors can be used for direct thermalization of the cyclotron mode by coupling the induced image-charges to a resonator circuit. Differently, sideband cooling with an axial resonator can only cool the mode to a temperature $T_+ = T_z \, \nu_+/\nu_z$ (see Sec. 3.3), while direct cooling of the modified cyclotron mode provides thermalization to 4 K. A major disadvantage of cyclotron detectors is that while the axial frequency of the ion can easily be tuned by adjusting the trap voltages, the cyclotron frequency depends mostly on the magnetic field, which is essentially fixed. Thus, a modified cyclotron detector is typically designed for a specific q/M range.

Here the design for a largely tunable mechanical varactor (LTMV) is presented. It is placed electrically parallel to the cyclotron resonator. With the LTMV, the total capacity of the LC circuit can be changed, enabling to tune the oscillation frequency given by $\omega_{\mathrm{res}} = 1/\sqrt{LC}$. Far tuning is useful as one detector can be used for a multitude of ions without the need to replace/modify the resonator. The design consists of three stacked printed circuit boards (PCB), shown in Fig. 10.4. The top and bottom PCB are fixed, the middle PCB is hooked to a Bowden cable, and slides between the two top and bottom PCBs. In each PCB the top and bottom copper layers are connected by vias. Depending on the position of the Bowden cable, the overlap of the copper layers on the PCB is varied, changing the capacitance between the two. To avoid electrical contact between the two poles, polyimide[4] tape is used in between. This has a dielectric constant of around 3.4, further increasing the capacitance per overlapping area. In total, the design has four opposing copper plates of which the overlap is changed by the Bowden cable. Fully inserted the total overlapping area is $4 \times 7 \times 14\,\mathrm{mm}^2$. The Bowden cable is connected to a mechanical feedthrough at the vacuum enclosure. The cable is made of titanium and is enclosed by a PTFE tube which is fixed close to the linear feedthrough and to the frame of the LTMV. Additional thermal load from the Bowden setup is small since the titanium and PTFE are poor thermal conductors. With this design, the capacity changes roughly linearly[5] with the extrusion length of the titanium wire at the LTMV. With a tape thickness of around 100 µm, the maximum capacitance should theoretically reach values up to 120 pF. Testing the design showed upper values between 40 pF and 100 pF, depending on the tightness of the assembly.

One thing to consider is the thermal shrinking of the material when cooling to liquid helium temperatures. The PCB shrinks significantly more than the metal screws that tighten the stack. Thus, copper-beryllium springs are used which ensure a constant force. Careful adjustment of the spring tightness needs to be done to avoid the PCB to get stuck. In the apparatus it was attached to a cyclotron resonator, which has an inductance of around 2.1 µH. In the setup, after cooling to 4 K, the frequency could be changed with the LTMV from 14.5 MHz to 20.5 MHz, showing a

[4] More specifically Kapton.
[5] Stray capacity has little impact due to the relatively large distances compared to the opposing plates.

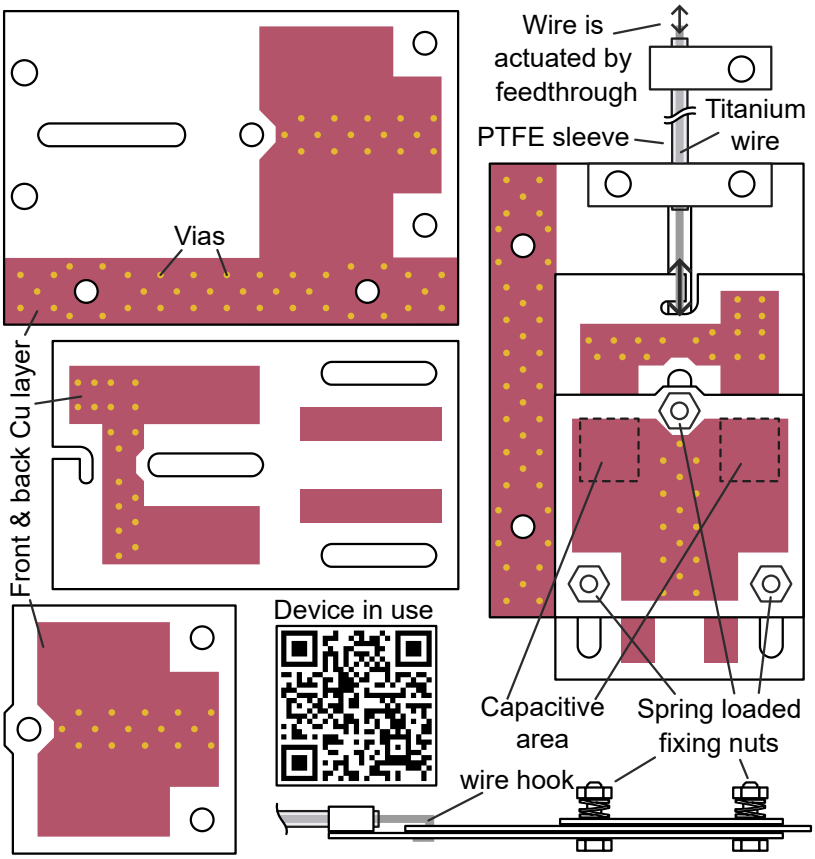

Fig. 10.4: LTMV design, including a QR code that links to a video that shows the LTMV in use (upside down and not fully assembled for testing purposes). (VideoLink: www.youtube.com/watch/peySYswfFkc)

capacity change of around 30 pF, all while maintaining a Q value of around 1400. This calculation assumes that the capacitance reached values close to zero in its pulled out state, the 20.5 MHz resonance frequency gives a value for the capacitance of the circuit without the LTMV.

Typical ions in the trap have a modified cyclotron frequency between 20 MHz (HD^+) and 26 MHz (C^{5+}). Using a lower inductance, or removing unnecessary capacitive load[6] could change the range to have a larger overlap with the given width of possible modified cyclotron frequencies.

Note, that this design exhibits large hysteresis, making it necessary to hand-adjust the LTMV. This is due to the slack within the PTFE tubing for smooth coupling of the mechanical motion.

Overall the LTMV shows great performance. Little chance of the Q value over its complete tuning range is observed, suggesting that it is not the limiting factor for losses in the circuit. For the future the range should be adjusted, which would enable direct modified cyclotron cooling for an even larger number of ions.

10.3 Superconducting Shield

Superconducting magnets have shown extremely stable and often very homogeneous magnetic fields, which are beneficial for a multitude of high-precision experiments. Nonetheless, with ongoing technical advances a multitude of experiments are limited by the magnetic field stability [22, 29, 140]. In this thesis, the precision of the measured hydrogen-like and the lithium-like Γ_0 is limited by the magnetic field fluctuations during the measurement. Hence, reducing the drifts and the jitter of the magnetic field could potentially increase the precision in the measurements and therefore give new measurement opportunities.

[6] To lower the tuning range, a semi-rigid coaxial wire has been added as a parallel capacitor which could be removed in the future to lower the overall capacitance.

By design, the superconducting magnets have a certain screening effect where external field changes are partially compensated by the magnet coils themselves [160]. To evaluate the effectiveness of the screening, the self-shielding factor is typically used. It describes the amount of screening (in z direction) at the center of the trap

$$S^{-1} = 1 - \frac{B_{\text{ind}}}{B_{\text{ext}}}. \tag{10.1}$$

With B_{ext} as an external change of the magnetic field in the form $\mathbf{B} = B_{\text{ext}} \times \mathbf{e}_z$ and B_{ind} as the field in the center produced by the current induced in the persistent coil by the magnetic field change B_{ext}. In example for the ALPHATRAP magnet the self-shielding factor has been measured in the past and amounts to about a factor of 14 [52]. Often additional self-shielding coils (SSC) are implemented [52, 119, 160] to further increase the shielding. Theoretically for homogeneous solenoids, infinite shielding can be achieved for a specific length-to-width ratio. These are typically mounted on top of the inner vacuum chamber which enables precise positioning relative to the trap. Such a SSC is wound around the ALPHATRAP trap chamber, which was probed to have a shielding factor of 7 [52].

Here, we present a novel approach that does not require a perfect geometry. Instead of using a coil, a cylinder made from superconducting bulk material is used. This has the advantage, that through every closed loop within the shield, the magnetic flux is conserved by the currents induced in the cylinder. Thus, a large volume within the cylinder is screened extremely well. In the limit of an infinitely long cylinder the screening is infinite, but already with large aspect ratios extremely high shielding factors can be achieved.

Another advantage is that, while a self-shielding coil (SSC) only screens $\mathbf{B}_z$ changes, the bulk superconducting shield (SCS) also compensates changes in radial direction. Essentially, this approach should result in improved magnetic field stability for better high-precision measurements. Using COMSOL, the shielding factor for a cylinder with an aspect ratio (length to diameter) of roughly three is simulated. The self-shielding factor along the z axis is shown in Fig. 10.6. In the center a shielding of up to 5 orders of magnitude is reached over a rather large volume, greatly relieving the tolerances on the positioning required for a high shielding. As superconductor niobium-titanium is used, which has a high critical field strength and a critical temperature above liquid helium temperature. While it should be possible to manufacture a complete trap chamber from NbTi, for simplicity here a design was chosen that encloses the trap chamber from the outside, simplifying the implementation. This was built into the setup after the tin campaign, and first results on the shielding are presented here.

The NbTi cylinder has a length of 315 mm, and an inner diameter of 104 mm. The wall thickness is 3 mm giving it an outer diameter of 110 mm, which is designed to fit into the 77 K heat shield within the magnet bore. The setup is shown in Fig. 10.5.

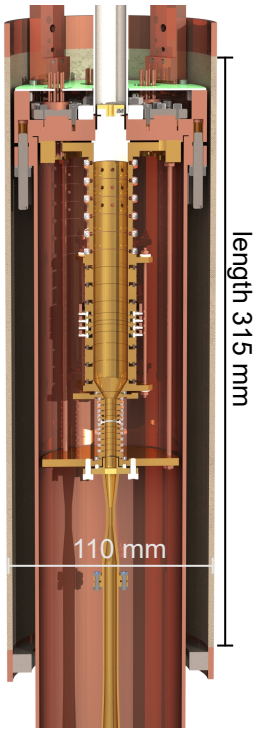

Fig. 10.5: Cut-section of the SCS enclosing the trap chamber.

At the top and at the bottom of the cylinder, copper rings are welded, which incorporate the screw holes necessary to fixate the shield to the four vertical copper bars of the apparatus. At the bottom, a custom bracket and screws fixate the shield to the trap-chamber mitigating any relative movement between the two. The shield is roughly centered around the PT, were thehigh-precision measurement takes place. After the cool down with the implemented shield, it was tested for its shielding factor. It was characterized by measuring the magnetic field change induced by a small external magnetic field coil which was wound on the outside of the superconducting magnet. The magnetic field is determined with an ion in the PT.

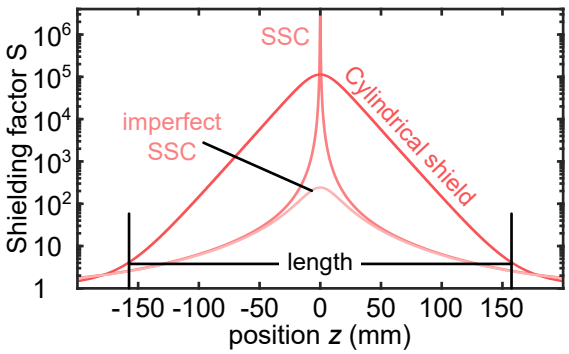

Fig. 10.6: Self-shielding factor along the z-axis for a NbTi cyclinder placed symmetric around $z = 0$. The inner diameter is 104 mm and the outer diameter is 110 mm. The length is 315 mm. Also shown is the self-shielding factor for a perfect SSC. For this S is infinite at $z = 0$, The shielding factor redues much quicker when the coil is not perfectly aligned compared to the SCS. Additionally shown is the curve for a SSC with a 1 % error in the length-to-width ratio. This already reduces S to about 200 in the center.

Next, current is applied to the external coil, in order to measure the shift of the magnetic field at the position of the ion. In order to extract a self-shielding factor the SCS is quenched with a manganin wire wound around the SCS. The magnetic field is measured again for either state of the external coil, which gives the overall external field change B_{ext}. Note that the shielding of the magnet does not influence the measurement, as it cancels in the ratio $^{B_{\text{ind}}}/_{B_{\text{ext}}}$. With this, a shielding factor of 130(40) was measured for the SCS, with the uncertainty stemming from the precision of the frequency determination. While this is a factor of 9 improvement over the prior implemented SSC, it is far below the expected 5 orders of magnitude, leaving the question why this does not agree with the simulations. One possibility is that only parts of the NbTi is actually superconducting. If there are some local variations of the stoichiometry of the material, parts of the shield might exhibit a lower critical field. Nonetheless, this is rather unlikely as a quenching of the shield was only observed[7] when the temperature of the shield was getting close to the critical temperature at 7 to 8 K. This was measured with a calibrated thermometer attached to the upper copper piece which is welded to the cylinder. Therefore, further research is required. This includes detailed tests in a coldhead, where one could exclude uncertainties such as the temperature distribution.

Even though the shielding factor is far below the value expected from simulations, the shielding factor of 130 is a significant improvement over the prior installed SSC[8], which only had a shielding factor of around seven [52]. Following this, tests were made to characterize the magnetic field stability and compare it to the data recorded in the tin campaign.

Magnetic Field Stability

This is tested using a $^{12}C^{5+}$ ion. This was done with the PnA method, where the phase accumulated after a free evolution time is continuously recorded. Only ν_+ is measured, which is for these purposes a good estimate of the changes of the magnetic field. Overall multiple measurements were performed with different evolution times, and some were running for multiple hours. In Fig. 10.7, two datasets with the longest times used (66.2 s and 99.2 s) are shown. The measurement with 99.2 s evolution time was running for roughly 12 hours, while the 60.2 s measurement ran for around 4 hours. For both, the Allan deviation is calculated [161] and shown in the right side in the figure. This is a variation of the standard deviation to see how the measurement stability behaves as a function of the averaging time τ. By taking the standard deviation of the data for different averaging times, the evolution of the stability for different time intervals can be compared. For both measurements, the magnetic field is drifting over time. This was on the order 100 ppt per hour, which is similar to what is reported by other experiments [137, 162], apart from one with

[7] Observed by a jump in the modified cyclotron frequency induced by the external coil.
[8] The SSC was removed before the SCS was implemented into the setup.

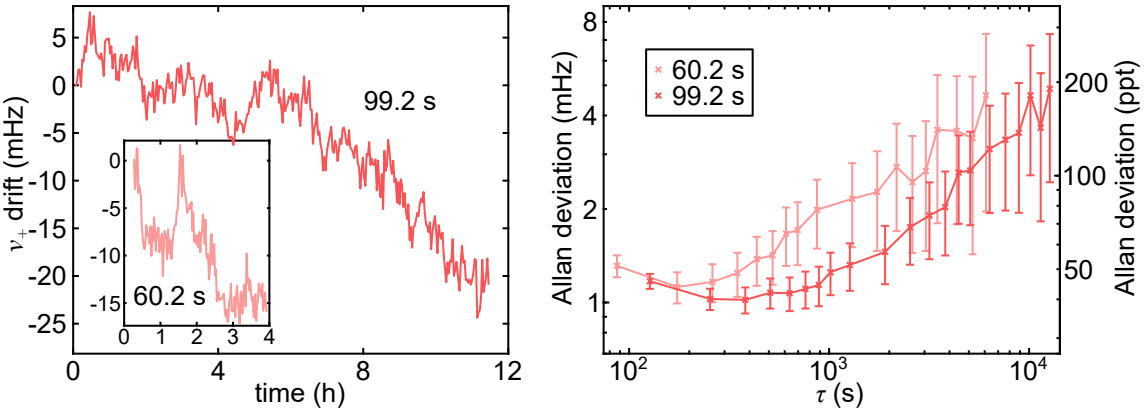

Fig. 10.7: Sampled data for two different phase evolution times (66.2 s and 99.2 s) along with the Allan deviation of the data [161]. The inset in the left plot has the same scaling as the outer plot. During both measurements, drifts of multiple 10 mHz occurred in a couple of hours. Short-term, the stability is quite good, and among the highest reported with a shot-to-shot stability of around 46 ppt (51 ppt) for the 99.2 s (60.2 s) measurement [137, 163].

exceptional long term stability [163]. In the past, before the SCS was implemented, the magnetic field drift was typically on the order of 500 ppt to 1000 ppt per hour.

Now with the SCS a shot-to-shot stability of about 50 ppt is observed, which is significantly better than the about 200 ppt that have seen in the tin campaign (compare Tab. 9.2). The shot-to-shot noise improved by about a factor of four, which is less than the observed shielding factor improvement of $^{130}/_{7} \approx 19$. Also the long-term drift does not seem to fully correlate with the improved shielding. This can be due to multiple reasons. For once, the drifts of the axial frequency would cause a shift of the PnA phase, due to the varying phase accumulation of the axial mode during and after the coupling before the readout. Normally this is irrelevant, as it is compensated with the reference phases, as they would exhibit the very same shift of phase, but for the stability measurements presented here, no reference phase is recorded, thus a large shift of the axial frequency would give a systematic drift of the frequency. This can be excluded though, as the axial frequency was recorded regularly, and no significant drift was observed.

Another possibility is that a jitter of the axial frequency, in example due to the instability of the power supplies, would cause a jitter in the modified cyclotron frequency, according to Eq. (3.6). From dip measurements the axial frequency shot-to-shot stability is typically below 30 mHz. This would correspond to an added ν_+ jitter of about 0.9 mHz, which is close to the observed ν_+ shot-to-shot stability (1.3 mHz). Nonetheless, it is unclear whether the observed axial frequency stability is actually limited by the axial frequency stability or rather by the resolution of the dip measurement. This could be further resolved using phase-sensitive methods to determine the stability with much higher resolution.

Other explanations of the observed residual jitter might be the inherent magnetic properties of the surrounding structures, including the copper electrodes. If these in example exhibit a temperature dependent magnetization, minuscule temperature fluctuations could perturb the field, causing a change of the magnetic field within the trap. Ref. [164] gives an overview of many properties of copper. It has a detailed analysis of the magnetic susceptibility κ of copper for temperatures above 1.4 K. These tests were done with oxygen free C10100 copper materials, which has a purity of about 99.999 %. The electrodes in the ALPHATRAP setup are produced from the same grade of copper. Even with this high purity copper the unknown residual iron impurity has still a significant impact on the temperature dependence of the susceptibility at temperatures

below 10 K [164]. There some samples showed a temperature dependence of up to κ of 0.3×10^{-6} per kelvin at temperatures around 4.2 K. If then the temperature of the trap electrodes near the ion exhibit a variation over time, this could result in a change of the magnetic field within the trap. Simulations of the trap region using COMSOL showed that a temperature change of 1 mK for a single correction electrode in the PT causes a relative magnetic field change of about 4×10^{-12}, which is a shift of about 0.1 mHz in the modified cyclotron frequency of hydrogen-like carbon. A 1 mK change of the complete trapstack would also result in a 5×10^{-12} change of the field. Since the ALPHATRAP setup is not equipped to measure such localized temperature changes, the temperature stability is unknown. The installed temperature sensor at the bottom of the liquid helium cryostat shows a temperature fluctuation at 100 s intervals of about 70 µK. While it is unlikely that the temperature fluctuations at the trap stack are orders of magnitude higher, it cannot be excluded, as the sensor at the cryostat is placed close to the cryostat, which might buffer temperature fluctuations.

Overall, the results of the shield are promising, but further investigation is required. This would include a better measurement of the axial frequency stability in the PT. Additional temperature sensors near the chamber would also be useful to observe the temperature stability closer to the trap. An additional test would be to measure the impurities of the copper electrodes, to better estimate their influence on the temperature dependence. Furthermore, one could built a trap stack made from a different material to see whether the magnetic field stability changes. In the following section a new trap design is suggested that uses a monolithic block of fused silica with a gold-coated surface.

10.4 Fused-Silica Trap

Another project carried out within this thesis is the design of a trap stack that uses different manufacturing techniques than the typically used copper-sapphire trap stacks. It relies on laser etched fused silica (FS) coated with a thin layer of conductive material, i.e. gold. In this selective laser-induced etching (SLE) technology a pulsed laser locally heats the FS within its focus, which permanently modifies the material [148]. A subsequent etching step with a wet agent removes the modified material, which can then be used to structure the FS substrate with a high degree of freedom. This could provide smaller tolerances since in the original stacked approach, manufacturing imperfections of the individual electrodes are "stacked". Furthermore, with this monolithic design made from only fused silica[9], thermal expansion during cool down would be quite homogeneous, and possible misalignment is reduced compared to the electrode stack which incorporates multiple materials with different expansion coefficients. The presented design exhibits two half cylinders, which are then placed on top of each other to built the cylindrical trap. The different electrodes would be separated using a T-shaped channel with a high aspect ratio, as shown in Fig. 10.9. After the SLE process, the half cylinders would be covered with a thin layer of gold. Because of the T-shaped gaps neighboring electrodes are electrically isolated. For the coating an anisotropic technique like physical vapor deposition (PVD) would be suitable. The individual electrodes would then be contacted using wire-bonds to an interface PCB as shown in Fig. 10.8. The here presented design includes two separate trap sections with separately optimized electrode geometries for high harmonicity. The one in the center is a 7-pole trap, with a combined orthogonality criteria for the two sets of correction electrodes. The theoretical background required to replicate such a design can be found in the thesis of Florian Köhler [86]. As introduced in the Penning-trap chap-

[9] The thin film of gold on top contributes negligibly to the thermal expansion, and would rather produce stress on the surface, requiring good adhesion between the FS and the gold coating.

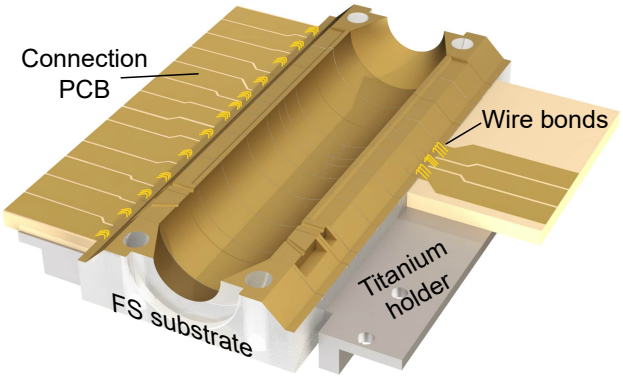

Fig. 10.8: Concept design for a FS trap. The half cylinder design is shown, which is placed on top of a titanium holder on which the PCB for the electrical connection rests as well. Via wire bonds, the required biasing voltages are applied to the electrodes. The PCB is then used as a solder pad to connect external wires. For the complete design, two half cylinders are stacked to complete the cylindrical trap.

ter (Chapter 3), the goal is to have a very harmonic trap, with negligibly small higher-order C_n coefficients.

The second trap at the side is a 5-pole design, incorporating only two correction electrodes. The outermost end-cap electrode is tapered for mechanical stability and to change the radius the one in the AT of ALPHATRAP. Apart from the tapered end-caps, the trap is designed with a radius r_0 of 5 mm. Since the end cap of the 5-pole trap is tapered, this must be included in the optimization process for the harmonicity of the trap, requiring special care of asymmetric terms. This has been done using a COMSOL simulation of the electric field produced by the electrodes, which combined with an optimization of the applied voltages and the length of the individual electrodes was used to optimize the harmonicity of the trap. While the 7-pole trap is optimized only for the even-order terms, as the odd-order terms are zero due to the axial symmetry, the 5-pole trap must be treated differently. Thus it is optimized for the criteria $C_3 = 0$, $C_4 = 0$ and $C_6 = 0$. Additionally $D_1 = 0$ and $D_2 = 0$ is required. These are the first and second order coefficients of the field produced in the trap center by the two correction electrodes. This is helpful for the later operation of the trap, as a change in the applied tuning. Due to the chosen optimization criteria, it is unavoidable that by design the trap will exhibit non-zero odd higher-order terms. The first unoptimized term is C_5. From the simulation this should be on the order of 1×10^{-2} for the chosen characteristic trap length $d_{\text{char}} = 5\,\text{mm}$.

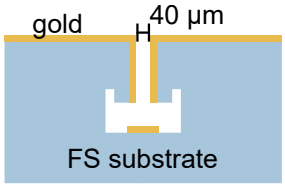

Fig. 10.9: Cut-section of the T channels that ensure electrical isolation between neighboring electrodes.

Tab. 10.1: Geometry of the 7-pole trap on the left, 5-pole trap on the right. The 7-pole one is axially symmetric, so odd C coefficients are zero by design, apart from imperfections due to manufacturing tolerances and the accuracy of the voltage sources. By minimizing C_4, C_6, C_8, C_{10} and D_2^{comb}, the trap is designed for highest harmonicity even at high amplitudes, the means to repeat such optimizations are explained with ample details in Ref. [86]. The 5-pole trap is asymmetric due to the tapered end-cap electrode, this is included in the optimization, to reduced the dominating odd order coefficient C_3, in addition with the other coefficients C_4, C_6, D_1 and D_2.

Electrode	Size (mm)
Endcap l_{EC}	4.0
Correction 2 l_{cor2}	3.454
Correction 1 l_{cor1}	2.098
Ring electrode l_{r}	1.147
Tuning ratio	**Value**
Tuning Ratio 1	0.96361
Tuning Ratio 2	0.81567

Electrode	Size (mm)
Endcap l_{EC}	4.0
upper correction l_{upper}	3.904
Ring electrode l_{r5}	1.633
Lower correction l_{lower}	4.209
Lower Endcap (tapered) $l_{\text{ECtapered}}$	4.0
Transfer copper electrode	4.0
Tuning ratio	**Value**
Upper Tuning Ratio	0.88047
Lower Tuning Ratio	0.87187

As discussed in Sec. 3.2.2, odd-order coefficients only shift the frequency in second order. This means that it only couples to other asymmetric trap terms, like C_5 or B_1. So the dominant shifts including C_5 scale with C_5^2, $C_5 \times C_3$, $C_5 \times B_1$ [90]. These typically scale with high order of $\hat{z}$, e.g. the ν_z shift from the C_5^2 term scales with $\hat{z}^6$, making it only relevant at large amplitudes far above the typically range in the traps ($< 100\,\mu m$). The gap size is chosen to be $40\,\mu m$, $100\,\mu m$ smaller than in the previous stacked design, which is possible due to the precision of the SLE process. Nonetheless, with smaller gap sizes, dust particles might get into the crevices, potentially shorting neighboring electrodes. Hence handling and assembly in a clean-room facility, which is available at the Max-Planck-Institut für Kernphysik, is advisable.

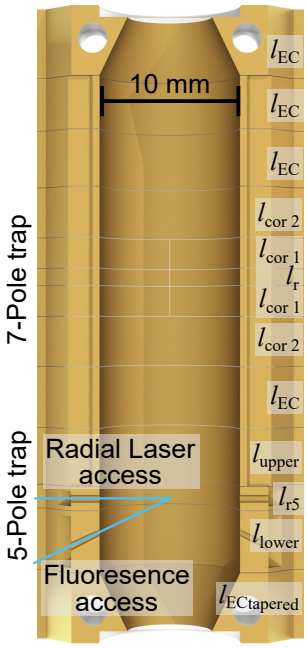

Fig. 10.10: Top view with the half cylinder. Also shown are the ports for optical access.

The two-trap design serves multiple purposes. The center 7-pole trap is implemented for utmost harmonicity similar to the PT of the ALPHATRAP setup, which is therefore aimed at high-precision spectroscopy. The second, the 5-pole trap, is also optimized but not as strictly, limited by the asymmetric design. Here high harmonicity is not as essential as for a Precision trap. In the 5-pole trap, radial access is provided by small holes on the top surfaces of the half cylinder. Next to it another port for fluorescence detection is implemented, as shown in Fig. 10.10. The presented design incorporates a 4° view angle for this. In example for $^9Be^+$ and the 313 nm cooling transition, a few 10 000 scattered photons leave the trap through the fluorescence port. Placing there a silicon photo detector, as in example used for cryogenic application in Ref. [165], which have a typical quantum efficiency of 20 % to 40 % this results in a rate of about a few thousand photons every second. Furthermore, the two-trap design can also be used to couple ions in two separate traps. This was already demonstrated in the past by our group [113].

Chapter 11

Conclusions

Looking back to Fig. 1.1 in the introduction, the here presented g-factor measurements are a jump into the high electric field regime. In the following, the measured values are compared to their theoretical predictions. Each is brought into perspective to evaluate the implications of each measurement.

Note that the here discussed theoretical g-factor calculations were not within the scope of this thesis. They were performed by the group of Zoltán Harman and by Vladimir Yerokhin, both at the Max-Planck-Insitut für Kernphysik.

After both the experiment and the theory finalized their values and evaluated their uncertainties, the results were compared[1].

11.1 Hydrogen-like Tin

The measurement of the hydrogen-like tin g factor is made possible by the combination of two state-of-the-art instruments: The Heidelberg-EBIT for the external ion production and the Alphatrap-apparatus with its high-precision measurement capabilities. With the achieved precision of 0.5 ppb, the theoretical prediction of the bound-electron g factor can be precisely tested.

As introduced in Chapter 2, the theoretical description takes into account not only the free-electron contributions, but also the various bound-state (BS) effects. Its calculation is described in detail in the publication for this measurement [54]. The overall theoretical prediction is $g^{\text{H-like}}_{\text{theory}} = 1.910\,561\,821(299)$. The experimental value agrees with this within 0.8 sigma. The relative uncertainty of 1.5×10^{-7} is currently limited by the uncalculated higher order terms in the $Z\alpha$ expansion, namely the terms scaling with order $(Z\alpha)^6$ and higher. The next largest uncertainty comes from the finite nuclear size (FNS) correction with a relative uncertainty of 1.2×10^{-8}. This consists of two uncertainties, shown in the summary Table 11.1: the first results directly from the experimental uncertainty of the nuclear charge radius, as given in Ref. [74]. The second is the model uncertainty estimated by comparing the finite nuclear size correction for a homogeneously charged sphere and the two-parameter Fermi model.

As described in Chapter 2, one-loop calculations are performed using a rigorous all-order approach, while the 2-loop terms are only calculated till the fifth order in the $Z\alpha$ expansion. With the measurement of tin, for the first time in g factors, the Wichmann-Kroll correction (labeled *VP-EL, WK* in Tab. 11.1) is tested with about 2 sigma confidence. This is the VP term that

[1] Note that for the hydrogen-like g factor, a preliminary value of the theory was used to search for the resonance in the experiment. Nonetheless since the experimental precision is orders of magnitude higher than for the theory, and systematic shifts that could cause significant discrepancies are non existent, it is unlikely that the experimental value is getting biased even with the complete theoretical prediction.

Tab. 11.1: Table of the theoretical prediction of the hydrogen-like tin g factor. The data is taken from [54]. Corrections too small to be relevant like the electroweak correction, are not shown here. In the barplot, the vertical lines are from left to right the uncertainty of the theoretical prediction, the experimental uncertainty limited by the mass and lastly the uncertainty on Γ_0. Light-green bars are showing the size of the contribution. The overlaying dark-green and black bars are the uncertainty of the respective contributions, either coming from uncalculated diagrams (dark-green) or from the experimental uncertainty of the charge radius/distribution (black bars). The abbreviations ML stands for magnetic loop, here it refers to the Feynman diagrams, where the same VP loop exchanges a photon with both the bound electron and the external magnetic field. EL is the electric loop in which the VP only exchanges photons with the bound-electron. SESE refers to the two-loop terms with two SE vertices.

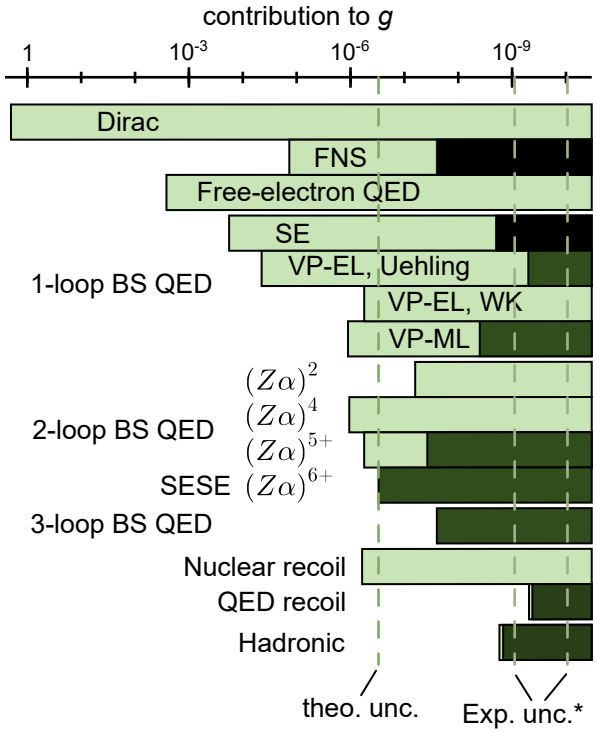

Term		$^{118}Sn^{49+}$
Breit		1.908 079 205 3(1)
FNS		0.000 014 489 4(110)(211)
1-loop	$(Z\alpha)^0$	0.002 322 819 5
	SE binding	0.000 182 170 1
	SE-FNS	-0.000 000 159 4(21)
	VP-EL, Uehling	-0.000 035 089 7(5)
	VP-EL, WK	0.000 000 658 4
	VP-ML	0.000 001 225 0(40)
	muonic VP	-0.000 000 002 7(14)
2-loop	$(Z\alpha)^0$	-0.000 003 544 6
	$(Z\alpha)^2$	-0.000 000 078 6
	$(Z\alpha)^4$	-0.000 001 123 8
	$(Z\alpha)^5$	0.000 000 211 0(215)
	$(Z\alpha)^{5+}$	0.000 000 286 5(53)
	$(Z\alpha)^{6+}$ SESE	0.000 000 000 0(2968)
≥3-loop	$(Z\alpha)^0$	0.000 000 029 5
	$(Z\alpha)^{2+}$	0.000 000 000 7(105)
Recoil	$\left(\frac{m}{M}\right)^1$	0.000 000 726 8
	$\left(\frac{m}{M}\right)^{2+}$	-0.000 000 000 1
	QED recoil	-0.000 000 000 5(4)
Hadronic	Uehling	-0.000 000 001 8(14)
Sum		1.910 561 821 0(2988)
Exp.		1.910 562 059 0(9)

includes light-by-light scattering effects, which describe the multi-photon exchange between the virtual electron-positron pairs and the nucleus. Specifically this is part of the VP electric loop (EL) contribution, where the interaction with the magnetic field is separate from the VP loop. The decomposition of the VP-EL loop contribution is shown in Fig. 11.1. The lowest order is the Uehling term, where the electron-positron pair interacts once with the electron and once with the nucleus. The WK are the higher orders, where the nucleus interacts 3, 5, etc. times with the vacuum. As a higher order bound-state QED effect, the WK correction scales strongly with $Z\alpha$, more so than the uncertainty of the uncalculated two-loop terms. Therefore in tin its contribution is larger than the total theoretical uncertainty, which was not the case for any of the measured low-Z ions, allowing this contribution to be tested for the first time.

Looking at the broader picture of other tests of bound-state QED, one cannot overlook the stringency of Lamb-shift measurements of the hydrogen atom. With the proton radius puzzle coming to an end [166], the spectroscopy of the hydrogen level structure can be seen as a very stringent test of bound-state QED inherent to the simplest atom. Recent measurements performed on the $2S - 6P$ transition with hydrogen[2] show an experimental uncertainty of 500 Hz. The size of the Lamb shift is about a GHz [167], which results in a test stringency of about 5×10^{-7}. Thus,

[2]Talk by Lothar Maisenbacher at the International Conference on Precision Physics of Simple Atomic Systems (2024).

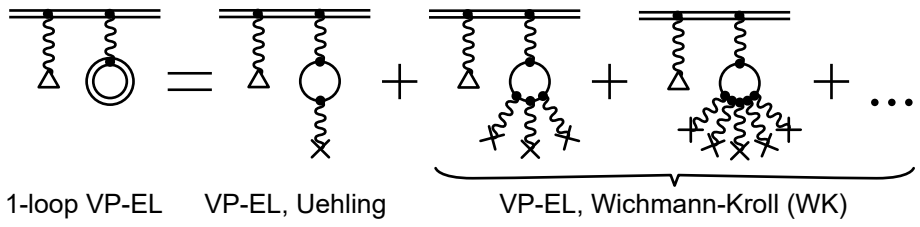

Fig. 11.1: Decomposition of the VP-EL contribution into the Uehling contribution and the WK contribution. Photon lines terminated with a cross denote an interaction with the nuclear binding potential.

the various contributions are tested with extremely high precision, and the importance of these tests cannot be understated. However, these measurements test the theory far from the relativistic regime since $Z\alpha \approx 0.007 \ll 1$. So tests of the all-order theory, together with the extremely high Coulomb field of the nucleus at high Z, where $Z\alpha$ reaches almost unity, are of utmost importance.

To give a bit of a context on what has been achieved in this high field regime, an overview of other measurements is presented. For once, for selected high-Z elements there are Lamb-shift measurements of high charge states as for example performed on hydrogen-like and lithium-like uranium [31, 32]. These where performed in the early 2000s, and still hold as extremely valuable tests of this strong field regime. There is also a recent measurement in helium-like uranium, where the $2p_{3/2}$ to $2s_{1/2}$ transition is measured [34]. Furthermore, a measurement of the Kα lines also in helium-like uranium was recently presented [33]. This uses micro calorimeter for X-ray spectroscopy, which enabled for the first time to resolve the individual lines of the Kα transitions. The theoretical prediction for these transitions in uranium is calculated to all-orders for both the one-loop and the two-loop QED terms, which is not yet the case for the bound electron g factor.

Apart from Lamb shifts and g factors, it is also possible to test QED with the hyperfine structure. These tests of the hyperfine structure have to include the complex interaction of the electron spin with the extremely high magnetic field of the nucleus which in certain cases can reach magnetic field strengths above 20 000 Tesla [39]. While this interaction is extremely interesting from a scientific point of view, at the same time it imposes a hard limit on the precision of the theoretical prediction. For once it relies on the measurement of the (unscreened[3]) nuclear magnetic moment, which caused problems in the past [37, 38]. Secondly, the structure of the nuclear magnetic moment – which influence is known as the Bohr-Weisskopf (BW) effect – is quite complex and impose further limits on the theoretical prediction. The BW effect can be compensated by using the so-called specific difference [40]. By measuring two different charge states and estimating the scaling of the limiting contribution, one can cancel its contribution and with it the uncertainty. Using this method, with the measurements of the hydrogen-like and lithium-like hyperfine splitting in bismuth-209 a stringent test of QED has been performed [37]. A specific difference method was also recently used in ^{9}Be, marking an extremely stringent test in the low-Z regime [30].

Other tests are performed with measurements of Lamb shifts in muonic atoms. A lot of these were done in the 80s, which are predominantly used for the determination of nuclear charge radii. Nonetheless, there are a few measurements dedicated to testing the QED contribution, which are performed in electric field strengths far greater than any electronic system can reach. This is due to the heavy mass of the muon, which results in an extremely small muon orbit $\propto 1/m$. This greatly increases the overlap with the nucleus. Furthermore, compared to the electronic systems, the VP terms are significantly larger relative to the SE terms, uniquely testing these with extraordinary precision. A highlight measurement is the spectroscopy of the $3d_{5/2} - 2p_{3/2}$ transition in muonic

[3]It is possible to measure the magnetic moment of the nucleus in a neutral atom, but the bound electrons cause a certain amount of screening, that can be difficult to evaluate properly.

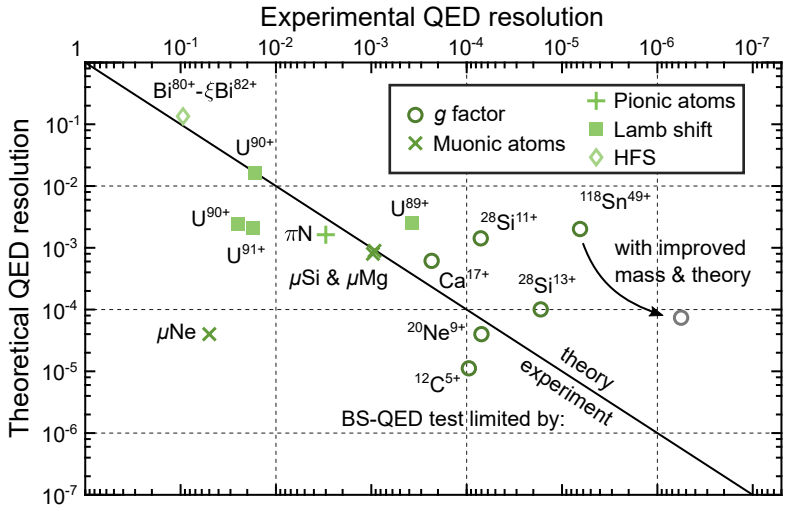

Fig. 11.2: The figure shows various tests of bound-state QED in strong electromagnetic fields. The gray point shows the updated position once the rigorous calculation for the two-loop QED effects is complete, and the mass is improved further. The shown theory limit of 8×10^{-4} is then due to uncertainty of the finite nuclear size contribution. The figure is adapted from Ref. [54]. The individual points are evaluated from Ref. [15, 16, 22, 24, 25, 27, 31–34, 37, 38, 168–170].

magnesium and silicon [15]. The selected transition is barely sensitive to the nuclear charge radius, and can therefore test the QED interaction extremely well [41].

Fig. 11.2 compares the experimental and theoretical uncertainties relative to their bound-state QED contribution for the most stringent measurements in the strong-field regime. Only bound-state radiative terms are considered, terms scaling with $\alpha(Z\alpha)^2$ or higher. This excludes the free-electron QED terms in g factors as one can fairly say that these are tested to highest precision by the $g-2$ experiment. For completeness, the low-Z g factors are shown as well, although all of them exhibit field strengths at least an order of magnitude lower than in tin. Considering the electric field in which these measurements take place, the muonic and pionic measurements are unparalleled [15, 16]. The Lamb-shift measurement in hydrogen-like uranium are the next highest with field strengths at around $1 \times 10^{16}\,\mathrm{V/cm}$ [32]. In hydrogen-like tin, the field is with about $1.6 \times 10^{15}\,\mathrm{V/cm}$ slightly below that of the $2s$ electron in lithium-like uranium. Off all these high-field tests, the measurement of the hydrogen-like tin g factor is by far the most precise, relative to the bound-state QED contributions. If in the future the mass gets remeasured by a dedicated experiment with improved precision [140], the here presented Γ_0 measurement has the potential to resolve the bound-state QED part to about 6 orders of magnitude. However, the theoretical uncertainty currently limits the test stringency, which needs to be improved before a more precise mass is required.

To summarize, the hydrogen-like tin measurement marks a ground-breaking test of QED, which was made possible by years of effort in combining two state-of-the-art experimental setups for production and spectroscopy. With $Z = 50$ it is a great step towards the heaviest available atoms, and $Z\alpha \approx 0.37$ is significantly higher than in any prior high-precision g-factor measurement. As a first this brings the tests of QED with bound-electron g factors onto the same level as with other observables. Furthermore, with the anticipated completion of an all-order two-loop calculation, this test can be improved by more than an order of magnitude, at which point other contributions as the finite nuclear size uncertainty limit the test stringency.

The next step for precision tests of QED in high-Z g factors will occur once the Hyper-EBIT is completed and hydrogen-like lead and uranium will be available and can be measured. This will improve the tests of QED even further, not only by having a significantly higher field strength, but also having a much higher sensitivity to the higher order bound-state QED effects, as the uncertainty of the all-order calculations is expected not to scale with Z, but rather with the numerical precision of the calculations[4]. At this point, it might become crucial to better estimate

[4] From private communication with Bastian Sikora.

Tab. 11.2: Table of the theoretical prediction of the lithium-like tin g factor. The data is taken from [64]. In the bar diagram, the vertical lines are from right to left the uncertainty of the theoretical prediction, the enhanced theoretical prediction, the experimental uncertainty limited by the mass and the uncertainty on Γ_0. Light-red bars are showing the size of the contribution. The overlaying dark-red and black bars are the uncertainty of the respective contributions, either coming from uncalculated diagrams (dark-red) or from the experimental uncertainty of the charge radius (black bars).

Term		$^{118}Sn^{47+}$
Breit		1.976 818 279
FNS		0.000 002 040(3)
Electron Structure		0.001 192 179(7)
QED screening		0.000 001 076(8)
1-loop	$(Z\alpha)^0$	0.002 322 819
1-e 1-loop		0.000 023 977(1)
2-loop	$(Z\alpha)^0$	-0.000 003 544
1-e 2-loop		-0.000 000 107(33)
- , enhanced		-0.000 000 080(6)
≥3-loop	$(Z\alpha)^0$	0.000 000 029
Recoil		0.000 000 172
Sum		1.980 354 769 (35)
Sum, enhanced		1.980 354 797 (12)
Exp.		1.980 354 799 8(9)

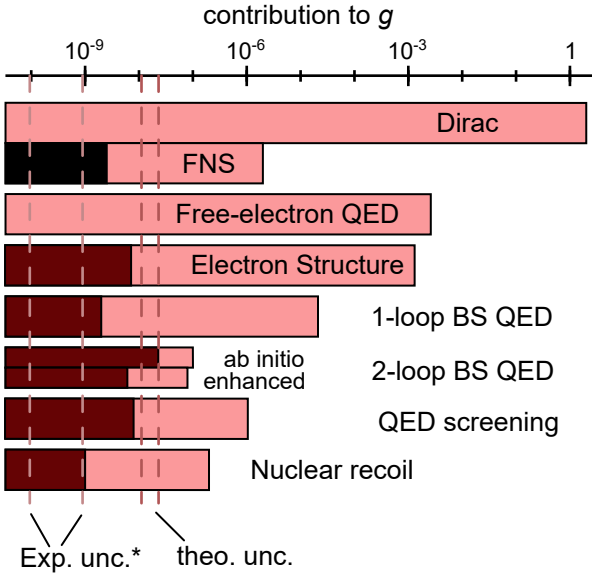

the model uncertainty in the finite nuclear size contribution to further improve the test stringency.

The demonstrated storage time, and the fidelity in spin-flip detection shows that such measurements of high-Z g factors are possible once the production of these is successful.

11.2 Lithium-like Tin

With the lower binding energy in lithium-like systems, the production is much simpler. Nonetheless, of all g-factor measurements, there are less lithium-like systems studied than hydrogen-like systems. Till now the highest Z lithium-like g factor measured is that of calcium ($Z = 20$) of which two isotopes have been studied separately for an additional test of the isotope shift [25]. The only other measured one is that of lithium-like silicon [23]. Therefore, the here presented measurement of tin is an important additional data point that also extends the tests of their theory into the medium-to-high Z range.

From a theoretical point, lithium-like g factors have become a big center of attention in recent years. When at first the measurements on lithium-like silicon and calcium were presented, the theory showed great agreement with the measurements [23, 25, 27]. But as calculations improved because of more detailed evaluation of the electron-electron interaction terms, discrepancies to the experiment became apparent [27, 55, 56]. In certain cases this reached close to 5-sigma discrepancy to the experiment. In 2022, Kosheleva *et al.* [57] presented theory calculations that seemingly resolved the discrepancies in the low-Z cases. It was suspected that the disagreement is a result of the used screening potential in the calculations, at the very least due to incorrect error estimation for uncalculated higher order corrections. To further strengthen the confirmation of this conjecture, a new measurement especially in the heavier regime would provide an independent test. The measurement of lithium-like tin therefore tests this not only with a new measurement, but also at much higher Z. The data on this is about to be published [64], and includes theoretical calculations done

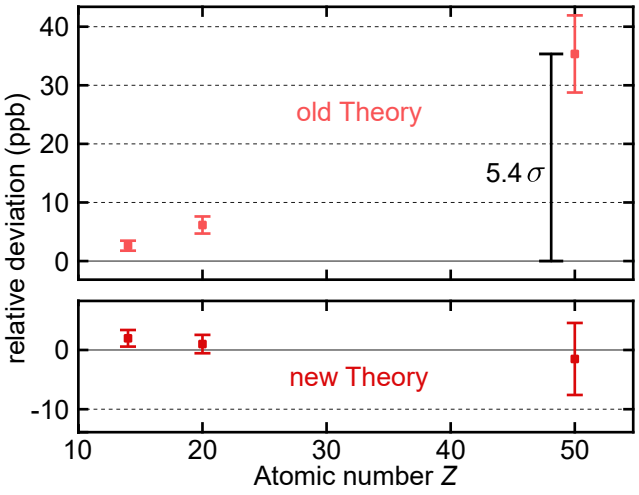

Fig. 11.3: Relative difference between the theoretical prediction and the experimental value of the three lithium-like g-factor measurements [25, 27, 64]. For tin, the enhanced theoretical prediction is used. In the the top figure, the theoretical prediction does not include the revised calculations, and the three available measurements disagree significantly from the experimental value. For $^{28}Si^{11+}$ and $^{40}Ca^{17+}$ the data is from [56], for $^{118}Sn^{47+}$ the value is kindly provided by Vladimir Yerokhin. In the bottom plot the comparison with the revised theory is shown [57, 64].

by Vladimir Yerokhin which is building upon the work done by Kosheleva *et al.* [57]. The overall lithium-like tin g factor was computed to be $g_{\text{theory}}^{\text{Li-like}} = 1.980\,354\,769\,(35)$. Tab. 11.2 summarizes the theoretical prediction [64]. This *ab initio* prediction is limited by the one-electron two-loop QED contribution to about 18 ppb. In the lighter systems, $^{28}Si^{11+}$ and $^{40,48}Ca^{17+}$, the limiting theoretical contribution is the electron-electron interaction. Therefore with the measurement of the lithium-like tin g factor, a test of the revised calculation of the multi-electron terms is limited by these single electron two-loop terms.

To overcome this limitation, as presented in [64], one can make use of the hydrogen-like tin measurement. Since the one-electron QED theory is similar in both systems, it is possible to enhance the theoretical prediction in the lithium-like system. Taking the measured $g_{\text{theory}}^{\text{H-like}}$ and subtracting all known terms gives an experimental value for the uncalculated higher-order QED terms. Using the scaling of QED terms between two different shells ($1/n^3$), or alternatively using the scaling in the known one-loop QED terms, one can predict the uncalculated terms for the lithium-like system. The enhancement reduces the uncertainty by about a factor of 5 for the two-loop correction, which is then smaller than the uncertainty of the electron structure and the QED screening corrections. This approach is fairly similar to that of the specific difference, where two measurements are combined with a scaling factor to cancel unknown effects, usually the finite nuclear size uncertainty [40, 171]. Due to the similar scaling, this enhanced value loses sensitivity to certain contributions, in particular the single-electron bound-state QED terms. Importantly, however, the electron-electron interaction terms are unaffected, as they are only present in the lithium-like system. Therefore it is possible to test these with the enhanced value. The enhanced theoretical prediction is $g_{\text{theory}}^{\text{Li-like}} = 1.980\,354\,797\,(12)$, which is in very good agreement with the experimental value. Fig. 11.3 shows the previous and the revised theoretical predictions in comparison to the available measurements for $^{28}Si^{11+}$, $^{40}Ca^{17+}$ and $^{118}Sn^{47+}$.

Overall, the agreement between the measurement and the enhanced value independently confirms the revised theory, and marks a rigorous test of these electron-electron interaction terms in this medium-to-high-Z range.

11.3 Boron-like tin

From the three measured g factors, the boron-like is the most difficult to acquire, both from a theoretical point, as well as on the experimental side. In the experiment, the spin detection is more difficult due to the smaller magnetic moment. In the theoretical description, the non-zero orbital angular momentum l must be taken into account, along with the more complex electron-electron interaction. Because of this, the theoretical description is less precise than for the s-shell g factors. The data for this measurement is about to be submitted for publication, along with theoretical calculations done by the group of Zoltán Harman. Since the theoretical calculations are not published yet, they will not be shown here, and the summary will be kept brief. Overall, the here presented determination is one of only two high-precision measurements of a boron-like g factor. So far only $^{40}Ar^{13+}$ has been measured [26]. Thus, the test of these is now also extended into the medium-to-high-Z range. As the theoretical prediction is currently less precise than the experimental value, it can also act as a benchmark for future theoretical work.

In the past, boron-like systems have been suggested to be combined with hydrogen-like measurements, aimed at the determination of the fine-structure constant α. With a specific difference, the finite nuclear size uncertainty can be significantly reduced, resulting in a truly *ab initio* approach limited only by the uncertainty of the theoretical prediction and the experimental measurement [171]. It is defined as

$$\Delta g = g^{\text{B-like}} - \xi g^{\text{H-like}}. \tag{11.1}$$

Here, ξ is the ratio between the finite nuclear size contribution in the boron-like and the hydrogen-like g factor. In this approach, α would be determined from the Breit correction to which Δg is still sensitive to. It follows that the achievable relative precision $\delta\alpha = {}^{\Delta\alpha}/_{\alpha}$ is given (to first order) by

$$\delta\alpha \approx \frac{2}{(Z\alpha)^2}\sqrt{(\delta g_{\text{theo}})^2 + (\delta g_{\text{exp}})^2}. \tag{11.2}$$

With δg_{theo} the relative uncertainty of the theoretical prediction, and δg_{exp} the experimental one. The ${}^{2}/_{(Z\alpha)^2}$ scaling suggests that a high-Z system would be advantageous, as these are the most sensitive to α. As of yet, most limiting for this approach is the theoretical prediction of the boron-like system, which in the region around tin has an uncertainty around 1 ppm [62, 147]. Therefore, orders of magnitude improvement is required from the theoretical side for such a determination. Nonetheless, this measurement proves the feasibility from the experimental side.

11.4 Summary and Outlook

In total, three bound-electron g factors were determined with a precision of 0.5 ppb, accompanied by a factor of ten improvement in the mass of the Sn-118 isotope, demonstrating the measurement capabilities of the Alphatrap apparatus. The comparison with the theoretical predictions provides rigorous tests of bound-state QED, now for the first time with a g factor at medium-to-high Z. The observed agreement for all three charge states shows that the Standard Model is extremely successful in predicting properties of atomic systems in the laboratory. Thus the search to complete our understanding of the universe continues.

In the pursuit to test bound-state QED in high fields at Alphatrap, the next steps rely partly on the completion of the Hyper-EBIT. This will allow the production of high-Z hydrogen-like ions, and the here presented test of bound-state QED can be performed on even heavier elements, probing bound-state QED in the strongest fields available.

Nevertheless, even without the Hyper-EBIT, measurements of lithium-like and boron-like ions

at high $Z > 80$, for example in lead and uranium, are possible, as their binding energy is much lower and their production is possible with the Heidelberg-EBIT. Therefore, if the two-loop all-order calculations are completed and extended to these charge states, such measurements could provide valuable tests at highest Z.

Another possibility is to measure the isotope shift with other tin nuclei, in order to study the nuclear structure. Tin is a rather interesting candidate, as it has 8 long-lived (many years) isotopes with zero nuclear magnetic moment, more than any other element. Here, experimental methods to measure the difference with 13 digits of relative precision[5] have been developed in our group [114] and could be employed when needed. Although even with the uncertainty reached in the measurements presented here, the theoretical prediction of the difference can be tested precisely. From this one could determine the nuclear charge radius difference, which might be useful for isotope shift measurements using optical spectroscopy.

Also interesting are tests of QED in the extreme conditions of highly charged ions with non-zero nuclear moment. Employing laser spectroscopy on a single ion would enable to determine the HFS in a high-Z ion, where the transition is in the optical regime. By doing this for the hydrogen-like and lithium-like systems it is possible to cancel the Bohr-Weisskopf effect, as was done in Ref. [37]. Furthermore, in a Penning trap it would be possible to determine the magnetic moment of the nucleus, which currently limits the stringency of the QED test performed in bismuth [37, 38]. The here demonstrated sensitivity to detect the spin state of a particle further paves the way for such a HFS measurement, where the change of the magnetic moment is small which requires high precision for the spin-flip detection.

Lastly, with the superconducting shield, the magnetic field stability improved, and might enable more precise g-factor measurements. With the observed factor of four improvement in the stability a precision of 10 ppt seems feasible. If systematic uncertainties allow, this could be used for more precise tests of QED, or even a new measurement of the $^{12}C^{5+}$ g factor, from which it is possible to determine the mass of the electron. If this reaches below 10 ppt, it would be the most precise determination of the mass of the electron.

[5] 13 digits relative to the g factor, not the difference.

List of Publications

- Bingsheng Tu, Felix Hahne, Ioanna Arapoglou, Alexander Egl, Fabian Heiße, Martin Höcker, Charlotte König, **Jonathan Morgner**, Tim Sailer, Andreas Weigel, Robert Wolf, and Sven Sturm. Tank-circuit assisted coupling method for sympathetic laser cooling.
  Advanced Quantum Technologies, **4**(7):2100029, 2021. Cited as Ref. [113].

- Tim Sailer, Vincent Debierre, Zoltán Harman, Fabian Heiße, Charlotte König, **Jonathan Morgner**, Bingsheng Tu, Andrey V. Volotka, Christoph H. Keitel, Klaus Blaum, and Sven Sturm. Measurement of the bound-electron g-factor difference in coupled ions.
  Nature, **606**(7914):479–483, June 2022. Cited as Ref. [114].

- **Jonathan Morgner**, Bingsheng Tu, Charlotte M. König, Tim Sailer, Fabian Heiße, Hendrik Bekker, Bastian Sikora, Chunhai Lyu, Vladimir A. Yerokhin, Zoltán Harman, José R. Crespo López-Urrutia, Christoph H. Keitel, Sven Sturm, and Klaus Blaum. Stringent test of QED with hydrogen-like tin.
  Nature, **622**(7981):53–57, October 2023. Cited as Ref. [54].

- Fabian Heiße, Menno Door, Tim Sailer, Pavel Filianin, Jost Herkenhoff, Charlotte M. König, Kathrin Kromer, Daniel Lange, **Jonathan Morgner**, Alexander Rischka, Christoph Schweiger, Bingsheng Tu, Yuri N. Novikov, Sergey Eliseev, Sven Sturm, and Klaus Blaum. High-precision determination of g factors and masses of $^{20}Ne^{9+}$ and $^{22}Ne^{9+}$.
  Physical Review Letters, **131**(25):253002, December 2023. Cited as Ref. [29].

- **Jonathan Morgner**, Vladimir A. Yerokhin, Charlotte M. Konig, Fabian Heiße, Bingsheng Tu, Tim Sailer, Bastian Sikora, Zoltan Harman, José Crespo López-Urrutia, Christoph H. Keitel, Sven Sturm, Klaus Blaum. Listening to electrons talk: g-factor measurement of lithium-like tin.
  Submitted to Science, 2024. Cited as Ref. [64].

- **Jonathan Morgner**, Bingsheng Tu, Charlotte M. König, Fabian Heiße, Tim Sailer, Matteo Moretti, Bastian Sikora, N. S. Oreshkina, Vladimir A. Yerokhin, Zoltán Harman, Christoph H. Keitel, Sven Sturm, and Klaus Blaum. g-factor measurement of boron-like tin.
  In Preparation. Cited as Ref. [72].

- Charlotte M. König, Fabian Heiße, **Jonathan Morgner**, Tim Sailer, Bingsheng Tu, Dimitar Bakalov, Klaus Blaum, Stephan Schiller and Sven Sturm. Hyperfine Spectroscopy of a Single HD^+ Molecular Ion in a Penning Trap
  Submitted.

Bibliography

[1] G. Kirchhoff. "Ueber Das Verhältniss Zwischen Dem Emissionsvermögen Und Dem Absorptionsvermögen Der Körper Für Wärme Und Licht". In: *Annalen der Physik* 185.2 (1860), pp. 275–301. ISSN: 1521-3889. DOI: 10.1002/andp.18601850205.

[2] Max Planck. "Ueber Irreversible Strahlungsvorgänge". In: *Annalen der Physik* 306.1 (1900), pp. 69–122. ISSN: 1521-3889. DOI: 10.1002/andp.19003060105.

[3] A. Einstein. "Über Einen Die Erzeugung Und Verwandlung Des Lichtes Betreffenden Heuristischen Gesichtspunkt". In: *Annalen der Physik* 322.6 (1905), pp. 132–148. ISSN: 1521-3889. DOI: 10.1002/andp.19053220607.

[4] N. Bohr. "The Spectra of Helium and Hydrogen". In: *Nature* 92.2295 (Oct. 1913), pp. 231–232. ISSN: 1476-4687. DOI: 10.1038/092231d0.

[5] E. Schrödinger. "Quantisierung Als Eigenwertproblem". In: *Annalen der Physik* 384.6 (1926), pp. 489–527. ISSN: 1521-3889. DOI: 10.1002/andp.19263840602.

[6] Paul Adrien Maurice Dirac and Ralph Howard Fowler. "The Quantum Theory of the Electron". In: *Proceedings of the Royal Society of London. Series A, Containing Papers of a Mathematical and Physical Character* 117.778 (Feb. 1928), pp. 610–624. DOI: 10.1098/rspa.1928.0023.

[7] Willis E. Lamb and Robert C. Retherford. "Fine Structure of the Hydrogen Atom by a Microwave Method". In: *Physical Review* 72.3 (Aug. 1947), pp. 241–243. DOI: 10.1103/PhysRev.72.241.

[8] H. A. Bethe. "The Electromagnetic Shift of Energy Levels". In: *Physical Review* 72.4 (Aug. 1947), pp. 339–341. DOI: 10.1103/PhysRev.72.339.

[9] Julian Schwinger. "On Quantum-Electrodynamics and the Magnetic Moment of the Electron". In: *Physical Review* 73.4 (Feb. 1948), pp. 416–417. DOI: 10.1103/PhysRev.73.416.

[10] R. P. Feynman. "Space-Time Approach to Quantum Electrodynamics". In: *Physical Review* 76.6 (Sept. 1949), pp. 769–789. DOI: 10.1103/PhysRev.76.769.

[11] R. P. Feynman. "Mathematical Formulation of the Quantum Theory of Electromagnetic Interaction". In: *Physical Review* 80.3 (Nov. 1950), pp. 440–457. DOI: 10.1103/PhysRev.80.440.

[12] X. Fan et al. "Measurement of the Electron Magnetic Moment". In: *Physical Review Letters* 130.7 (Feb. 2023), p. 071801. DOI: 10.1103/PhysRevLett.130.071801.

[13] Richard H. Parker et al. "Measurement of the Fine-Structure Constant as a Test of the Standard Model". In: *Science* 360.6385 (Apr. 2018), pp. 191–195. DOI: 10.1126/science.aap7706.

[14] Léo Morel et al. “Determination of the Fine-Structure Constant with an Accuracy of 81 Parts per Trillion”. In: *Nature* 588.7836 (Dec. 2020), pp. 61–65. ISSN: 1476-4687. DOI: 10.1038/s41586-020-2964-7.

[15] I. Beltrami et al. “New Precision Measurements of the Muonic $3d_{5/2}-2p_{3/2}$ X-ray Transition in ^{24}Mg and ^{28}Si: Vacuum Polarisation Test and Search for Muon-Hadron Interactions beyond QED”. In: *Nuclear Physics A* 451.4 (Apr. 1986), pp. 679–700. ISSN: 0375-9474. DOI: 10.1016/0375-9474(86)90299-X.

[16] M. Trassinelli et al. “Measurement of the Charged Pion Mass Using X-ray Spectroscopy of Exotic Atoms”. In: *Physics Letters B* 759 (Aug. 2016), pp. 583–588. ISSN: 0370-2693. DOI: 10.1016/j.physletb.2016.06.025.

[17] Masaki Hori et al. “Two-Photon Laser Spectroscopy of Antiprotonic Helium and the Antiproton-to-Electron Mass Ratio”. In: *Nature* 475.7357 (July 2011), pp. 484–488. ISSN: 1476-4687. DOI: 10.1038/nature10260.

[18] J. S. Tiedeman and H. G. Robinson. “Determination of $\frac{g_J(^1H,1^2S_{\frac{1}{2}})}{g_s(e)}$: Test of Mass-Independent Corrections”. In: *Physical Review Letters* 39.10 (Sept. 1977), pp. 602–604. DOI: 10.1103/PhysRevLett.39.602.

[19] C. E. Johnson and H. G. Robinson. “g_J Factor of an Ion: Determination of $\frac{g_J(^4He^+,1^2S_{\frac{1}{2}})}{g_J(^4He,2^3S_1)}$”. In: *Physical Review Letters* 45.4 (July 1980), pp. 250–252. DOI: 10.1103/PhysRevLett.45.250.

[20] H. Häffner et al. “Double Penning trap technique for precise g factor determinations in highly charged ions”. In: *The European Physical Journal D - Atomic, Molecular, Optical and Plasma Physics* 22.2 (Feb. 2003), pp. 163–182. ISSN: 1434-6079. DOI: 10.1140/epjd/e2003-00012-2.

[21] J. Verdú et al. “Electronic g Factor of Hydrogenlike Oxygen $^{16}O^{7+}$”. In: *Physical Review Letters* 92.9 (Mar. 2004), p. 093002. DOI: 10.1103/PhysRevLett.92.093002.

[22] S. Sturm et al. “g-factor measurement of hydrogenlike $^{28}Si^{13+}$ as a challenge to QED calculations”. In: *Physical Review A* 87.3 (Mar. 2013), p. 030501. DOI: 10.1103/PhysRevA.87.030501.

[23] A. Wagner et al. “g Factor of Lithiumlike Silicon $^{28}Si^{11+}$”. In: *Physical Review Letters* 110.3 (Jan. 2013), p. 033003. DOI: 10.1103/PhysRevLett.110.033003.

[24] S. Sturm et al. “High-Precision Measurement of the Atomic Mass of the Electron”. In: *Nature* 506.7489 (Feb. 2014), pp. 467–470. ISSN: 1476-4687. DOI: 10.1038/nature13026.

[25] Florian Köhler et al. “Isotope Dependence of the Zeeman Effect in Lithium-like Calcium”. In: *Nature Communications* 7.1 (Jan. 2016), p. 10246. ISSN: 2041-1723. DOI: 10.1038/ncomms10246.

[26] I. Arapoglou et al. “g Factor of Boronlike Argon $^{40}Ar^{13+}$”. In: *Physical Review Letters* 122.25 (June 2019), p. 253001. DOI: 10.1103/PhysRevLett.122.253001.

[27] D. A. Glazov et al. “g Factor of Lithiumlike Silicon: New Challenge to Bound-State QED”. In: *Physical Review Letters* 123.17 (Oct. 2019), p. 173001. DOI: 10.1103/PhysRevLett.123.173001.

[28] A. Schneider et al. “Direct Measurement of the $^3He^+$ Magnetic Moments”. In: *Nature* (June 2022), pp. 1–6. ISSN: 1476-4687. DOI: 10.1038/s41586-022-04761-7.

[29] F. Heiße et al. "High-Precision Determination of g Factors and Masses of $^{20}Ne^{9+}$ and $^{22}Ne^{9+}$". In: *Physical Review Letters* 131.25 (Dec. 2023), p. 253002. ISSN: 0031-9007, 1079-7114. DOI: 10.1103/PhysRevLett.131.253002.

[30] Stefan Dickopf et al. "Precision Spectroscopy on ^{9}Be Overcomes Limitations from Nuclear Structure". In: *Nature* 632.8026 (Aug. 2024), pp. 757–761. ISSN: 1476-4687. DOI: 10.1038/s41586-024-07795-1.

[31] P. Beiersdorfer et al. "Measurement of the Two-Loop Lamb Shift in Lithiumlike U^{89+}". In: *Physical Review Letters* 95.23 (Dec. 2005), p. 233003. DOI: 10.1103/PhysRevLett.95.233003.

[32] A. Gumberidze et al. "Quantum Electrodynamics in Strong Electric Fields: The Ground-State Lamb Shift in Hydrogenlike Uranium". In: *Physical Review Letters* 94.22 (June 2005), p. 223001. DOI: 10.1103/PhysRevLett.94.223001.

[33] Philip Pfäfflein et al. *Quantum Electrodynamics in Strong Electromagnetic Fields: Substate Resolved Kα Transition Energies in Helium-like Uranium*. July 2024. arXiv: 2407.04166 [physics].

[34] R. Loetzsch et al. "Testing Quantum Electrodynamics in Extreme Fields Using Helium-like Uranium". In: *Nature* 625.7996 (Jan. 2024), pp. 673–678. ISSN: 1476-4687. DOI: 10.1038/s41586-023-06910-y.

[35] P. Seelig et al. "Ground State Hyperfine Splitting of Hydrogenlike $^{207}Pb^{81+}$ by Laser Excitation of a Bunched Ion Beam in the GSI Experimental Storage Ring". In: *Physical Review Letters* 81.22 (Nov. 1998), pp. 4824–4827. DOI: 10.1103/PhysRevLett.81.4824.

[36] J. R. Crespo López-Urrutia et al. "Nuclear magnetization distribution radii determined by hyperfine transitions in the $1s$ level of H-like ions $^{185}Re^{74+}$ and $^{187}Re^{74+}$". In: *Physical Review A* 57.2 (Feb. 1998), pp. 879–887. DOI: 10.1103/PhysRevA.57.879.

[37] Johannes Ullmann et al. "High Precision Hyperfine Measurements in Bismuth Challenge Bound-State Strong-Field QED". In: *Nature Communications* 8.1 (May 2017), p. 15484. ISSN: 2041-1723. DOI: 10.1038/ncomms15484.

[38] Leonid V. Skripnikov et al. "New Nuclear Magnetic Moment of ^{209}Bi: Resolving the Bismuth Hyperfine Puzzle". In: *Physical Review Letters* 120.9 (Feb. 2018), p. 093001. ISSN: 0031-9007, 1079-7114. DOI: 10.1103/PhysRevLett.120.093001.

[39] Thomas Beier. "The g_j Factor of a Bound Electron and the Hyperfine Structure Splitting in Hydrogenlike Ions". In: *Physics Reports* 339.2 (Dec. 2000), pp. 79–213. ISSN: 0370-1573. DOI: 10.1016/S0370-1573(00)00071-5.

[40] V. M. Shabaev et al. "Towards a Test of QED in Investigations of the Hyperfine Splitting in Heavy Ions". In: *Physical Review Letters* 86.18 (Apr. 2001), pp. 3959–3962. DOI: 10.1103/PhysRevLett.86.3959.

[41] E. Borie and G. A. Rinker. "The Energy Levels of Muonic Atoms". In: *Reviews of Modern Physics* 54.1 (Jan. 1982), pp. 67–118. DOI: 10.1103/RevModPhys.54.67.

[42] Volker Hannen et al. "Lifetimes and g-factors of the HFS states in H-like and Li-like bismuth". In: *Journal of Physics B: Atomic, Molecular and Optical Physics* 52.8 (Apr. 2019), p. 085003. ISSN: 0953-4075. DOI: 10.1088/1361-6455/ab0ef0.

[43] Winfried Barth et al. "Carbon Stripper Foils for High Current Heavy Ion Operation". In: *Journal of Radioanalytical and Nuclear Chemistry* 299.2 (Feb. 2014), pp. 1047–1053. ISSN: 1588-2780. DOI: 10.1007/s10967-013-2651-3.

[44] H. -J. Kluge et al. "Chapter 7 HITRAP: A Facility at GSI for Highly Charged Ions". In: *Advances in Quantum Chemistry*. Ed. by S. Salomonson and E. Lindroth. Vol. 53. Current Trends in Atomic Physics. Academic Press, Jan. 2008, pp. 83–98. DOI: 10.1016/S0065-3276(07)53007-8.

[45] Morton A. Levine et al. "The Electron Beam Ion Trap: A New Instrument for Atomic Physics Measurements". In: *Physica Scripta* T22 (Jan. 1988), pp. 157–163. ISSN: 1402-4896. DOI: 10.1088/0031-8949/1988/T22/024.

[46] Wolfgang Lotz. "Electron-Impact Ionization Cross-Sections and Ionization Rate Coefficients for Atoms and Ions from Hydrogen to Calcium". In: *Zeitschrift für Physik* 216.3 (June 1968), pp. 241–247. ISSN: 0044-3328. DOI: 10.1007/BF01392963.

[47] F. Heiße et al. "High-Precision Mass Spectrometer for Light Ions". In: *Physical Review A* 100.2 (Aug. 2019), p. 022518. DOI: 10.1103/PhysRevA.100.022518.

[48] Moisés Medina Restrepo and Edmund G. Myers. "Mass Difference of Tritium and Helium-3". In: *Physical Review Letters* 131.24 (Dec. 2023), p. 243002. DOI: 10.1103/PhysRevLett.131.243002.

[49] N. Schwegler et al. "Trapping and Ground-State Cooling of a Single H_2^+". In: *Physical Review Letters* 131.13 (Sept. 2023), p. 133003. DOI: 10.1103/PhysRevLett.131.133003.

[50] A. Kramida et al. *NIST Atomic Spectra Database (Version 5.9)*. 2021.

[51] R. E. Marrs, S. R. Elliott, and D. A. Knapp. "Production and Trapping of Hydrogenlike and Bare Uranium Ions in an Electron Beam Ion Trap". In: *Physical Review Letters* 72.26 (June 1994), pp. 4082–4085. DOI: 10.1103/PhysRevLett.72.4082.

[52] Sven Sturm et al. "The ALPHATRAP Experiment". In: *The European Physical Journal Special Topics* 227.13 (Feb. 2019), pp. 1425–1491. ISSN: 1951-6355, 1951-6401. DOI: 10.1140/epjst/e2018-800225-2.

[53] A. J. González Martínez et al. "The Heidelberg EBIT : Present Results and Future Perspectives". In: *Journal of Physics: Conference Series* 72 (June 2007), p. 012001. ISSN: 1742-6596. DOI: 10.1088/1742-6596/72/1/012001.

[54] J. Morgner et al. "Stringent Test of QED with Hydrogen-like Tin". In: *Nature* 622.7981 (Oct. 2023), pp. 53–57. ISSN: 1476-4687. DOI: 10.1038/s41586-023-06453-2.

[55] V. A. Yerokhin et al. "Self-energy screening effects in the g factor of Li-like ions". In: *Physical Review A* 102.2 (Aug. 2020), p. 022815. DOI: 10.1103/PhysRevA.102.022815.

[56] V. A. Yerokhin, C. H. Keitel, and Z. Harman. "Two-photon-exchange corrections to the g factor of Li-like ions". In: *Physical Review A* 104.2 (Aug. 2021), p. 022814. DOI: 10.1103/PhysRevA.104.022814.

[57] V. P. Kosheleva et al. "g Factor of Lithiumlike Silicon and Calcium: Resolving the Disagreement between Theory and Experiment". In: *Physical Review Letters* 128.10 (Mar. 2022), p. 103001. DOI: 10.1103/PhysRevLett.128.103001.

[58] V. A. Yerokhin et al. "Electron-Correlation Effects in the g Factor of Light Li-like Ions". In: *Physical Review A* 95.6 (June 2017), p. 062511. DOI: 10.1103/PhysRevA.95.062511.

[59] Bastian Sikora. "Quantum Field Theory of the g-Factor of Bound Systems". PhD thesis. Ruprecht-Karls-Universität Heidelberg, Apr. 2018. DOI: 10.17617/2.2619194.

[60] B. Sikora et al. “Theory of the Two-Loop Self-Energy Correction to the g Factor in Nonperturbative Coulomb Fields”. In: *Physical Review Research* 2.1 (Jan. 2020), p. 012002. DOI: 10.1103/PhysRevResearch.2.012002.

[61] Igor A. Valuev et al. “Skyrme-Type Nuclear Interaction as a Tool for Calculating the Finite-Nuclear-Size Correction to Atomic Energy Levels and the Bound-Electron g Factor”. In: *Physical Review A* 101.6 (June 2020), p. 062502. DOI: 10.1103/PhysRevA.101.062502.

[62] H. Cakir et al. “QED corrections to the g factor of Li- and B-like ions”. In: *Physical Review A* 101.6 (June 2020), p. 062513. DOI: 10.1103/PhysRevA.101.062513.

[63] Andrzej Czarnecki et al. “Two-Loop Binding Corrections to the Electron Gyromagnetic Factor”. In: *Physical Review Letters* 120.4 (Jan. 2018), p. 043203. DOI: 10.1103/PhysRevLett.120.043203.

[64] Jonathan Morgner. “Listening to Electrons Talk: g-Factor Measurement of Lithiumlike Tin”. In: *Submitted to Science* (2024).

[65] W. H. Furry. “On Bound States and Scattering in Positron Theory”. In: *Physical Review* 81.1 (Jan. 1951), pp. 115–124. DOI: 10.1103/PhysRev.81.115.

[66] Andrzej Czarnecki, Kirill Melnikov, and Alexander Yelkhovsky. “Anomalous Magnetic Moment of a Bound Electron”. In: *Physical Review A* 63.1 (Dec. 2000), p. 012509. DOI: 10.1103/PhysRevA.63.012509.

[67] N. A. Belov et al. *Muonic Vacuum Polarization Correction to the Bound-Electron g-Factor*. Oct. 2016. DOI: 10.48550/arXiv.1610.01340. arXiv: 1610.01340 [physics].

[68] Muon g-2 Collaboration et al. “Measurement of the Positive Muon Anomalous Magnetic Moment to 0.46 Ppm”. In: *Physical Review Letters* 126.14 (Apr. 2021), p. 141801. DOI: 10.1103/PhysRevLett.126.141801.

[69] Tatsumi Aoyama, Toichiro Kinoshita, and Makiko Nio. “Theory of the Anomalous Magnetic Moment of the Electron”. In: *Atoms* 7.1 (Mar. 2019), p. 28. ISSN: 2218-2004. DOI: 10.3390/atoms7010028.

[70] Sergey Volkov. “Calculating the Five-Loop QED Contribution to the Electron Anomalous Magnetic Moment: Graphs without Lepton Loops”. In: *Physical Review D* 100.9 (Nov. 2019), p. 096004. DOI: 10.1103/PhysRevD.100.096004.

[71] G. Breit. “The Magnetic Moment of the Electron”. In: *Nature* 122.3078 (Oct. 1928), pp. 649–649. ISSN: 1476-4687. DOI: 10.1038/122649a0.

[72] Jonathan Morgner. “g-Factor Measurement of boron-like Tin”. In: *In Preparation* (2024).

[73] V. Debierre et al. “Two-Loop Virtual Light-by-Light Scattering Corrections to the Bound-Electron g Factor”. In: *Physical Review A* 103.3 (Mar. 2021), p. L030802. DOI: 10.1103/PhysRevA.103.L030802.

[74] I. Angeli and K. P. Marinova. “Table of Experimental Nuclear Ground State Charge Radii: An Update”. In: *Atomic Data and Nuclear Data Tables* 99.1 (Jan. 2013), pp. 69–95. ISSN: 0092-640X. DOI: 10.1016/j.adt.2011.12.006.

[75] Jacek Zatorski et al. “Nuclear Shape Effect on the g Factor of Hydrogenlike Ions”. In: *Physical Review Letters* 108.6 (Feb. 2012), p. 063005. DOI: 10.1103/PhysRevLett.108.063005.

[76] V. A. Yerokhin, C. H. Keitel, and Z. Harman. "Nuclear-Size Self-Energy and Vacuum-Polarization Corrections to the Bound-Electron g Factor". In: *Journal of Physics B: Atomic, Molecular and Optical Physics* 46.24 (Nov. 2013), p. 245002. ISSN: 0953-4075. DOI: 10.1088/0953-4075/46/24/245002.

[77] Savely G. Karshenboim and Vladimir G. Ivanov. "Finite-nuclear-size contribution to the g factor of a bound electron: Higher-order effects". In: *Physical Review A* 97.2 (Feb. 2018), p. 022506. DOI: 10.1103/PhysRevA.97.022506.

[78] V. M. Shabaev and V. A. Yerokhin. "Recoil Correction to the Bound-Electron g Factor in H-Like Atoms to All Orders in α Z". In: *Physical Review Letters* 88.9 (Feb. 2002), p. 091801. ISSN: 0031-9007, 1079-7114. DOI: 10.1103/PhysRevLett.88.091801.

[79] D. V. Zinenko et al. "Electron Correlation Effects on the g Factor of Lithiumlike Ions". In: *Physical Review A* 107.3 (Mar. 2023), p. 032815. DOI: 10.1103/PhysRevA.107.032815.

[80] A. V. Volotka et al. "Many-Electron QED Corrections to the g Factor of Lithiumlike Ions". In: *Physical Review Letters* 112.25 (June 2014), p. 253004. DOI: 10.1103/PhysRevLett.112.253004.

[81] A. V. Malyshev et al. "Ground-State Ionization Energies of Boronlike Ions". In: *Physical Review A* 96.2 (Aug. 2017), p. 022512. ISSN: 2469-9926, 2469-9934. DOI: 10.1103/PhysRevA.96.022512.

[82] T. P. Grozdanov and H. S. Taylor. "Second-Order Perturbation Calculations for the Hydrogenic Zeeman Effect". In: *Journal of Physics B: Atomic and Molecular Physics* 19.24 (Dec. 1986), p. 4075. ISSN: 0022-3700. DOI: 10.1088/0022-3700/19/24/011.

[83] A. S. Varentsova et al. "Third-Order Zeeman Effect in Highly Charged Ions". In: *Nuclear Instruments and Methods in Physics Research Section B: Beam Interactions with Materials and Atoms*. Proceedings of the 18th International Conference on the Physics of Highly Charged Ions (HCI-2016), Kielce, Poland, 11-16 September 2016 408 (Oct. 2017), pp. 80–83. ISSN: 0168-583X. DOI: 10.1016/j.nimb.2017.05.040.

[84] A. S. Varentsova et al. "Interelectronic-Interaction Contribution to the Nonlinear Zeeman Effect in Boronlike Ions". In: *Physical Review A* 97.4 (Apr. 2018), p. 043402. DOI: 10.1103/PhysRevA.97.043402.

[85] J.-Ph. Karr and Jeroen C. J. Koelemeij. "Extraction of spin-averaged rovibrational transition frequencies in HD^+ for the determination of fundamental constants". In: *Molecular Physics* 121.17-18 (Sept. 2023), e2216081. ISSN: 0026-8976. DOI: 10.1080/00268976.2023.2216081.

[86] Florian Thomas Köhler. "Bound-Electron g-Factor Measurements for the Determination of the Electron Mass and Isotope Shifts in Highly Charged Ions". PhD thesis. Heidelberg: Ruperto-Carola-University of Heidelberg, 2015. DOI: DOI:10.11588/heidok.00019184.

[87] Sascha Rau. "High-Precision Measurement of the Deuteron's Atomic Mass". PhD thesis. Heidelberg: Ruperto-Carola-University of Heidelberg, 2020. DOI: 10.11588/heidok.00029010.

[88] Lowell S. Brown and Gerald Gabrielse. "Precision Spectroscopy of a Charged Particle in an Imperfect Penning Trap". In: *Physical Review A* 25.4 (Apr. 1982), pp. 2423–2425. DOI: 10.1103/PhysRevA.25.2423.

[89] Lowell S. Brown and Gerald Gabrielse. "Geonium Theory: Physics of a Single Electron or Ion in a Penning Trap". In: *Reviews of Modern Physics* 58.1 (Jan. 1986), pp. 233–311. DOI: 10.1103/RevModPhys.58.233.

[90] Georg Jochen Ketter. "Theoretical Treatment of Miscellaneous Frequency-Shifts in Penning Traps with Classical Perturbation Theory". PhD thesis. Ruperto-Carola-University of Heidelberg, 2015. DOI: 10.11588/heidok.00018227.

[91] Lowell S Brown. "Geonium Lineshape". In: *Annals of Physics* 159.1 (Jan. 1985), pp. 62–98. ISSN: 0003-4916. DOI: 10.1016/0003-4916(85)90192-7.

[92] Sven Sturm. "The g-factor of the electron bound in $^{28}Si^{13+}$: The most stringent test of bound-state quantum electrodynamics". PhD thesis. Johannes-Gutenberg Universität Mainz, Apr. 2012. DOI: 10.25358/openscience-2019.

[93] M. Schuh et al. "Image Charge Shift in High-Precision Penning Traps". In: *Physical Review A* 100.2 (Aug. 2019), p. 023411. DOI: 10.1103/PhysRevA.100.023411.

[94] Ioanna Arapoglou. "First measurement of the ground-state g-factor of boronlike argon $^{40}Ar^{13+}$ in ALPHATRAP". PhD thesis. Ruprecht-Karls Universität Heidelberg, 2019. DOI: 10.11588/heidok.00026909.

[95] Tim Sailer. "Direct Bound-Electron g-Factor Difference Measurement of Coupled Ions at ALPHATRAP". PhD thesis. Ruprecht-Karls-Universität Heidelberg, Feb. 2022. DOI: 10.17617/2.3370290.

[96] Jochen Ketter et al. "Classical Calculation of Relativistic Frequency-Shifts in an Ideal Penning Trap". In: *International Journal of Mass Spectrometry* 361 (Mar. 2014), pp. 34–40. ISSN: 1387-3806. DOI: 10.1016/j.ijms.2014.01.028.

[97] D. J. Wineland and H. G. Dehmelt. "Principles of the Stored Ion Calorimeter". In: *Journal of Applied Physics* 46.2 (Feb. 1975), pp. 919–930. ISSN: 0021-8979. DOI: 10.1063/1.321602.

[98] Sven Sturm et al. "Phase-Sensitive Cyclotron Frequency Measurements at Ultralow Energies". In: *Physical Review Letters* 107.14 (Sept. 2011), p. 143003. DOI: 10.1103/PhysRevLett.107.143003.

[99] Stefan Ulmer. "First Observation of Spin Flips with a Single Proton Stored in a Cryogenic Penning Trap". PhD thesis. Ruperto-Carola University of Heidelberg, 2011. DOI: DOI:10.11588/heidok.00012306.

[100] M. J. Borchert et al. "Measurement of Ultralow Heating Rates of a Single Antiproton in a Cryogenic Penning Trap". In: *Physical Review Letters* 122.4 (Jan. 2019), p. 043201. DOI: 10.1103/PhysRevLett.122.043201.

[101] Robert W. Schmieder. "Physics of the EBIS and Its Ions". In: *Physics of Highly-Ionized Atoms*. Ed. by Richard Marrus. NATO ASI Series. Boston, MA: Springer US, 1989, pp. 321–376. ISBN: 978-1-4613-0833-1. DOI: 10.1007/978-1-4613-0833-1_10.

[102] Simon Marcus Heidrich. "Recommissionig of the Hyper-EBIT by Measuring X-Ray Spectra of Highly Charged Ions". PhD thesis. Ruperto-Carola-University of Heidelberg, 2022.

[103] Thomas M. Baumann et al. "Contributions of Dielectronic, Trielectronic, and Metastable Channels to the Resonant Intershell Recombination of Highly Charged Silicon Ions". In: *Physical Review A* 90.5 (Nov. 2014), p. 052704. DOI: 10.1103/PhysRevA.90.052704.

[104] Michael Andreas Blessenohl. "Fine-Structure Investigations in Highly Charged Ions Using Spectroscopy in the Vacuum Ultraviolet Regime". PhD thesis. Heidelberg: Ruprecht-Karls-Universität Heidelberg, 2020. DOI: 10.11588/heidok.00028747.

[105] Thomas Baumann. "Spektroskopische Untersuchungen resonanter Rekombinationsprozesse an hochgeladenem Silizium in einer Elektronenstrahl-Ionenfalle". PhD thesis. Ruperto-Carola-University of Heidelberg, 2012. DOI: 10.11588/heidok.00013380.

[106] Nils-Holger Rehbehn et al. "Sensitivity to New Physics of Isotope-Shift Studies Using the Coronal Lines of Highly Charged Calcium Ions". In: *Physical Review A* 103.4 (Apr. 2021), p. L040801. DOI: 10.1103/PhysRevA.103.L040801.

[107] Gabriel Herrmann. "Optical Theory of Thermal Velocity Effects in Cylindrical Electron Beams". In: *Journal of Applied Physics* 29.2 (Feb. 1958), pp. 127–136. ISSN: 0021-8979. DOI: 10.1063/1.1723053.

[108] Andreas Weigel. "Detection Electronics Design and First Observation of Bound-Electron Spin Transitions at the ALPHATRAP g-Factor Experiment". PhD thesis. Ruprecht-Karls-Universität Heidelberg, Jan. 2019. DOI: 10.17617/2.3150015.

[109] Tim Sailer. "A Laser Ion Source for the ALPHATRAP Experiment". PhD thesis. Ruprecht-Karls-Universität Heidelberg, Aug. 2017.

[110] Lisa Franziska Buchauer. "Konstruktion einer kompakten Elektronenstrahl- Ionenfalle mit Permanentmagneten für Fluoreszenzmessungen". Bachelor Thesis. Ruprecht- Karls-Universität Heidelberg, 2012.

[111] P. Micke et al. "The Heidelberg Compact Electron Beam Ion Traps". In: *Review of Scientific Instruments* 89.6 (June 2018), p. 063109. ISSN: 0034-6748. DOI: 10.1063/1.5026961.

[112] Alexander Egl. "High-Precision Laser Spectroscopy of the Fine Structure in $^{40}Ar^{13+}$ at ALPHATRAP". PhD thesis. Heidelberg: Ruprecht- Karls-Universität Heidelberg, 2020. DOI: 10.11588/heidok.00028293.

[113] Bingsheng Tu et al. "Tank-Circuit Assisted Coupling Method for Sympathetic Laser Cooling". In: *Advanced Quantum Technologies* 4.7 (2021), p. 2100029. ISSN: 2511-9044. DOI: 10.1002/qute.202100029.

[114] Tim Sailer et al. "Measurement of the Bound-Electron g-Factor Difference in Coupled Ions". In: *Nature* 606.7914 (June 2022), pp. 479–483. ISSN: 1476-4687. DOI: 10.1038/s41586-022-04807-w.

[115] Hendrik Bekker. "Optical and EUV Spectroscopy of Highly Charged Ions near the $4f$–$5s$ Level Crossing". PhD thesis. Ruprecht-Karls-Universität Heidelberg, May 2016. DOI: 10.17617/2.2291831.

[116] Marko Turkalj Orešković. "Development of a Cryogenic Vacuum Valve and an Electromechanical Switch for ALPHATRAP". PhD thesis. Ruprecht-Karls-Universität Heidelberg, Feb. 2014.

[117] Valentin Friedrich Hahn. "Design and Commissioning of an Optically Transparent Cryogenic Valve for the ALPHATRAP Experiment". PhD thesis. Ruprecht-Karls-Universität Heidelberg, 2023.

[118] Alexander Egl et al. "Application of the Continuous Stern-Gerlach Effect for Laser Spectroscopy of the $^{40}Ar^{13+}$ Fine Structure in a Penning Trap". In: *Physical Review Letters* 123.12 (Sept. 2019), p. 123001. DOI: 10.1103/PhysRevLett.123.123001.

[119] Jack A. Devlin et al. "Superconducting Solenoid System with Adjustable Shielding Factor for Precision Measurements of the Properties of the Antiproton". In: *Physical Review Applied* 12.4 (Oct. 2019), p. 044012. DOI: 10.1103/PhysRevApplied.12.044012.

[120] Ch. Schweiger et al. “Production of Highly Charged Ions of Rare Species by Laser-Induced Desorption inside an Electron Beam Ion Trap”. In: *Review of Scientific Instruments* 90.12 (Dec. 2019), p. 123201. ISSN: 0034-6748. DOI: 10.1063/1.5128331.

[121] C. B. Alcock, V. P. Itkin, and M. K. Horrigan. “Vapour Pressure Equations for the Metallic Elements: 298–2500K”. In: *Canadian Metallurgical Quarterly* 23.3 (July 1984), pp. 309–313. ISSN: 0008-4433, 1879-1395. DOI: 10.1179/cmq.1984.23.3.309.

[122] D. A. Knapp et al. “A High-Energy Electron Beam Ion Trap for Production of High-Charge High-Z Ions”. In: *Nuclear Instruments and Methods in Physics Research Section A: Accelerators, Spectrometers, Detectors and Associated Equipment* 334.2 (Oct. 1993), pp. 305–312. ISSN: 0168-9002. DOI: 10.1016/0168-9002(93)90790-O.

[123] Igor A. Kotelnikov and Alexander I. Milstein. “Electron Radiative Recombination with a Hydrogen-like Ion”. In: *Physica Scripta* 94.5 (Mar. 2019), p. 055403. ISSN: 1402-4896. DOI: 10.1088/1402-4896/ab060a.

[124] S. Sellner et al. “Improved Limit on the Directly Measured Antiproton Lifetime”. In: *New Journal of Physics* 19.8 (Aug. 2017), p. 083023. ISSN: 1367-2630. DOI: 10.1088/1367-2630/aa7e73.

[125] C Day. “Basics and Applications of Cryopumps”. In: *CAS - CERN Accelerator School : Vacuum in Accelerators* (2007), pp. 241–274. DOI: 10.5170/CERN-2007-003.241.

[126] B. M. Latacz et al. “Ultra-Thin Polymer Foil Cryogenic Window for Antiproton Deceleration and Storage”. In: *Review of Scientific Instruments* 94.10 (Oct. 2023), p. 103310. ISSN: 0034-6748. DOI: 10.1063/5.0167262.

[127] Alfred Müller and Erhard Salzborn. “Scaling of Cross Sections for Multiple Electron Transfer to Highly Charged Ions Colliding with Atoms and Molecules”. In: *Physics Letters A* 62.6 (Sept. 1977), pp. 391–394. ISSN: 03759601. DOI: 10.1016/0375-9601(77)90672-7.

[128] R. E. Olson and A. Salop. “Electron Transfer between Multicharged Ions and Neutral Species”. In: *Physical Review A* 14.2 (Aug. 1976), pp. 579–585. DOI: 10.1103/PhysRevA.14.579.

[129] H. Tawara et al. “Electron Capture Processes of I^{q+} Ions with Very High Charge States ($41 \geq q \geq 10$) in Collisions with He Atoms”. In: *Journal of Physics B: Atomic and Molecular Physics* 18.2 (Jan. 1985), p. 337. ISSN: 0022-3700. DOI: 10.1088/0022-3700/18/2/020.

[130] R. Mann. “Total One-Electron Capture Cross Sections for Ar^{q+} and I^{q+} Ions in Slow Collisions on H_2 and He”. In: *Zeitschrift für Physik D Atoms, Molecules and Clusters* 3.1 (Mar. 1986), pp. 85–90. ISSN: 1431-5866. DOI: 10.1007/BF01442351.

[131] H. Cederquist et al. “Increase of True Double-Electron-Capture Cross Sections in Slow Xe^{q+}-(Xe,He) Collisions at Very High q”. In: *Physical Review A* 46.5 (Sept. 1992), pp. 2592–2595. ISSN: 1050-2947, 1094-1622. DOI: 10.1103/PhysRevA.46.2592.

[132] Scott Kravis et al. “Single- and Double-Charge-Exchange Cross Sections for $Ar^{q+}+H_2$ (q=6, 7, 8, 9, and 11) Collisions from 6 eV to 11 keV”. In: *Physical Review A* 52.2 (Aug. 1995), pp. 1206–1212. DOI: 10.1103/PhysRevA.52.1206.

[133] S. Stahl et al. “Phase-Sensitive Measurement of Trapped Particle Motions”. In: *Journal of Physics B: Atomic, Molecular and Optical Physics* 38.3 (Jan. 2005), p. 297. ISSN: 0953-4075. DOI: 10.1088/0953-4075/38/3/013.

[134] Tim Sailer. “Aufbau Einer Präzisionsspannungsquelle Für Das ALPHATRAP-Experiment”. PhD thesis. Ruprecht-Karls-Universität Heidelberg, 2015.

[135] W. J. Huang et al. “The AME 2020 Atomic Mass Evaluation (I). Evaluation of Input Data, and Adjustment Procedures”. In: *Chinese Physics C* 45.3 (Mar. 2021), p. 030002. ISSN: 1674-1137. DOI: 10.1088/1674-1137/abddb0.

[136] Birgit Schabinger. “Ein Experiment zur Bestimmung des g-Faktors des gebundenen Elektrons in wasserstoff- und lithiumähnlichen mittelschweren Ionen”. PhD thesis. Johannes Gutenberg-Universität Mainz, 2011. DOI: 10.25358/OPENSCIENCE-3198.

[137] Menno Door. “Precision Mass and Mass-Ratio Measurements of Neon and Ytterbium Isotopes for Tests of Fundamental Physics”. PhD thesis. Heidelberg: Ruperto-Carola-University of Heidelberg, 2024. DOI: 10.11588/heidok.00035208.

[138] Eite Tiesinga et al. “CODATA Recommended Values of the Fundamental Physical Constants: 2018”. In: *Reviews of Modern Physics* 93.2 (June 2021), p. 025010. DOI: 10.1103/RevModPhys.93.025010.

[139] A. Rischka et al. “Mass-Difference Measurements on Heavy Nuclides with an eV/c^2 Accuracy in the PENTATRAP Spectrometer”. In: *Physical Review Letters* 124.11 (Mar. 2020), p. 113001. DOI: 10.1103/PhysRevLett.124.113001.

[140] Kathrin Kromer et al. “High-Precision Mass Measurement of Doubly Magic ^{208}Pb”. In: *The European Physical Journal A* 58.10 (Oct. 2022), p. 202. ISSN: 1434-601X. DOI: 10.1140/epja/s10050-022-00860-1.

[141] Kathrin Kromer et al. “Atomic Mass Determination of Uranium-238”. In: *Physical Review C* 109.2 (Feb. 2024), p. L021301. ISSN: 2469-9985, 2469-9993. DOI: 10.1103/PhysRevC.109.L021301.

[142] S. Sasidharan et al. “Penning-Trap Mass Measurement of Helium-4”. In: *Physical Review Letters* 131.9 (Aug. 2023), p. 093201. ISSN: 0031-9007, 1079-7114. DOI: 10.1103/PhysRevLett.131.093201.

[143] F. Teyssandier and D. Prêle. “Commercially Available Capacitors at Cryogenic Temperatures”. In: *Ninth International Workshop on Low Temperature Electronics - WOLTE9*. June 2010.

[144] J.C. Kuenen and G.C.M. Meijer. “Measurement of Dielectric Absorption of Capacitors and Analysis of Its Effects on VCOs”. In: *IEEE Transactions on Instrumentation and Measurement* 45.1 (Feb. 1996), pp. 89–97. ISSN: 1557-9662. DOI: 10.1109/19.481317.

[145] Xilin Xu et al. “Advances in Class-I C0G MLCC and SMD Film Capacitors”. In: *Proceeding CARTS USA 2008*. Newport Beach: Electronic Components Industry Association (ECIA), Mar. 2008.

[146] Peter J. Mohr et al. *Codata Internationally Recommended 2022 Values of the Fundamental Physical Constants*. 2024.

[147] V. A. Agababaev et al. “g Factor of the $[(1s)^2(2s)^22p]^2P_{3/2}$ State of Middle-Z Boronlike Ions”. In: *X-Ray Spectrometry* 49.1 (2020), pp. 143–148. ISSN: 1097-4539. DOI: 10.1002/xrs.3074.

[148] Martin Hermans. “Selective, Laser-Induced Etching of Fused Silica at High Scan-Speeds Using KOH”. In: *Journal of Laser Micro/Nanoengineering* 9.2 (June 2014), pp. 126–131. ISSN: 18800688. DOI: 10.2961/jlmn.2014.02.0009.

[149] L. Schmöger et al. “Coulomb Crystallization of Highly Charged Ions”. In: *Science* 347.6227 (Mar. 2015), pp. 1233–1236. DOI: 10.1126/science.aaa2960.

[150] R. Schuch et al. “The New Stockholm Electron Beam Ion Trap (S-EBIT)”. In: *Journal of Instrumentation* 5.12 (Dec. 2010), p. C12018. ISSN: 1748-0221. DOI: 10.1088/1748-0221/5/12/C12018.

[151] Y. Fu et al. “Overview of the Shanghai EBIT”. In: *Journal of Instrumentation* 5.08 (Aug. 2010), p. C08011. ISSN: 1748-0221. DOI: 10.1088/1748-0221/5/08/C08011.

[152] S. W. Epp et al. “X-Ray Laser Spectroscopy of Highly Charged Ions at FLASH”. In: *Journal of Physics B: Atomic, Molecular and Optical Physics* 43.19 (Sept. 2010), p. 194008. ISSN: 0953-4075. DOI: 10.1088/0953-4075/43/19/194008.

[153] M. A. Blessenohl et al. “An Electron Beam Ion Trap and Source for Re-Acceleration of Rare-Isotope Ion Beams at TRIUMF”. In: *Review of Scientific Instruments* 89.5 (May 2018), p. 052401. ISSN: 0034-6748. DOI: 10.1063/1.5021045.

[154] R. von Hahn et al. “The Cryogenic Storage Ring CSR”. In: *Review of Scientific Instruments* 87.6 (June 2016), p. 063115. ISSN: 0034-6748. DOI: 10.1063/1.4953888.

[155] Friedrich Paschen. “Ueber Die Zum Funkenübergang in Luft, Wasserstoff Und Kohlensäure Bei Verschiedenen Drucken Erforderliche Potentialdifferenz”. In: *Annalen der Physik* 273.5 (1889), pp. 69–96. ISSN: 1521-3889. DOI: 10.1002/andp.18892730505.

[156] J.T. Krile et al. “DC Flashover of a Dielectric Surface in Atmospheric Conditions”. In: *IEEE Transactions on Plasma Science* 32.5 (Oct. 2004), pp. 1828–1834. ISSN: 1939-9375. DOI: 10.1109/TPS.2004.835483.

[157] H. Fujita et al. “Breakdown Voltages of Gaseous N_2 and Air from Normal to Cryogenic Temperatures”. In: *Cryogenics* 18.4 (Apr. 1978), pp. 195–200. ISSN: 00112275. DOI: 10.1016/0011-2275(78)90001-2.

[158] A. V. Borodulina, O. V. Minakova, and S. L. Veber. “Breakdown Voltage in Argon, Nitrogen, and Sulfur Hexafluoride Gases As a Function of Temperature”. In: *Russian Journal of Coordination Chemistry* 48.7 (July 2022), pp. 452–455. ISSN: 1608-3318. DOI: 10.1134/S1070328422070028.

[159] Pieter Billen et al. “Replacing SF_6 in Electrical Gas-Insulated Switchgear: Technological Alternatives and Potential Life Cycle Greenhouse Gas Savings in an EU-28 Perspective”. In: *Energies* 13.7 (Jan. 2020), p. 1807. ISSN: 1996-1073. DOI: 10.3390/en13071807.

[160] G. Gabrielse and J. Tan. “Self-shielding Superconducting Solenoid Systems”. In: *Journal of Applied Physics* 63.10 (May 1988), pp. 5143–5148. ISSN: 0021-8979. DOI: 10.1063/1.340416.

[161] D.W. Allan. “Statistics of Atomic Frequency Standards”. In: *Proceedings of the IEEE* 54.2 (Feb. 1966), pp. 221–230. ISSN: 1558-2256. DOI: 10.1109/PROC.1966.4634.

[162] David J. Fink. “A New Value for the Deuteron to Proton Mass Ratio from Precision Measurements of the Cyclotron Frequencies of H_2^+ and D^+”. PhD thesis. Tallahassee, Florida: Florida State University, 2022.

[163] Stefan Dickopf. “High-Precision Penning-trap Measurements of the Magnetic Moments and Hyperfine Splitting in Hydrogen-like Beryllium-9”. PhD thesis. Heidelberg: Ruprecht-Karls-Universität Heidelberg, 2024. DOI: 10.11588/heidok.00035066.

[164] N J Simon, E S Drexler, and R P Reed. *Properties of Copper and Copper Alloys at Cryogenic Temperatures*. Tech. rep. NIST MONO 177. Gaithersburg, MD: National Institute of Standards and Technology, 1992, NIST MONO 177. DOI: 10.6028/NIST.MONO.177.

[165] Markus Wiesinger. "Sympathetic Cooling of a Single Individually-Trapped Proton in a Cryogenic Penning Trap". PhD thesis. Ruprecht-Karls Universität Heidelberg, July 2023. DOI: 10.11588/heidok.00033334.

[166] Randolf Pohl et al. "The Size of the Proton". In: *Nature* 466.7303 (July 2010), pp. 213–216. ISSN: 1476-4687. DOI: 10.1038/nature09250.

[167] W. R. Johnson and Gerhard Soff. "The Lamb Shift in Hydrogen-like Atoms, $1 \leq Z \leq 110$". In: *Atomic Data and Nuclear Data Tables* 33.3 (Nov. 1985), pp. 405–446. ISSN: 0092-640X. DOI: 10.1016/0092-640X(85)90010-5.

[168] V. A. Yerokhin and V. M. Shabaev. "Lamb Shift of $n = 1$ and $n = 2$ States of Hydrogen-like Atoms, $1 \leq Z \leq 110$". In: *Journal of Physical and Chemical Reference Data* 44.3 (Sept. 2015), p. 033103. ISSN: 0047-2689. DOI: 10.1063/1.4927487.

[169] V. A. Yerokhin and A. Surzhykov. "Energy Levels of Core-Excited $1s2l2l'$ States in Lithium-Like Ions: Argon to Uranium". In: *Journal of Physical and Chemical Reference Data* 47.2 (June 2018), p. 023105. ISSN: 0047-2689. DOI: 10.1063/1.5034574.

[170] T. Okumura et al. "Proof-of-Principle Experiment for Testing Strong-Field Quantum Electrodynamics with Exotic Atoms: High Precision X-Ray Spectroscopy of Muonic Neon". In: *Physical Review Letters* 130.17 (Apr. 2023), p. 173001. DOI: 10.1103/PhysRevLett.130.173001.

[171] V. M. Shabaev et al. "g-Factor of Heavy Ions: A New Access to the Fine Structure Constant". In: *Physical Review Letters* 96.25 (June 2006), p. 253002. DOI: 10.1103/PhysRevLett.96.253002.

Acknowledgments

An dieser Stelle möchte ich mich bei den vielen Leuten bedanken, die es mir ermöglicht haben, diese Arbeit fertigzustellen. Es war eine tolle Zeit und die gezeigten Ergebnisse sind mit Sicherheit ein Resultat aus der Zusammenarbeit mit den vielen Personen, die mir mit Rat und Tat zur Seite gestanden haben. Dieser Dank geht natürlich nicht nur an die im Folgenden genannten Personen, sondern an alle, die mich begleitet haben.

Angefangen mit dir, **Klaus**. Ich danke dir herzlich, dass du mich über die Zeit mit deiner hilfreichen und freundlichen Art unterstützt hast und bei quasi allen Themen maßgebend mitgewirkt hast. Deine Begeisterung an der Physik ist wirklich ansteckend und motiviert, die Welt in ihren Grundfesten zu hinterfragen. Ich kann mich noch sehr gut an unser erstes Telefonat erinnern: Wie nervös ich war, mit dem großen Prof. Klaus Blaum zu telefonieren. Aber im Laufe des Gesprächs konnte ich meine Nervosität durch deine nette Art schnell vergessen. Insgesamt gebührt dir viel Dank und Anerkennung für all deine Hilfe! Ich habe mich wirklich willkommen in der Gruppe gefühlt. Danke!

Similarly, I want to express my gratitute towards Professor **Degenkolb**. Thank you for being the second examiner of the thesis, and thanks for your support throughout the writing process.

Lieber **Sven**, auch dir danke ich für deine Rolle als direkter Ansprechpartner zu allen Belangen während der Arbeit an Alphatrap. Aus jedem einzelnen Gespräch habe ich extrem viel mitnehmen und lernen können. Du hast einen wirklich prägenden Einfluss auf mich gehabt. Deine Kreativität beim Lösen verschiedenster Probleme habe ich so noch nie erlebt. Ich bin wirklich froh, mit dir an Alphatrap gearbeitet zu haben. Du wirst für mich ein Vorbild bleiben, danke dafür!

Ganz viel Dank geht auch an dich, liebe **Gabi**. Dein Organisationstalent ist wirklich einzigartig und in der ganzen Zeit konntest mir in allen Belangen weiterhelfen.

Einen sehr direkten Einfluss auf diese Arbeit hatten natürlich alle Mitglieder von Alphatrap, die mir während der Arbeit nicht nur viel beigebracht, sondern auch untersützend zur Seite gestanden haben. Gern erinnere ich mich an die vielen Abende, an denen wir den Tag im Büro haben ausklingen lassen. Spezieller Dank geht hier an **Charlotte**. Da wir gleichzeitig mit der Doktorarbeit begonnen haben, hatten wir ähnliche Fragen und Probleme, bei denen deine Unterstützung sehr hilfreich war. Danke für deine lockere Art und die Gespräche, die mir in vielen Dingen eine neue Perspektive eröffnet haben. Danke auch für die Organisation unserer Teilnahme an der *Lion Team Challenge* (beim nächsten Mal bin ich bestimmt schneller als du, bei der Promotion habe ich es ja immerhin knapp geschafft). Weiterhin danke ich auch **Fabian**, der über all die Jahre an meiner Seite stand und mich als Postdoc in viele Themen eingewiesen hat. Das war unglaublich wertvoll für diese Arbeit. Deine Fähigkeit, Zusammenhänge zu erkennen, das Big-Picture der *QED tests in strong fields* zu überblicken, ist einzigartig. Ich bin sehr froh, mit dir zusammengearbeitet zu haben. Danke! I would also like to thank **Bingsheng** for his patience with me at the beginning. You really took your time in order to help me get started quickly with the experimental side of both the HCI production and the Alphatrap apparatus. Thank you for that. I wish you lots of success with your current endeavors! Vielen Dank auch an **Tim**, der mir als vorangegangener Doktorand eine unglaubliche Hilfe war. Als Experte und Sitz-Nachbar warst du für mich oftmals der Ansprechpartner Nummer eins; danke für dein offenes Ohr, deine lustige Art und für die schöne Zeit, die wir gemeinsam verbracht haben!

Schließlich möchte ich mich bei den Kolleginnen und Kollegen von Pentatrap, Liontrap und μTEx bedanken, insbesondere bei **Menno**, **Kathrin**, **Olesia**, **Marius** und **Stefan**. Als Co-Promovierende wart ihr eine echte Bereicherung und ich habe die Zeit mit euch sehr genossen.

Special Thanks goes out to all the theoreticians, which are the ones making these measurements worthwhile. Danke dir, **Zoltán**, für die lange und gute Zusammenarbeit. So viele Dinge haben wir gemeinsam durch dein Wirken erreicht. Deine Fähigkeit, die komplexen Themen der Quanten Elektrodynamic zu erklären ist einzigartig und hat mir vieles erleichtert. Danke auch, dass du ein Prüfer bei meiner Disputation bist! Furthermore, I thank **Vladimir** for his large impact on many of the calculations to which the tin measurements are compared to. Looking at your list of publications, your importance to the community is nearly unparalleled. Whenever a question from us experimentalists arose, you could help quickly and precisely, thank you for that! Viel Dank geht auch an **Bastian**: Die viele Rechnungen, die du an den g-Faktoren gemacht hast, haben essentiell zu den tollen Ergebnissen geführt. Danke auch für alle Fragen, die ich dir in der Zeit stellen konnte, und danke auch für das Korrekturlesen von dem Theorie-Kapitel. Jetzt, wo deine ersten Ergebnisse zu den *Two-Loop All-Order*-Rechnungen vorliegen, bin ich besonders gespannt, wie es mit den g-Faktoren weitergeht!

Weiterhin danke ich allen Personen am MPIK, die mich und meine Projekte auf verschiedenste Weise begleitet haben. Vielen Dank an Frau **Mörk** und **Frank** von dem Konstruktions-Büro für die großartige Arbeit an dem *Hyper-EBIT*-Projekt. Danke an die Hauptwerkstatt, besonders an Herrn **Spranz** und Herrn **Mather**, für die gute Zusammenarbeit bei so vielen Projekten. Danke an **Christian** und die Beschleuniger-Werkstatt für die viele Mithilfe an verschiedensten Projekten, besonders für den zügigen und soliden Aufbau von dem Hochspannungs-Labor der Hyper-EBIT.

Zuletzt möchte ich mich bei meinen **Eltern** und meinen **Geschwistern** bedanken. In der ganzen Zeit wart ihr immer eine sicherer Hafen für mich. Danke für all eure unterstützenden Worte und eure Geduld mit mir. Ich bin froh, eine so tolle Familie zu haben!